Assessment of ICESat-2 laser altimetry in hydrological applications

A thesis accepted by the Faculty of Aerospace Engineering and Geodesy of the University of Stuttgart in partial fulfillment of the requirements for the degree of Doctor of Engineering Sciences (Dr.-Ing.)

by

Bo Wang
born in Heilongjiang, China

Main referee:	Prof. Dr.-Ing. Nico Sneeuw
Co-referee:	Prof. Dr. techn. Gottfried Mandlburger
Date of defense:	07 February 2024

Institute of Geodesy
University of Stuttgart
2024

Acknowledgement

I would like to express my deepest gratitude to my supervisor, Prof. Nico Sneeuw, for his warm guidance, support, and encouragement throughout my PhD study. His expertise, patience, and unwavering commitment have been instrumental in shaping this thesis. I am grateful for his patience, kindness, and accessibility, which have made him not just a supervisor but also a trusted mentor and friend. He has consistently challenged and motivated me to push the boundaries of my research, encouraging me to strive for excellence in everything I do. I am forever grateful for the impact he has had on my academic and personal journey.

I am deeply grateful to Prof. Gottfried Mandlburger for his insightful feedback, constructive criticism, and thorough examination of this thesis. His expertise and contributions have enriched the quality of this research and enhanced its scholarly rigor. I am appreciative of his commitment to academic excellence and his willingness to share his knowledge and expertise in laser technology, which has significantly enhanced the quality of this thesis. I also want to express my sincere appreciation to Prof. Uwe Sörgel for his leadership, guidance, and impartiality as the chair of my PhD defense.

I am grateful to all my colleagues at the Institute of Geodesy, University of Stuttgart for providing the resources and facilities necessary for conducting this research. Special thanks to Dr. Mohammad Tourian, Dr. Peyman Saemian and Dr. Omid Elmi for providing a lot of stimulating discussions, shared insights, and mutual support; and to Tamara De Francesco, Ron Schlesinger and Thomas Götz who have supported me a lot in living smoothly at the institute.

I would like to acknowledge the China Scholarship Council (CSC) for the financial support during my PhD study in Germany.

To my friends in Stuttgart, thank them for their friendship, encouragement, and solidarity. Their support has been a constant source of strength, and I am grateful for the camaraderie we have shared. Our friendship and companionship have made this

journey more fulfilling and enjoyable.

Last but not least, to my cherished parents, girlfriend and family, I owe the deepest debt of gratitude. Their unwavering love, encouragement, and sacrifices have been the bedrock of my journey. I am profoundly grateful to them for their unconditional support, belief in my abilities, and endless encouragement. Their sacrifices and unwavering faith in me have been a constant source of strength and motivation.

Contents

List of Figures

List of Tables

List of Abbreviations

AATSR	Advanced Along-Track Scanning Radiometer
ALOS	Advanced Land Observing Satellite
AMSR-E	Advanced Microwave Scanning Radiometer for EOS
AMSU-B	Advanced Microwave Sounding Unit-B
ATLAS	Advanced Topographic Laser Altimeter System
CNES	French Space Agency
CNSA	China National Space Administration
DBSCAN	Density-Based Spatial Clustering of Applications with Noise
DEM	Digital Elevation Model
DGPS	Differential Global Positioning System
EOS	Earth Observing System
ESA	European Space Agency
ETM	Enhanced Thematic Mapper
GEBCO	General Bathymetric Chart of the Oceans
GEDI	Global Ecosystem Dynamics Investigation
GLAS	Geoscience Laser Altimeter System
GNSS-R	Global Navigation Satellite System Reflectometry
GOMOS	Global Ozone Monitoring by Occultation of Stars
GPM	Global Precipitation Mission
GPS	Global Positioning System
GRACE	Gravity Recovery and Climate Experiment
GRDC	Global Runoff Data Centre
GRWL	Global River Widths from Landsat
GSWE	Global Surface Water Explorer
InSAR	Interferometric Synthetic Aperture Radar
IPCC	Intergovernmental Panel on Climate Change
LiDAR	Light Detection and Ranging
LOLA	Lunar Orbiter Laser Altimeter
LRM	Low-resolution Mode
LRO	Lunar Reconnaissance Orbiter
LS	Least Squares

LST Land Surface Temperature
MABEL Multiple Altimeter Beam Experimental Lidar
MAD Median Absolute Deviation
MERIS Medium Resolution Imaging Spectrometer
MERIT Multi-Error-Removed Improved-Terrain
MGS Mars Global Surveyor
MNDWI Modified Normalized Difference Water Index
MODIS Moderate Resolution Imaging Spectroradiometer
MOLA Mars Orbiter Laser Altimeter
MSL Mean Sea Level
MSS Multi Spectral Scanner
NASA National Aeronautics and Space Administration
NDWI Normalized Difference Water Index
NIR Near-Infrared
OLI Operational Land Imager
POD Precision Orbit Determination
PPD Precision Pointing Determination
RANSAC Random Sample Consensus
RGT Reference Ground Track
RH Relative Height
RMS Root Mean Square
RMSE Root Mean Square Error
RSS River Surface Slope
SAR Synthetic Aperture Radar
SDB Satellite-based Bathymetry
SIRAL Synthetic Aperture Interferometric Radar Altimeter
SLC Scan Line Corrector
SMAP Soil Moisture Active Passive
SMOS Soil Moisture and Ocean Salinity
SNR Signal-to-Noise Ratio
SRTM Shuttle Radar Topography Mission
SSH Sea Surface Height
SSMI Special Sensor Microwave Imager
SSW Sea Surface Wind
SWE Snow Water Equivalent
SWH Significant Wave Height
SWIR Short-Wave Infrared
SWORD SWOT River Database

TIRS	Thermal Infrared Sensor
TM	Thematic Mapper
TRMM	Tropical Rainfall Measuring Mission
USGS	U.S. Geological Survey
WGS84	World Geodetic System 1984
XO	Crossover

Abstract

Water bodies act as critical components of the hydrological cycle, serving as reservoirs, lakes, wetlands, and aquifers that store and release water over time. Monitoring changes in the extent and volume of these water bodies is crucial for understanding their role in regulating water flow, maintaining baseflow during dry periods, and supporting ecological habitats. Furthermore, the identification of trends and alterations in water body dynamics aids in detecting potential impacts of climate change and human activities on the hydrological cycle. Historically, gauge stations have been employed to monitor the water level of these bodies since the 19th century. However, their numbers have been dwindling since the 1970s due to maintenance challenges. With the development of satellite altimetry missions, more accurate and continuous monitoring of lakes and rivers has become possible. These satellites in recent years offer the capability to provide water level data with different along-track sampling distances. For instance, ICESat-2 offers a sampling distance of 70 cm with a footprint size of ~17 m, while Sentinel-3 provides a sampling distance of 300 m. The temporal resolution ranges from 10 days (Jason-3) to 369 days (Cryosat-2). These advances allow researchers to effectively observe and understand changes in water bodies.

The invention of satellite-based laser altimetry has brought a revolutionary advancement in our ability to monitor and study Earth's water bodies with unprecedented precision and extensive spatial coverage. This doctoral thesis aims to explore the diverse applications of ICESat-2 laser altimetry data over inland water bodies. Through these investigations, the aim is to advance our understanding of global hydrological processes and acquire valuable insights to improve water resource management strategies.

It is important to understand the error budget of the altimetric observations, one component of which is radial orbit error. Apart from the altimetric ranging errors, radial orbit errors directly influence the accuracy of the measurement of Earth's surface heights. These errors can be assessed by analyzing the difference of surface heights at ground track intersections, so-called crossover differences (XO differences). An effective approach is to model the orbit error by minimizing the residual XO difference

by the least-squares (LS) method, which is commonly known as XO adjustment. This method was implemented in the Arctic region to examine the performance of the LS adjustment over spherical cap geometry and assess the level of radial orbit error across a large-scale area. This analysis will aid in understanding the accuracy and reliability of ICESat-2 satellite orbit over the Arctic region.

The ICESat-2 satellite captures high-resolution observations of Earth's surface, including land and water, thus enabling dense measurements of heights. The green laser used in ICESat-2 has the capability to penetrate water surfaces, allowing measurements of not only the lake water level but also the nearshore water bottom. This study proposes a novel algorithm that combines ICESat-2 measurements with Landsat imagery to extract lake water level, extent and volume. This algorithm was applied to Lake Mead, resulting in a long-term time series of water level, extent and volume dating back to 1984, only derived from remote sensing data.

The ICESat-2 satellite is equipped with three pairs of laser transmitters, which concurrently generate three pairs of ground tracks. This unique characteristic enables us to derive river surface heights for each ground track, thereby calculating the river slope between two tracks, referred to as the *across-track river slope*. Moreover, when one ground track passes through the river surface, producing dense measurements, it allows us to obtain the small-scale slope for that specific track, termed the *along-track based river slope*. By using these methods, both types of slopes were estimated for the entire length of the Rhine River and subsequently generated the average slope for each reach along the river.

Zusammenfassung

Gewässer fungieren als entscheidende Bestandteile des hydrologischen Kreislaufs und dienen als Reservoire, Seen, Feuchtgebiete und Grundwasserleiter, die Wasser im Laufe der Zeit speichern und freisetzen. Die Überwachung von Veränderungen in Umfang und Volumen dieser Gewässer ist entscheidend, um ihre Rolle bei der Regulierung des Wasserflusses, der Aufrechterhaltung des Grundwasserflusses während trockener Perioden und der Unterstützung ökologischer Lebensräume zu verstehen. Darüber hinaus hilft die Identifizierung von Trends und Veränderungen in der Dynamik der Wasserflächen bei der Erkennung potenzieller Auswirkungen des Klimawandels und menschlicher Aktivitäten auf den hydrologischen Kreislauf. Historisch gesehen wurden Pegelstationen seit dem 19. Jahrhundert eingesetzt, um den Wasserstand dieser Gewässer zu überwachen. Ihre Anzahl hat jedoch seit den 1970er Jahren aufgrund von Wartungsproblemen abgenommen. Mit der Entwicklung von Satellitenaltimetriemissionen ist eine genauere und kontinuierliche Überwachung von Seen und Flüssen möglich geworden. Diese Satelliten bieten in den letzten Jahren die Kapazität, Wasserstandsdaten mit verschiedenen Abtastabständen entlang der Strecke bereitzustellen. Zum Beispiel bietet ICESat-2 einen Abtastabstand von 70 cm bei einer Fußabdruckgröße von ~17 m, während Sentinel-3 einen Abtastabstand von 300 m bietet. Die zeitliche Auflösung variiert von 10 Tagen (Jason-3) bis 369 Tagen (Cryosat-2). Diese Fortschritte ermöglichen es Forschern, Veränderungen in Wasserreservoirs effektiv zu beobachten und zu verstehen.

Die Erfindung der satellitengestützten Laseraltimetrie hat einen revolutionären Fortschritt in unserer Fähigkeit zur Überwachung und Erforschung der Wasserkörper der Erde mit beispielloser Präzision und weitreichender räumlicher Abdeckung gebracht. Diese Doktorarbeit zielt darauf ab, die vielfältigen Anwendungen von ICESat-2-Laseraltimetriedaten über Binnengewässern zu erkunden. Durch diese Untersuchungen beabsichtigen wir, unser Verständnis globaler hydrologischer Prozesse voranzutreiben und wertvolle Erkenntnisse zur Verbesserung von Strategien zur Wassernutzung zu gewinnen.

Es ist wichtig, das Fehlerbudget der altimetrischen Beobachtungen zu verstehen, zu

dem auch der radiale Bahndatenfehler gehört. Abgesehen von den Fehlerquellen bei der Altimetrie beeinflussen radiale Bahndatenfehler direkt die Genauigkeit der Messung der Erdoberflächenhöhen. Diese Fehler können durch die Analyse der Differenz der Oberflächenhöhen an den Schnittpunkten der Bodenspur, den sogenannten Crossover-Unterschieden (XO-Unterschieden), bewertet werden. Ein effektiver Ansatz besteht darin, den Bahndatenfehler zu modellieren, indem man den verbleibenden XO-Unterschied durch die Methode der kleinsten Quadrate (LS), die allgemein als XO-Ausgleichung bekannt ist, minimiert. Wir setzen diese Methode in der Arktis ein, um die Leistung der LS-Ausgleichung über sphärische Kappen-Geometrie zu untersuchen und das Niveau des radialen Bahndatenfehlers in einem großflächigen Gebiet zu bewerten. Diese Analyse wird dazu beitragen, das Verständnis für die Genauigkeit und Zuverlässigkeit der Bahndaten des ICESat-2-Satelliten über der Arktis-Region zu verbessern.

Der ICESat-2-Satellit erfasst hochauflösende Beobachtungen der Erdoberfläche, einschließlich Land und Wasser, was dichte Messungen von Höhen ermöglicht. Der grüne Laser, der im ICESat-2 verwendet wird, hat die Fähigkeit, Wasserflächen zu durchdringen, was Messungen nicht nur des Wasserstands in Seen, sondern auch des Untergrunds im küstennahen Bereich ermöglicht. Diese Studie schlägt einen innovativen Algorithmus vor, der ICESat-2-Messungen mit Landsat-Bildern kombiniert, um den Wasserstand, die Ausdehnung und das Volumen von Seen zu extrahieren. Wir wenden diesen Algorithmus auf den Lake Mead an und erhalten eine Langzeit-Zeitreihe von Wasserstand, Ausdehnung und Volumen, die bis ins Jahr 1984 zurückreicht und ausschließlich aus Fernerkundungsdaten abgeleitet ist.

Der ICESat-2-Satellit ist mit drei Paaren von Laser-Sendern ausgestattet, die gleichzeitig drei Paare von Bodenspuren erzeugen. Diese einzigartige Eigenschaft ermöglicht es uns, Flächenhöhen von Flüssen für jede Bodenspur abzuleiten und somit das Gefälle des Flusses zwischen zwei Spuren zu berechnen, das als *quer zur Spur verlaufendes Flussgefälle* bezeichnet wird. Darüber hinaus, wenn eine Bodenspur die Flussoberfläche durchquert und dichte Messungen erzeugt, können wir das Kleinskalen-Gefälle für diese spezifische Spur erhalten, das als *flussabwärts basiertes Flussgefälle entlang der Spur* bezeichnet wird. Durch die Verwendung dieser Methoden schätzen wir beide Arten von Gefällen für die gesamte Länge des Rheins und generieren anschließend das Durchschnittsgefälle für jeden Abschnitt entlang des Flusses.

Chapter 1

Introduction

Climate change poses profound challenges to hydrological systems worldwide, fundamentally altering the quantity, timing, and distribution of water resources. The intricate relationship between climate and hydrology needs a comprehensive understanding of how changes in atmospheric conditions affect the availability, quality, and management of freshwater supplies (Marques et al., 2022). According to the IPCC (2022) report, it is predicted that the global mean temperature will likely increase by 1.5°C or more from 2021 to 2040 if greenhouse gas emissions continue unabated. From 1901 to 2018, there was an observed increase in global mean sea level (MSL) by 0.2 m, with the average rate of MSL rise during the period from 1901 to 1971 of 1.3 mm/yr, increasing to 1.9 mm/yr between 1971 and 2006, and further increasing to 3.7 mm/yr between 2006 and 2018 (IPCC, 2021).

The prevailing consensus reveals that global warming and associated changes to the hydrological cycle are expected to amplify the occurrence and intensity of extreme climate events, leading to heightened incidences of severe floods and droughts (Déry et al., 2009; Jung et al., 2012; Thompson, 2012). Extreme climate events can have significant impacts on the natural environment. Therefore, understanding the impact of climate change on the temporal and spatial evolution of the hydrological cycle is a vital basis for improving the management of water resources. Conversely, the variation of the hydrological cycle is a significant indicator to predict the trend of climate change on a regional scale. In the context of rapid population growth and socio-economic development, the demand for freshwater continues to rise (Cook and Bakker, 2012). Current reports indicate that more than 2 billion people are facing high water stress, while approximately 4 billion people experience severe water scarcity for at least one month per year (Uhlenbrook and Connor, 2019). The future state of water security may be further exacerbated by the prolonged occurrence of droughts within the context of a changing climate (Seckler et al., 1999).

In addition to global climate change, human activities such as afforestation, deforestation, and urban construction have also contributed to changes in the hydrological cycle, particularly at large-scale changes in land cover or its management (Brown et al., 2005; Jiang et al., 2012a). Furthermore, the use of water for agricultural and industrial purposes can also have substantial implications for the hydrological cycle, leading to an influence on the dynamics of surface and sub-surface water content.

Over the past few decades, the management of water resources at the catchment or regional scale has faced increasing challenges concerning water quantity and quality (IPCC, 2013). Consequently, there has been a growing recognition of the need to comprehend the impact and relative significance of climate change and human-induced alterations on hydrology and water resources, leading to heightened concerns in this field (Siriwardena et al., 2006). To address these challenges, water conservancy facilities have been constructed to serve as buffers against climate extremes, facilitating water supply, flood control, and hydropower generation (Cheng et al., 2008; Fu, 2008; Lehner and Döll, 2004). Furthermore, ground observation equipment also plays a crucial role in hydrological cycles to monitor water resources and forecast climate events. Nevertheless, in recent decades, the availability of active gauging stations has significantly declined due to financial and political restrictions (Elmi, 2019). Figure 1.1 illustrates the status of basins with publicly accessible gauging stations, depicting the decrease in the number of river discharge measurement stations over time as reported by the Global Runoff Data Centre (GRDC). Therefore, due to the limited and declining number of gauging stations worldwide, the utilization of satellite technologies to monitor water bodies becomes particularly valuable (Tourian et al., 2013).

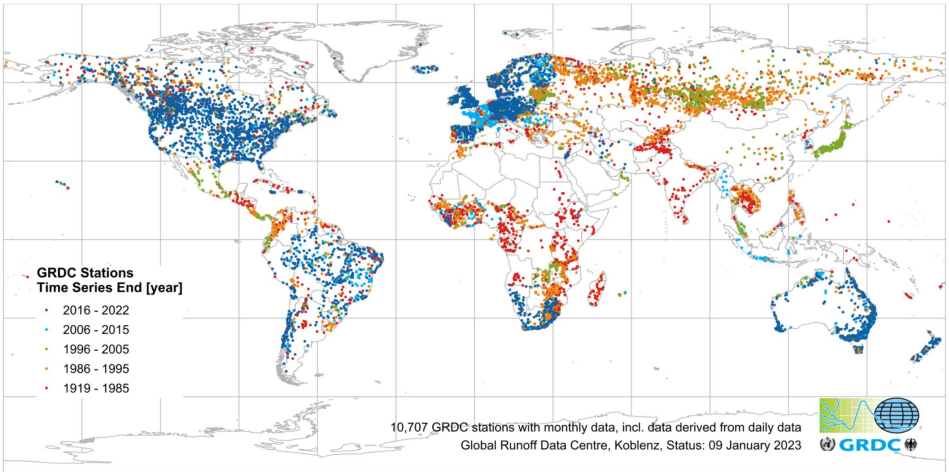

Figure 1.1: Spatial distribution of gauging stations with available runoff data in the database of GRDC in different timeframes (https://www.bafg.de/GRDC/EN/Home/homepage_node.html).

1.1 Monitoring the hydrological cycle by satellite-based technologies

Satellite-based technologies involve the use of remote sensing instruments on satellites to gather information about the Earth's surface and atmosphere. These instruments capture electromagnetic radiation reflected or emitted by the Earth, enabling the measurement of various hydrological parameters. National space agencies such as those of the USA, France, China, Japan, Canada, India, and other countries manage an extensive array of satellite systems that provide the scientific community with a wide range of measurement types and varying spatial and temporal coverage. Over the past 25 years, remarkable progress has been made in our capacity to observe the hydrological cycle, due to the maturation of satellite remote sensing, improvements in computing power, and the expansion of data-storage capabilities (Lettenmaier et al., 2015). Consequently, different types of satellites equipped with various sensors, including passive and active sensors, provide valuable data for monitoring different aspects of the hydrological cycle (Liu et al., 2012), including the global measurements of rainfall (Jeniffer et al., 2010), soil moisture (Jackson et al., 1996), snow cover (Immerzeel et al., 2009), groundwater storage change (Yeh et al., 2006), surface water level (Altenau et al., 2019), and other hydrological cycle variables.

Precipitation is a fundamental component of the hydrological cycle, and accurate estimation of precipitation is important for understanding regional water availability and predicting extreme climate events. Satellite-retrieved rainfall was first inferred using visible and thermal infrared observations, providing an estimate of rainfall volume (Lethbridge, 1967). With the launch of microwave sensors such as the Advanced Microwave Sounding Unit-B (AMSU-B) and the Special Sensor Microwave Imager (SSMI), a shift towards more direct measurements of precipitation rates was taken. Evolutions on these early missions are reflected in the dedicated Tropical Rainfall Measuring Mission (TRMM) and the latest Global Precipitation Mission (GPM), both of which use a combination of radiometers and high-resolution radar measurements. These methods integrate satellite observations with ground-based measurements, and employ a combination of statistical and physical models to generate accurate estimates of precipitation (Kidd and Huffman, 2011).

Evapotranspiration represents the combined processes of water evaporation from the

land surface and transpiration from vegetation. Accurate estimation of evapotranspiration is vital for water resource management, crop yield prediction, and understanding the energy balance of the Earth's surface. Thermal infrared sensors, such as those onboard the MODIS (Moderate Resolution Imaging Spectroradiometer) instrument, provide valuable inputs for evapotranspiration modeling (Mu et al., 2007). These techniques use surface temperature, vegetation indices, and meteorological data to derive evapotranspiration rates (Fisher et al., 2008). Although modern geostationary satellites have the capability to retrieve data with a spatial resolution of 1–2 km in the visible-to-infrared spectrum, the currently available global operational data products are limited to coarse degree-scale resolutions. This limitation poses a significant challenge for generating global estimates (McCabe et al., 2016). Therefore, it is necessary to require improvements in both retrieval algorithms and satellite measurements.

Soil moisture is a key parameter in hydrological processes, affecting plant growth, runoff, and groundwater recharge. Satellite remote sensing offers the ability to monitor soil moisture at different spatial and temporal scales. Microwave sensors, such as those onboard the Soil Moisture and Ocean Salinity (SMOS) and Soil Moisture Active Passive (SMAP) satellites, provide valuable measurements of surface soil moisture content (Kerr et al., 2012). Advanced algorithms are employed to retrieve soil moisture information from the microwave observations, considering factors like surface roughness and vegetation cover (Wagner et al., 2012). Despite no planned SMOS follow-on mission at present, the outlook for satellite remote sensing of soil moisture remains promising, with Sentinel-1 series equipped with high-resolution radars having demonstrated the capacity to provide soil moisture estimations at resolutions below 1 km and in near-real time (Paloscia et al., 2013). Spaceborne Global Navigation Satellite System-Reflectometry (GNSS-R) is also used to measure soil moisture in recent years. The concept is similar to radar altimetry, but it uses naturally occurring navigation satellite signals as the source of energy for sensing instead of actively generated radar waves (Camps et al., 2016).

Snow and ice dynamics play an important role in the hydrological cycle as an indicator of climate change. Space technologies have a wide range of applications in this field, including the monitoring of snow cover variations, estimation of snow water equivalent, tracking of glaciers and ice sheets, and observation of sea ice (Hall and Martinec, 1985). Optical sensors, such as those onboard the Landsat series and Sentinel-2 missions, capture reflected solar radiation to identify and map snow-covered areas. These sensors

provide high-resolution imagery, allowing for the detection of even fractional snow-covered areas (Dozier et al., 2009). Microwave sensors, such as the Advanced Microwave Scanning Radiometer for EOS (AMSR-E) and the Special Sensor Microwave Imager (SSMI), are used to retrieve snow water equivalent (SWE) by exploiting the differences in microwave emission between snow and underlying ground surfaces (Tedesco et al., 2015). These onboard sensors measure the microwave radiation emitted by the snowpack, allowing for the estimation of SWE at regional and global scales (De Lannoy et al., 2012). Snow and ice monitoring from space comes with several challenges. The complex interaction between snow and ice surfaces, such as changes in surface properties due to melting and refreezing, poses challenges for retrieval algorithms. Additionally, the rugged terrain and steep slopes in mountainous regions can affect the accuracy of snow and ice mapping. Therefore, continued advancements in sensor technology, integration of multiple satellite data sources, and improved algorithms for atmospheric correction and surface modeling are key areas of focus for addressing these challenges (Luo et al., 2018).

Water level and river discharge monitoring is essential for understanding river flow dynamics, flood forecasting, and water resource management. Satellite altimetry, a remote sensing technique that measures the height of water surfaces using radar- or laser-based sensors, has emerged as a valuable tool for monitoring the water level and estimating the river discharge with hydrological models (Alsdorf et al., 2007). Satellite altimetry provides a global-scale observation of water levels in rivers, lakes, and reservoirs. Altimetry sensors, such as the Jason series, Sentinel-3 missions and ICESat series, measure the distance between the satellite and the water surface by emitting radar or laser pulses and measuring the time taken for the signal to return. Altimetry-derived water level measurements are particularly significant for large river systems and remote areas where *in-situ* gauge networks may be limited. River discharge, the volume of water flowing through a river channel per unit of time, is a fundamental parameter for water resource management and flood forecasting. Estimating river discharge from altimetry data involves the integration of water level measurements with channel geometry and hydraulic models. By combining altimetry-derived water levels with width-depth relationships and slope information, river discharge can be estimated (Sneeuw et al., 2014). The integration of altimetry-derived river discharge with *in-situ* gauge observations and hydrological models enhances the understanding of river flow dynamics and improves water resource planning (Tourian et al., 2017).

Monitoring changes of water area and water storage in lakes, reservoirs, and wetlands

is important for assessing water availability, ecosystem health, and water resource management. Satellite-based optical sensors (e.g. the Landsat series and Sentinel-2 missions), provide high-resolution imagery for mapping and monitoring water bodies (Pekel et al., 2016). These sensors capture information about water reflectance, allowing for the detection of water extent changes (Elmi and Tourian, 2023). Additionally, satellite-based radar sensors, including Synthetic Aperture Radar (SAR), provide all-weather imaging capabilities to monitor the variation of water areas (Shen et al., 2019).

To monitor the changes of water storage on a global scale, the Gravity Recovery and Climate Experiment (GRACE) mission is one example, which provided high-resolution observations of temporal changes in the Earth's gravity field, enabling the estimation of changes in water storage (Tourian, 2013). GRACE provides information about changes in water storage including groundwater, ice sheets, lakes, rivers, and oceans. By analyzing the data from GRACE, scientists can estimate changes in the Earth's water mass, and this information has significant implications for understanding global water availability, sea level rise, and the impacts of climate change on the distribution of water resources. The mission has been succeeded by GRACE Follow-On, continuing its legacy of monitoring Earth's water storage variations from space.

Satellite-based technologies have significant advantages in our understanding of the hydrological cycle by providing information on various components such as precipitation, evapotranspiration, soil moisture, surface water, and snow and ice dynamics. However, several challenges exist, and ongoing research aims to address these limitations and improve the capabilities of satellite-based monitoring. The challenges encountered in satellite-based hydrological cycle monitoring are as follows:

1. **Spatial and Temporal Resolution**: Although satellite sensors have improved over time, the spatial resolution may not always capture small-scale features, such as localized precipitation patterns or changes in small water bodies. Similarly, the temporal resolution of satellite observations may not adequately capture rapid hydrological processes, such as intense rainfall events or short-term changes in soil moisture. Table 1.1 presents details regarding frequently used satellites, including their spatial and temporal coverage, as well as spatial and temporal resolution.

2. **Integration of Multiple Data Sources**: To overcome the limitations of individual satellite sensors, the integration of multiple data sources has gained attention. Combining data from different satellite missions, such as optical, microwave,

and radar sensors, can provide complementary information and enhance the accuracy of hydrological parameter retrieval. Abowarda et al. (2021) generated surface soil moisture maps at 30 m spatial resolution by fusing reflectance products of the MODIS and Landsat with land surface temperature (LST). Additionally, the integration of satellite observations with ground-based measurements, such as gauges and weather stations, can help validate and calibrate satellite-derived products. Tourian et al. (2017) used ENVISAT, SARAL/AltiKa and Jason-2 altimetry data with *in-situ* data to estimate daily river discharge over Niger River. Further research is needed to develop robust data fusion techniques that effectively integrate various data sources, facilitating a more comprehensive understanding of the hydrological cycle.

3. **Improved Retrieval Algorithms**: Accurate retrieval of hydrological parameters from satellite observations requires advanced algorithms that account for various factors affecting signal interactions with the Earth's surface. Developing robust retrieval algorithms for estimating precipitation, evapotranspiration, soil moisture, and other variables is important. These algorithms should consider the complexities introduced by surface roughness, vegetation cover, atmospheric effects, and other factors that influence the observed signal. Ongoing research aims to improve the accuracy of retrieval algorithms by incorporating advanced modeling approaches, machine learning techniques, and assimilation methods.

4. **Validation and Uncertainty Quantification**: Validating satellite-derived hydrological products is vital for ensuring their reliability and usefulness. This involves comparing satellite observations with ground-based measurements and independent datasets to assess accuracy and uncertainty. For instance, since the Shuttle Radar Topography Mission (SRTM) conducted a single comprehensive survey of global topography, it becomes impractical to directly validate this data against ground truth on a worldwide scale. Nevertheless, SRTM remains a standard reference point for assessing the performance of newer sensors and remote sensing technologies. Establishing robust validation protocols and frameworks is crucial for evaluating the performance of satellite-based monitoring techniques. Additionally, developing methods to quantify uncertainties associated with satellite-derived products is essential for effectively utilizing the data in hydrological modeling and decision-making processes.

Among the space-borne sensors, satellite altimetry offers the capability to measure surface water height at regular intervals of between 10 and 35 days (Fu and Cazenave,

2000). Despite its original design for oceanography, four decades of altimetry missions have presented an opportunity to investigate the continental hydrological cycle (Tourian et al., 2013). Nowadays, satellite altimetry is often used with other sensors, providing information about various components such as water levels, river discharge, snow and ice dynamics, and water storage. There are several advantages to using satellite altimetry to monitor the hydrological cycle. Firstly, it enables the monitoring of the hydrological cycle on a global scale, covering vast areas that may be inaccessible or challenging to observe using traditional ground-based methods (Alsdorf et al., 2007). Secondly, it has the ability to provide continuous and regular monitoring of water levels and other surface heights over time. By capturing measurements at regular repeat times, altimetry data allows for the observation of seasonal variations, long-term trends, and extreme events such as floods and droughts (Frappart et al., 2019). Thirdly, satellite altimetry measurements complement *in-situ* gauge networks, particularly in regions with limited or sparse ground-based observations. By integrating altimetry data with *in-situ* measurements, a more comprehensive and accurate assessment of the hydrological cycle can be achieved. Fourthly, by providing real-time or near real-time information on water levels and river discharge, altimetry helps in the timely detection and prediction of potential flood events. This allows for early warnings and effective responses, minimizing the risks to human life and infrastructure (Paris et al., 2016).

Consequently, satellite altimetry plays a multifaceted role in hydrological cycle monitoring, which has applications ranging from water resource management to climate change studies. By integrating altimetry data with other remote sensing datasets and assimilating it into hydrological models, we can enhance our understanding and management of the hydrological cycle.

Table 1.1: Characteristics of some typical remote sensing satellites

Satellite/sensor	Spatial coverage	Temporal coverage	Spatial resolution	Temporal resolution
TRMM	35°S–35°N	1997–2015	5 km	90 mins
MODIS	82°S–82°N	1999–now	250 m	1–2 days
SMOS	82°S–82°N	2009–now	40 km	1–3 days
SMAP	82°S–82°N	2015–now	10 km	2–3 days
Sentinel-3/SRAL	81.4°S–81.4°N	2016–now	300 m	27 days

1.2 The historical development of satellite altimetry

Satellite altimetry has undergone significant advancements since its inception in 1978, leading to its widespread use in monitoring the Earth's oceans, ice sheets, and inland water bodies. This section provides an overview of the historical development of satellite altimetry, highlighting key milestones and advancements in technology. Figure 1.2 gives an overview of main past, current and future altimeter missions since 1978.

Early missions

The development of satellite altimetry can be traced back to the early oceanographic missions. Seasat was the first satellite altimetry launched in 1978 by NASA (National Aeronautics and Space Administration), marking the beginning of satellite altimetry for oceanographic applications. Although the mission lasted for only a few months, it gave a good start for subsequent altimetry missions. The following missions Geosat launched in 1985 and ERS-1 launched in 1991, used radar altimeters to measure the height of the ocean surface and provided valuable data on ocean circulation patterns and sea level variations (Chelton et al., 2001). Due to the limitations of the accuracy and large footprints of radar, the early missions are only applicable to measure the sea level of open oceans.

Topex/Poseidon and Jason missions

A major breakthrough in satellite altimetry occurred with the launch of the satellite Topex/Poseidon (T/P) in 1992 by NASA and CNES (French Space Agency), which started the era of inland water bodies monitoring by satellite altimetry. The T/P satellite followed by the Jason-1, Jason-2, and Jason-3 missions marked a significant improvement in accuracy and spatial resolution, revolutionizing our understanding of global ocean dynamics and inland water surface variations (Fu and Cazenave, 2000). These altimetry missions employed dual-frequency radar altimeters and provided high precision measurements of sea surface height (SSH), contributing to the establishment of a long-term sea level record.

Envisat mission

The Envisat mission was launched in 2002 by ESA (European Space Agency). It carried the Radar Altimeter-2 (RA-2) providing data on oceanography, ice sheets, and land surface topography (Fu and Cazenave, 2000). Other instruments onboard Envisat

included the Medium Resolution Imaging Spectrometer (MERIS), which provided detailed observations of land and ocean color, the Advanced Along-Track Scanning Radiometer (AATSR), which measured land and sea surface temperatures, and the Global Ozone Monitoring by Occultation of Stars (GOMOS), which monitored the concentration and distribution of ozone in the atmosphere.

ICESat missions

The Ice, Cloud, and land Elevation Satellite (ICESat) was launched by NASA in 2003, with the primary objective of studying Earth's polar ice sheets and measuring changes in the global ice cover. The ICESat satellite was equipped with a laser altimeter instrument called the Geoscience Laser Altimeter System (GLAS), which emitted laser pulses towards the Earth's surface and measured the time it took for the signals back, providing measurements with smaller footprints than radar altimetry. In addition to its primary focus on ice, ICESat also provided data on land topography, vegetation canopy height, and cloud properties. These measurements were used in various applications, including studies of forest biomass, terrain mapping, and atmospheric research. ICESat operated until 2009, and its mission was followed by the ICESat-2 mission, which was launched in 2018. ICESat-2 continues the work of its predecessor, using an advanced laser altimeter to provide measurements of Earth's polar ice sheets and other geophysical parameters with even much smaller footprints than ICESat. One of the advantages of ICESat-2 is that the green laser can penetrate the water to get the bathymetry of nearshore water bodies. Another key advantage is that the onboard 3 pairs of laser beams can detect more information of the surface.

CryoSat mission

CryoSat-2 is a satellite mission launched by ESA in 2010 with the primary objective of monitoring changes in Earth's polar ice sheets and sea ice thickness. It is the successor to the original CryoSat mission, which unfortunately suffered a launch failure in 2005. The CryoSat mission introduced a new radar altimeter called the Synthetic Aperture Interferometric Radar Altimeter (SIRAL), which enabled improved measurement accuracy over ice surfaces (Wingham et al., 2006). This mission significantly advanced our understanding of ice sheet dynamics and ice thickness changes. By combining the measurements from CryoSat-2 with those from other satellite missions, scientists can monitor the mass balance of ice sheets and assess their contribution to global sea level rise. One of the key features of CryoSat-2 is its ability to measure not only the thickness of sea ice floating on the ocean but also the freeboard.

HY-2 missions

The HY-2 (Haiyang-2) missions are a series of satellite missions launched by the China National Space Administration (CNSA) with the primary objective of monitoring and studying Earth's oceans, including SSH, significant wave height (SWH), sea surface wind (SSW) speed, sea surface temperature and polar ice sheet elevation (Jiang et al., 2012b). HY-2A was the first mission of the HY-2 series launched in 2011. One of the advantages of HY-2 missions is that the microwave radiometer on HY-2A measures microwave radiation emitted by the sea surface. This information is used to determine sea surface temperature, which is an essential parameter for studying ocean circulation, heat exchange between the ocean and the atmosphere, and climate variations.

SARAL/AltiKa mission

The SARAL/AltiKa mission is a joint satellite mission between ISRO (Indian Space Research Organisation) and CNES launched in 2011. Its primary objective is to measure sea surface heights and ocean circulation. It is the first spaceborne altimeter to operate at Ka-band. The satellite carries an Argos instrument that receives and relays data from thousands of small Argos tracking beacons deployed worldwide. These beacons are attached to drifting buoys, animal tags, and other objects of interest, providing valuable information on ocean currents, animal migration patterns, and environmental parameters. The combination of altimetry and Argos tracking enables a better understanding of ocean dynamics and ecosystem monitoring.

Sentinel-3 missions

Sentinel-3 is a constellation of two satellites Sentinel-3A and Sentinel-3B, launched in February 2016 and April 2018 respectively, which are managed by ESA. The onboard Synthetic Aperture Radar Altimeter (SRAL) operates in dual-frequency, which includes both Ku-band and C-band. The Ku-band is primarily used for the Delay-Doppler Altimetry Mode, while the C-band is utilized for the Synthetic Aperture Radar (SAR) Mode (Donlon et al., 2012). This dual-frequency capability allows for improved accuracy in altimetry measurements over inland water bodies and oceans. The combination of Ku-band and C-band measurements enhances the capabilities of the altimeter and enables more precise observations of sea surface height, wave characteristics, and other parameters.

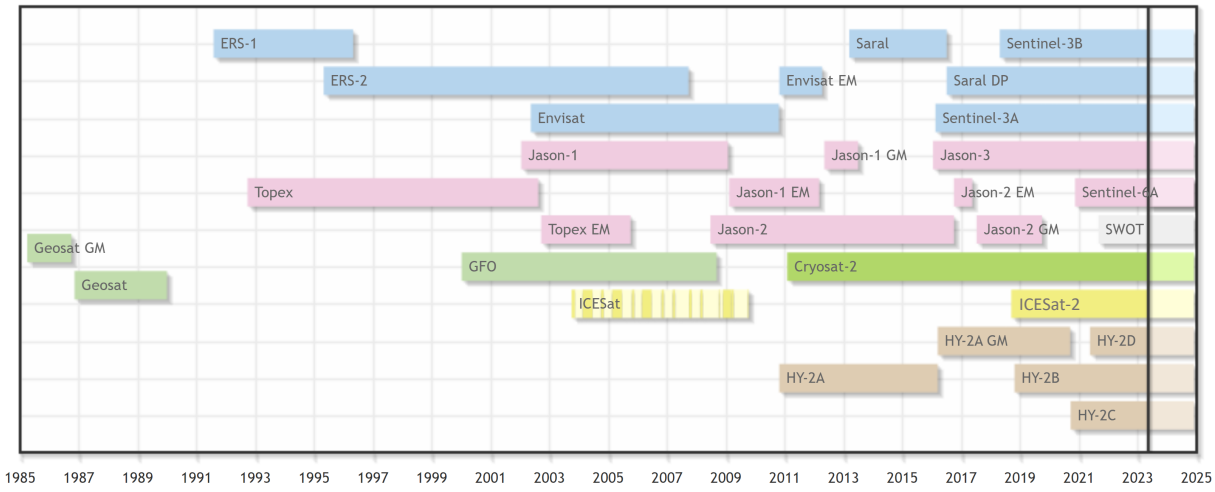

Figure 1.2: The operating time period of different altimetry satellites (https://dahiti.dgfi.tum.de/en/products/water-level-altimetry/).

1.3 Research problems of radar altimetry

Monitoring water bodies, such as lakes, reservoirs, and rivers, poses several challenges due to their dynamic nature and many remote locations. Traditional methods of data collection, such as *in-situ* measurements and aerial surveys, are limited in their spatial coverage and temporal resolution. Remote sensing techniques, particularly radar altimetry, offer an opportunity to overcome these limitations and provide comprehensive and consistent monitoring of water bodies at a global scale (Crétaux et al., 2016). The development of satellite altimetry has significantly improved our understanding of Earth's surface and its dynamic processes. From the early Seasat mission to the latest satellite radar altimeters, continuous technological advancements have improved the accuracy, resolution, and coverage of altimetry measurements. Nevertheless, there are still several challenges and research gaps that need to be discussed.

1. **Accuracy and Precision of Water Level Measurements**: Radar altimetry is a powerful tool for measuring water levels due to its ability to penetrate clouds and retrieve information over large areas. However, achieving accurate and precise water level measurements is crucial for reliable monitoring. Radar altimeters can provide measurements with centimeter-level accuracy over large lakes under favorable conditions. The problem lies in the presence of various error sources, including waveform distortions, land contamination, and interference from other surface features (Bao et al., 2009; Bonnefond et al., 2018). Measuring water bodies using radar altimetry can be more challenging than measuring open ocean surfaces. Inland water bodies often have complex topography, vegetation, and

varying water conditions, which can introduce additional sources of error. The error level might range from 10 cm to several decimeters over narrow rivers. Addressing these challenges and improving the accuracy and precision of water level measurements using radar altimetry is a key problem to be solved.

2. **Integration of Radar Altimetry with Hydrological Models**: To fully utilize radar altimetry data for water body monitoring, integration with hydrological models is necessary. This enables the estimation of key hydrological parameters such as water volume, inflows, outflows, and water storage changes. However, the problem lies in effectively assimilating radar altimetry data into hydrological models, addressing data uncertainties, and ensuring compatibility between the remote sensing observations and model dynamics (Paiva et al., 2013). Developing methodologies and frameworks for the seamless integration of radar altimetry with hydrological models is important for accurate and reliable water resource assessments.

3. **Spatial and Temporal Resolution**: Water bodies exhibit complex spatiotemporal dynamics, including diurnal and seasonal variations. Radar altimetry data, with its large spatial coverage, often has limited temporal resolution due to revisit times and orbital constraints of satellite missions, see Table 1.2. Overcoming the limitations of radar altimetry's temporal resolution and addressing the need for higher spatial resolution monitoring is essential to capture the full range of water body dynamics (Busker et al., 2019).

4. **Data Processing and Analysis**: Radar altimetry data processing involves complex procedures, including calibration, waveform retracking, and geophysical corrections (Calmant and Seyler, 2006). Additionally, analyzing large volumes of radar altimetry data requires efficient algorithms and computational resources (Schlembach et al., 2020). Developing automated and streamlined data processing techniques, along with advanced analysis methods, is critical for handling the vast amount of radar altimetry data and deriving meaningful information for water body monitoring.

The parameters of different radar altimetry missions are listed in Table 1.2. Addressing these challenges is important to achieve accurate and comprehensive assessments of water resources and understanding the dynamics of water bodies. In the future, the proposed direction of radar altimetry research should be developing innovative methodologies and algorithms to overcome these challenges and improving the technical ability to acquire more data from the Earth's surface.

Apart from these satellite radar altimeters, the use of laser technology is a new breakthrough in satellite altimetry, which makes ICESat-2 an advanced and capable altimetry satellite, providing improved accuracy, spatial resolution, and coverage for studying Earth's surfaces and monitoring changes in sea surface, inland water bodies, sea ice and other geophysical parameters. Consequently, this thesis aims to address the existing challenges encountered in radar altimetry by using ICESat-2 and advance our understanding of the hydrological cycle. The details of ICESat-2 will be introduced in Chapter 2.

Table 1.2: Parameters of different radar altimetry missions

Altimeter	Revisit Time	Altitude [km]	Inclination [°]	Band	Antenna Beamwidth[°]	Frequency [Hz]	Waveform Gates	Nominal Tracking Point	Pulse Width [ns]
SEASAT	17 days	800	108	Ku	1.59	1020	60	29.5	3.125
GEOSAT	17 days	800	108	Ku	2.00	1020	60	30.5	3.125
ERS-1	35 days	785	98.5	Ku	1.30	1020	64	32.5	3.030
TOPEX	9.9 days	1336	66	Ku	1.10	4500	128	32.5	3.125
				C	2.70	1200	128	32.5	3.125
Poseidon	9.9 days	1336	66	Ku	1.10	1700	60	29.5	3.125
ERS-2	35 days	785	98.5	Ku	1.30	1020	64	32.5	3.030
GFO	17 days	880	108	Ku	1.60	1020	128	32.5	3.125
Jason-1	10 days	1336	66	Ku	1.28	1800	104	31.0	3.125
				C	3.40	300	104	31.0	3.125
Envisat	35 days	800	98.4	Ku	1.29	1800	128	46.5	3.125
				S	5.50	450	64	25.5	6.250
Jason-2	9.9 days	1336	66	Ku	1.26	1800	104	31.0	3.125
				C	3.38	300	104	31.0	3.125
Cryosat-2	369 days	717	92	Ku	1.08	18181	128	63.0	1.5625
SARAL	35 days	800	98.5	Ka	1.29	1800	128	46.5	3.125
Jason-3	9.9 days	1336	66	Ku	1.28	1800	104	31.0	3.125
				C	3.40	300	104	31.0	3.125
Sentinel-3A/B	27 days	814	98.65	Ku	1.28	1924	128	44.0	3.125
				C	3.40	274.8	128	44.0	3.125

1.4 Objectives

The primary objective of this study is to investigate the potential of the ICESat-2 mission for monitoring water bodies in the aspects such as water level variations, surface area changes, and other hydrological dynamics. Laser technology has the capability to not only measure water levels but also determine the elevations of various other landscapes and features. When the nearshore profile measurements of the water body is combined with water area variation, it will give the opportunity to monitor the variation of the water volume. Moreover, the use of 3 pairs of onboard lasers provides a distinct advantage as it enables synchronous measurements, thereby obtaining the river surface slope, which is a key parameter for estimating the river discharge.

To enhance our comprehension of ICESat-2's capabilities, we've developed efficient methodologies employing diverse algorithms. These methods can be employed to construct hydrological models for monitoring purposes, including lakes and rivers. They have the potential to substantially enhance the effectiveness and precision of current monitoring techniques. Additionally, the results of this study can assist in water resource management, particularly in regions where water resources are scarce. Furthermore, the findings can help assess the impact of climate change on water resources by monitoring the changes in the water level, area, and volume of lakes.

The research questions in this study are:

1. Can we evaluate the error budget of ICESat-2, especially the radial orbit error with an optimal method?
2. Is it possible to use the ICESat-2 and satellite imagery-based measurements to monitor lake level, area and volume variations?
3. Can we establish a function model to estimate each parameter if we know the relationship between water level, area and volume?
4. Is it possible to determine the river surface slope if we take advantage of 3 pairs of laser beams?
5. How does the accuracy of the ICESat-2 and satellite imagery-based measurements compare to traditional field-based measurements?

1.5 Outline of the thesis

The first chapter has introduced the importance of the hydrological cycle and the satellite-based technologies normally used to monitor the hydrological cycle. Then the historical development of satellite altimetry was introduced, and the problems and limitations of radar altimetry were stated. Consequently, this thesis focuses on the new advanced satellite laser altimetry ICESat-2 and gives the aims to be addressed in this study.

The second chapter will provide the basic principles of laser altimetry and the properties of ICESat-2. This chapter will detail the previous generation of laser altimetry ICESat, the current relatively new generation ICESat-2, and the mission GEDI (Global Ecosystem Dynamics Investigation).

In the third chapter, the radial orbit error of the ICESat-2 satellite will be discussed. *Crossover analysis* was used to evaluate the radial orbit error level. In this method, function models of the radial orbit correction were established, and the performances of different models were analyzed. This chapter is an augmented version of the paper Wang and Sneeuw (2024).

In the fourth chapter, a methodology for monitoring lakes will be presented. A methodology was developed for establishing a relationship between the lake water level, area and volume. Each step of the algorithm will be introduced in detail. This method can be used to monitor the lake variation in the long term. Then the results were validated with *in-situ* data and other datasets.

Chapter 5 will introduce the ability of ICESat-2 to determine the river surface slope. The 3 pairs of lasers were fully used to estimate the local slope with the across-track and along-track directions. The slope variation was generated and the chainage slope of the entire river was performed. Then the satellite-derived slopes were compared with the measurements from the boat.

Chapter 6 will discuss the findings of the study, their implications for water resource management, and understanding the impact of climate change on water resources. Finally, the conclusions and recommendations will be provided for further research.

Chapter 2

Laser altimetry

2.1 Basic principles and applications

Laser altimetry is a remote sensing technique used to measure the elevation of the Earth's surface by employing laser pulses. It provides highly accurate and detailed information about the topography and structure of the Earth's surface, including the Earth's landforms, vegetation, and man-made structures (Cohen et al., 1987).

The basic principle of laser altimetry involves emitting a laser beam from an aircraft or satellite towards the ground and measuring the time it takes for the laser pulse to travel to the target and back to the sensor (Blair et al., 1994). By knowing the speed of light, the precise time measurement allows for the calculation of the distance between the sensor and the surface.

The following is a simple step-by-step process of laser altimetry:

1. **Emitting laser pulses**: A laser source emits short pulses of light in the form of laser beams towards the Earth's surface. These pulses typically have a narrow beam divergence, ensuring that the laser energy is concentrated and focused on a specific target area, e.g. ~70 m diameter for ICESat and ~17 m diameter for ICESat-2 (Neumann et al., 2019).

2. **Pulse reflection**: When the laser pulse reaches the surface, it interacts with the various objects and features present there. The pulse can be reflected, scattered, or absorbed, depending on the properties of the surface and objects encountered. The reflected laser light returns to the sensor.

3. **Measurement of return time**: The altimeter measures the time it takes for the laser pulse to return to the sensor. This measurement is highly precise with several centimeters ranging error and allows for accurate determination of the distance between the sensor and the surface.

4. **Calculation of elevation**: Using the known speed of light, the altitude or elevation of the surface is calculated by multiplying the time taken by the speed of light and dividing it by two. This provides the distance between the sensor and the surface, commonly referred to as the range. During the propagation of the pulse, geophysical corrections should be considered due to atmospheric disturbances and Earth's tides. Therefore, the elevation should be corrected in this step. The basic equation of satellite altimetry is

$$h = r_{\mathrm{s}} - R, \tag{2.1}$$

where h is the SSH above the reference ellipsoid, r_{s} is the height of the satellite with respect to the reference ellipsoid, and R is the range from the satellite to the Earth's surface.

5. **Data collection and analysis**: As the laser altimeter continues to emit laser pulses and measure their return times, a large amount of data is collected. This data is then processed and analyzed to create a detailed topographic map or a three-dimensional representation of the Earth's surface.

Laser altimetry has been used in various applications, such as mapping and monitoring ice sheets, glaciers, and polar regions, studying changes in forest canopy height and biomass, assessing coastal erosion and measuring the elevation of land surfaces (Zwally et al., 2002). There are several notable satellite laser altimeters used in different applications, as follows:

1. **Mars Orbiter Laser Altimeter (MOLA)**: MOLA is an instrument on NASA's Mars Global Surveyor (MGS) spacecraft, which orbited Mars from 1997 to 2006. MOLA employed laser altimetry to create a detailed global topographic map of Mars. By measuring the time it took for the laser pulses to return from the Martian surface, MOLA provided scientists with valuable data about the planet's topography, including the height of mountains, the depth of canyons, and the elevation of various Martian features (Smith et al., 2001).

2. **Lunar Orbiter Laser Altimeter (LOLA)**: LOLA is an instrument on NASA's Lunar Reconnaissance Orbiter (LRO) spacecraft, which has operated from 2009 till now. LOLA studies the moon in the same way that MOLA studied Mars. LOLA's primary measurement is surface topography, and in addition the instrument provides ancillary measurements of surface slope, roughness and 1064 nm reflectance (Smith et al., 2010). The data from LOLA was used to generate a global lunar

topographic model and geodetic grid that serves as the foundation of essential lunar understanding.

3. **Geoscience Laser Altimeter System (GLAS)**: GLAS is an instrument carried aboard NASA's ICESat mission. It was specifically designed to study the Earth's polar ice sheets and assess changes in their mass and thickness over time. GLAS uses lasers to measure the distance between the satellite and the ice surface, allowing scientists to monitor changes in ice volume and track the dynamics of ice sheets (Abshire et al., 2005).

4. **Advanced Topographic Laser Altimeter System (ATLAS)**: ATLAS is an advanced laser altimetry instrument carried by NASA's ICESat-2 satellite, launched in 2018. It is designed to continue the work of its predecessor, ICESat, by monitoring changes in the Earth's polar ice sheets, sea ice thickness and land topography (Markus et al., 2017). ATLAS uses a high-power laser to collect precise elevation data and track variations in the height of the Earth's surfaces with exceptional accuracy.

5. **Global Ecosystem Dynamics Investigation (GEDI)**: The GEDI instrument was launched to the International Space Station (ISS) in December 2018 and was designed to study the Earth's forests and vegetation structure in three dimensions. Such observations are critical for accurately assessing the existing biomass of forests, and how changes in this biomass caused by human activities or variations in climate may impact atmospheric CO_2 concentrations (Dubayah et al., 2020).

The following sections in this chapter will introduce details of GEDI, GLAS and ATLAS instruments, as well as their respective satellite platforms.

2.2 GEDI

GEDI was deployed to the ISS in December 2018 and retired in January 2023. GEDI measurements were conducted both during daytime and nighttime, providing continuous coverage over terrestrial land surfaces. This coverage includes the diverse tropical and temperate forest regions of the Earth. The GEDI instrument employed an active across-track pointing system to mitigate coverage gaps caused by orbital variations of the ISS. These variations arise due to the non-repetitive nature of the ISS orbit and the potential occurrence of orbital resonances that lead to significant coverage gaps. With

its pointing capability, GEDI can precisely target specific plot locations or other areas of interest with an accuracy of approximately 35 m (Dubayah et al., 2020). GEDI's approach involved a systematic and evenly distributed distribution of laser tracks across the Earth, following a predefined set of Reference Ground Tracks (RGTs) designed to optimize sampling.

The GEDI instrument included three identical near-infrared lasers. Two were used at full power, while the other one was split into two beams, for a total of 4 beams. Each of the beams was optically dithered across-track to create a total of 8 ground tracks, with a between-track spacing of ~600 m, and a total across-track width of ~4.2 km. The average along-track distance between the footprints is 60 m and the footprint size is 25 m, resulting in almost continuous along-track coverage. It is operated by emitting laser pulses in 1064 nm wavelength light, where it interacts with the leaves and branches within the footprint. The laser system operated at a frequency of 242 pulses per second. GEDI used an advanced laser remote sensing system that relies only on the analysis of the returned laser waveform. This full waveform provided valuable information for deriving various canopy and waveform metrics, including canopy height, canopy vertical profile, and Relative Height (RH) energy metrics (Tang et al., 2012), as well as topographic surface elevation.

Figure 2.1 shows a sample of the reflected waveform when the laser detects the vegetation on the ground. The light brown area under the curve represents the return energy from the canopy, while the dark brown area signifies the return from the underlying topography. The black line is the cumulative return energy, starting from the bottom of the ground return (normalized to 0) to the top of the canopy (normalized to 1). RH metrics give the height at which a certain quantile returned energy is reached relative to the ground (the center of the ground return). The diagram on the right shows the distribution of trees that produced the waveform on the left.

Here are some key features and objectives of the GEDI mission:

1. **3D Forest Structure**: GEDI aimed to provide a comprehensive assessment of the Earth's forest structure in three dimensions. It measured the heights and vertical distribution of vegetation, including the canopy, branches, and understory, providing valuable insights into forest biomass, carbon stocks, and biodiversity.

2. **Global Coverage**: GEDI covered a broad range of latitudes, from 51.6°N to 51.6°S, allowing for a global assessment of forests and vegetation. The instrument collected data along the ISS orbit path, providing a unique perspective for studying

various forest types, including tropical, temperate, and boreal forests. GEDI can be rotated up to 6°, allowing the lasers to be pointed up to 40 km on either side of the ISS ground track. This capability was used to sample the Earth's land surface as completely as possible, filling in gaps due to clouds. During GEDI's operating time, about 10 billion cloud-free observations of the Earth's surface were acquired. These observations can then be gridded into regular coverages of varying resolution, such as 1 km grid cells.

3. **Ecological Research**: GEDI data supports ecological research by facilitating a better understanding of forest dynamics, habitat structure, and ecosystem health. It helps scientists monitor forest disturbance, such as deforestation, regrowth, and degradation, and assess the impact of these changes on biodiversity, carbon cycling, and climate regulation.

4. **Climate Modeling**: GEDI data is valuable for improving climate models and understanding the role of forests in the global carbon cycle. By providing accurate measurements of forest structure and biomass, GEDI contributed to estimating carbon stocks, carbon sequestration rates, and the overall impact of forests on Earth's climate system.

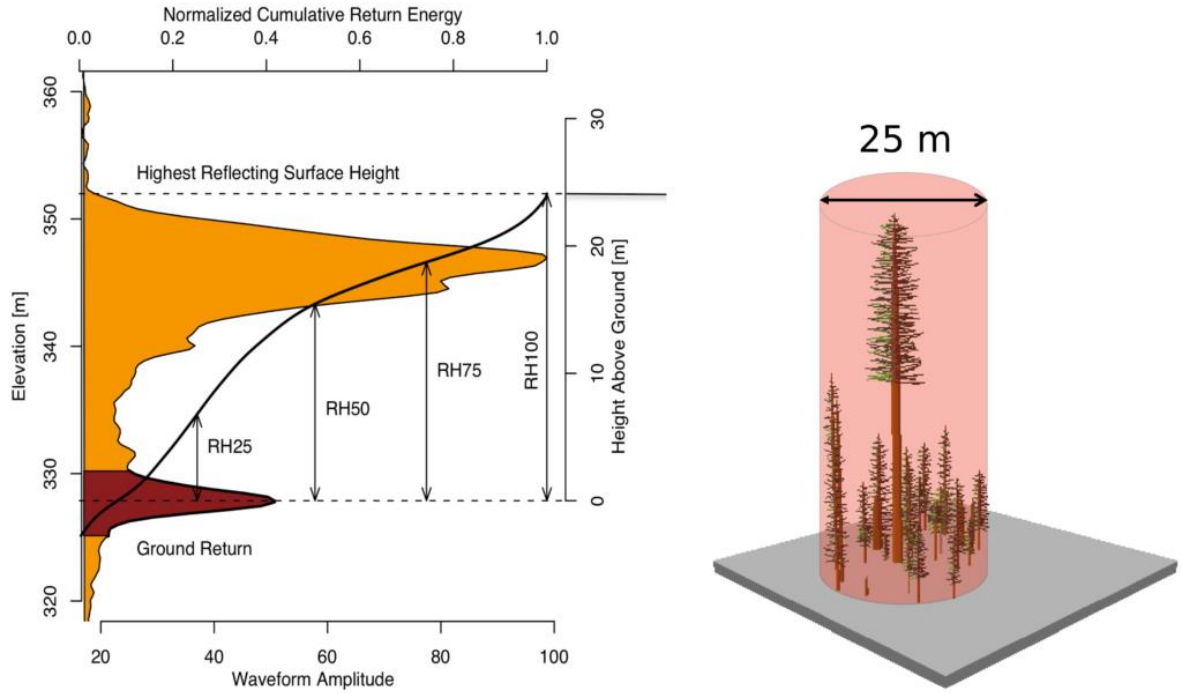

Figure 2.1: A sample of the reflected waveform of one laser pulse detecting the vegetation (https://gedi.umd.edu/mission/technology/).

2.3 ICESat and GLAS

The main objective of ICESat was to ascertain inter-annual and long-term variations in mass within polar ice sheets, elucidate the factors influencing these changes in mass balance (such as polar precipitation, ice melting, or ice flow acceleration/deceleration), and evaluate their consequences on global sea level (Zwally et al., 2002). Changes in ice mass arise from imbalances between inputs (snowfall, condensation, and occasional rainfall) and outputs (evaporation, melt runoff, iceberg discharge, and snow drift removal). Other scientific objectives of ICESat include: global measurements of cloud heights and the vertical structure of clouds and aerosols; precise measurements of land topography and vegetation canopy heights; and measurements of sea ice roughness, sea ice thickness, ocean surface elevations, and surface reflectivity.

ICESat revolutionized global measurements of vertical cloud and aerosol structure, optical depth, planetary boundary layer height, and polar tropospheric and stratospheric clouds, providing unprecedented insights. The laser data, offering direct and explicit information, has the ability in validating cloud and aerosol retrievals from passive sensors on other Earth Observing System (EOS) satellites (Zwally et al., 2002). While passive sensors excel at observing cloud tops, their capacity to distinguish multi-level cloud formations and determine vertical cloud distribution is hindered by upper-layer clouds. ICESat's laser, on the other hand, offered distinct advantages with direct cloud height measurements, aerosol distribution monitoring over land, and year-round measurements of polar clouds and aerosols. Enhanced cloud measurements, particularly in polar regions, are crucial for comprehending the radiation balance and refining atmospheric precipitation modeling, both essential factors impacting surface ice mass balance. Moreover, laser measurements play a crucial role in enhancing digital elevation models, particularly in regions where geodetic control is limited, such as higher-latitude areas. Utilizing repeat laser profiling and crossover analysis, the mission enables the detection of land elevation changes resulting from geologic processes, including soil erosion, sediment transportation, and volcanic magma inflation. Furthermore, ICESat facilitates the monitoring of inland water levels and the measurement of vegetation height in low-relief regions. An important capability of the mission was its accurate spacecraft pointing to off-nadir targets of opportunity, such as volcanic aerosol plumes or flood-affected areas.

GLAS has three lasers (designated Laser 1, 2 and 3) mounted on a rigid optical bench, with only one laser operating at a time (Abshire et al., 2005; Zwally et al., 2002). Each emitter produces a 1064 nm wavelength laser pulse, but a doubler crystal produces

a 532 nm wavelength laser pulse, which yields a more sensitive determination of the vertical distribution of clouds and aerosols (Spinhirne et al., 2005). The expected precision for the surface elevation measurements is better than 15 cm, calculated as an average value over laser footprints with a diameter of ~70 m, and spaced with an interval of ~170 m along the track (Zwally et al., 2002). ICESat's orbit is at an altitude of 600 km with an inclination of 94°. The 8-day repeat orbit was used during the calibration phase of the ICESat mission since it enabled the flight over a specific calibration site every 8 days. The 183-day repeat orbit was designed to be the actual operational orbit after calibration. The onboard Global Positioning System (GPS) system provides radial orbit determinations with an accuracy better than 5 cm, while the star trackers in GLAS and on the spacecraft will allow for horizontal footprint localization to 6 m. Precise control of the laser beam's spacecraft pointing will enable repeat tracks over the ice sheets to be maintained within $\pm$35 m on the surface.

On February 20, 2003, the initiation of laser firing was commanded for the first laser within the GLAS instrument on board the satellite. The initial data obtained displayed robust, leading to high-quality measurements of surface and cloud elevations (Webb et al., 2012). However, after a mere two weeks, a rapid decline in laser energy was observed, surpassing the anticipated rate, and potential issues with the laser pump diodes were indicated. This diminishing trend persisted until March 29 when Laser 1 ceased firing after 36 days of operational activity in orbit. Upon conducting an analysis of the Laser 1 failure, a recommendation was made to operate Laser 2 at a lower temperature, aiming to decelerate the growth of gold-indide compounds (Abshire et al., 2005). Furthermore, considering the projected reduced lifetimes of the remaining lasers, the mission operations plan was modified to strike a balance between spatial and temporal coverage requirements in alignment with the scientific objectives. Consequently, the initially intended 183-day repeat cycle was substituted with a 91-day repeat cycle (Schutz et al., 2005). The main characteristics of ICESat's repeat orbits are summarized in Table 2.1. However, it was decided that GLAS would solely operate during a 33-day near-repeat subcycle within this revised orbit, occurring three times annually: Winter (February/March), Spring (May/June), and Fall (September/October). The last laser failed on 11 October 2009, and following attempts to restart it, the satellite was retired in February 2010. Between 23 June 2010 and 14 July 2010, the spacecraft was maneuvered into a lower orbit in order to speed up orbital decay. On 14 August 2010, it was decommissioned, and on 30 August 2010 it reentered the atmosphere.

Table 2.1: Main characteristics of ICESat's repeat orbits

Parameters	8-day repeat	91-day repeat	183-day repeat
Nodal days (α)	8	91	183
Reference ground tracks (β)	119	1354	2723
Ratio β/α	14.875	14.879	14.880
Inclination	94°	94°	94°

Consequently, the challenges faced by ICESat underscored the importance of developing robust and redundant systems for future satellite missions. ICESat's laser failure contributed to the design and implementation of ICESat-2, ensuring a more reliable and capable platform for studying Earth's ice sheets and related processes.

2.4 ICESat-2 and ATLAS

2.4.1 Principles and properties

The ICESat-2 mission, launched in September 2018, represents the second generation of NASA's ICESat laser altimetry missions. The ICESat-2 satellite uses a photon-counting lidar system along with supplementary components such as GPS and star cameras to conduct three fundamental measurements: the time for a photon to travel the round-trip from ATLAS to the Earth's surface, the precise pointing direction of ATLAS when the photon is emitted, and the spatial coordinates of the satellite when the photon is detected by ATLAS (Jasinski et al., 2021). ICESat-2 is significantly different from its predecessor, ICESat/GLAS, in terms of its operational characteristics. ICESat-2 completes 1387 revolutions within a single repeat cycle of exactly 91 nodal days. While ICESat/GLAS used ~80 mJ lasers with a firing rate of 40 Hz to enable full waveform detection (Abshire et al., 2005; Schutz et al., 2005), ICESat-2 employs a much higher firing rate. The ATLAS instrument operates by emitting green (532 nm) laser pulses at a frequency of 10 kHz, with a footprint size of ~17 m in diameter. Considering the velocity ~7 km/s of the spacecraft at the nominal ~500 km orbit altitude of ICESat-2, this results in a transmission of approximately one laser pulse per ~70 cm along the ground tracks. ICESat-2 carries the ATLAS with 3 pairs of beams (GT1L/GT1R, GT2L/GT2R and GT3L/GT3R), in which "GT" means "Ground Track" and "L/R" means "Left/Right". Each emitted laser pulse is diffractively split by an optical element within ATLAS, resulting in the generation of six distinct beams arranged in three pairs. The distance between two neighboring pairs in the across-track direction on the Earth's surface is

about 3.3 km. Each pair consists of a strong beam with high energy (175 ± 17 μJ) and a weak beam with low energy (45 ± 5 μJ), with a distance of 90 m between the two beams in each pair on the Earth's surface (Neumann et al., 2019), as shown in Figure 2.2. The comparison of key parameters between ICESat and ICESat-2 is shown in Table 2.2.

Table 2.2: Comparison between ICESat and ICESat-2

Parameters	ICESat	ICESat-2
Repeat cycle (days)	91	91
Inclination (°)	94	92
Mean altitude (km)	600	500
Reference ground tracks	1354	1387
Footprint (m)	~70	~17
Along-track sampling distance (m)	~170	~0.7

Each laser pulse includes ~10^{14} photons from the ATLAS, traveling through the atmosphere to the Earth's surface, and returning through the atmosphere and back into the ATLAS photon detector.

For surfaces with high reflectivity and under clear sky conditions, it is expected that around ten signal photons originating from a single strong beam will be detected by ATLAS per transmitted laser pulse. Concurrently, background photons emitted by sunlight at the same 532 nm wavelength may also reach the detector, leading to their inclusion in the ATLAS recordings. Regardless of their source, any photon for which ATLAS registers an arrival time is referred to as a photon event. The quantity of photon events captured by ATLAS is contingent upon factors such as the Earth's surface geometry and reflectance, solar conditions, as well as scattering and attenuation in the atmosphere. The number of recorded photon events ranges from nearly zero events per pulse over non-reflective surfaces, to no more than twelve events per pulse over highly reflective surfaces (Neumann et al., 2021).

In order to reduce the volume of data downlinked to Earth, ICESat-2 employs onboard flight software to identify and transmit data pertaining to photon events that are most likely to correspond to the laser pulse's returned photons, while also providing atmospheric information. These transmitted pulses are spaced approximately 30 km apart in their one-way journey. Consequently, received photon events exhibit an inherent height ambiguity of approximately 15 km. Thus, ICESat-2 is capable of characterizing

only the lowest 15 km of the Earth's atmosphere. The onboard software counts photon events and generates a histogram covering the lowest 14 km of the atmosphere, employing vertical bins of 30 m. These atmospheric histograms aggregate the number of photon events over four hundred consecutive laser transmit pulses, resulting in the generation of an atmospheric histogram every 0.04 s, spanning ~280 m of along-track distance.

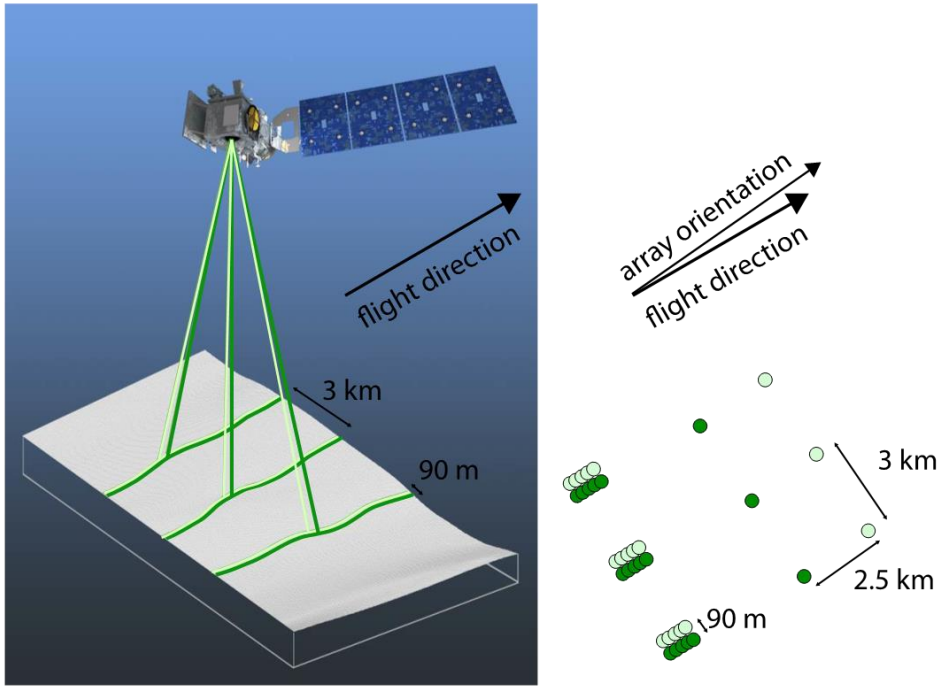

Figure 2.2: Schematic diagram of ICESat-2 and its 3 pairs of beams (Neumann et al., 2021).

Due to the large volume and rate of photon events, it is not feasible for ATLAS to assign a unique time tag to each received photon event and transmit the corresponding information. Instead, the flight software establishes a range window, spanning at least 500 m and not exceeding 6 km, within which detected photons are assigned time tags and designated as photon events. The width of this window primarily depends on factors of the surface types (e.g. ocean, ice, inland water and land) (Leigh et al., 2014). Within the defined range window, ATLAS assigns time tags to the received photons and generates altimetric histograms based on these events. The onboard software utilizes these histograms to identify the surface and determine which photon event data should be downlinked to the Earth for each beam. The range of photon time tags that are downlinked to Earth is referred to as the telemetry band.

While lower-level data products operate on individual photon events, higher-level geophysical data products employ photon aggregations to ascertain the ellipsoidal height of the Earth, canopy height, structure, and other relevant geophysical parameters.

2.4.2 Overview of data products

The description of the ICESat-2 data products and their interconnections can be observed in Figure 2.3. The ATL01 algorithm reformats and unpacks the Level 0 data from ICESat-2, then converts it into engineering units. Subsequently, the ATL02 processing applies instrument corrections to refine these data. This includes correcting photon event time tags for temperature and voltage variations in the ATLAS electronics, as well as eliminating biases from timing and pointing measurements. The Precision Orbit Determination (POD) and Precision Pointing Determination (PPD) use data from ATL02 to determine the position of the ICESat-2 observatory as a function of time and the pointing vector of the observatory as a function of time.

ATL03 integrates the data products derived from POD, PPD, and ATL02 to generate a Level 2 product that includes geolocated ellipsoidal heights for each photon event downlinked from ATLAS with time tags. These heights are corrected with various geophysical parameters, such as atmospheric corrections and tides (Neumann et al., 2021). Additionally, the data are classified into two categories: likely signal photon events and likely background photon events.

The raw atmospheric profiles of each beam are extracted from ATL02 to generate atmospheric data products. ATL04 generates normalized relative backscatter profiles, while ATL09 produces calibrated backscatter profiles, atmospheric layer heights and associated atmospheric parameters.

All Level 3A data products draw from the geolocated photon heights in ATL03 and the atmospheric parameters from ATL09. ATL06 provides along-track land ice ellipsoidal heights, ATL07 provides along-track sea ice and polar ocean heights, and ATL08 provides along-track terrestrial ellipsoidal heights and related metrics for vegetation heights. ATL10 contains sea ice freeboard for the Arctic and Antarctic seas and associated parameters. Ocean heights are available in ATL12, while ATL13 provides inland water heights.

The Level 3B data products consist of gridded products derived from the along-track products of Level 3A. ATL11, ATL14, and ATL15 are gridded land ice products that include land ice height time series, annually gridded land ice heights, and gridded land ice height change. ATL20 and ATL21 provide gridded sea ice data for the Arctic and Antarctic regions. Gridded terrestrial data is available in ATL18, while ATL19 provides gridded mean sea surface heights. Lastly, ATL16 and ATL17 offer weekly and monthly gridded atmospheric data products.

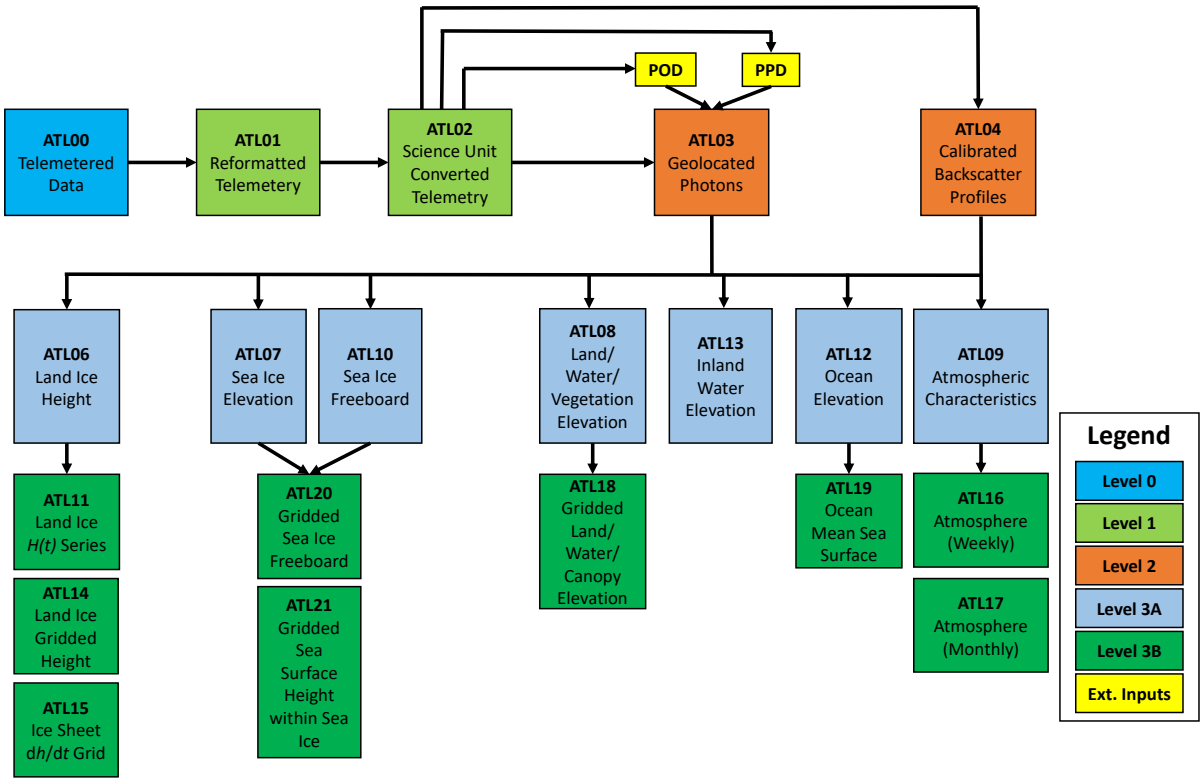

Figure 2.3: The flow of ICESat-2 data processing from Level 0 to Level 3. The color indicates data product levels, while the text reports data product number and short name.

In this thesis, only ATL03, ATL12 and ATL13 data sets from ICESat-2 are used for the following chapters. ATL03, as the lower level data product, has an along-track sampling distance of 70 cm. The ATL03 datasets include all raw points (signal points and noisy points), each of which is tagged with a unique time, latitude, longitude, and elevation above the WGS84 ellipsoid (Neumann et al., 2021). The geophysical errors such as atmospheric errors, polar tide and solid tide are corrected in the datasets. ATL12 is generated from the ATL03 level-2 geolocated photon data product and includes the data of open oceans and ice-covered oceans. ATL12 only processes ATL03 data from strong beams, and generates data with length scales between 70 m (ice-ocean) and 7 km

(open ocean), as determined by an adaptive surface finding algorithm (Morison et al., 2019). For ATL13, the length of these segments along the track can vary from 30 to several hundred meters, depending on the number of signal photons received per pulse (Jasinski et al., 2021).

Chapter 3

Crossover analysis

The ICESat-2 mission aims to obtain height measurements that create a global portrait of Earth's radial dimension, gathering data to monitor changes of terrain including glaciers, sea ice, forests and more. Therefore, it is important to understand the error budget of the observations, one component of which is radial orbit error. Apart from the altimetric ranging errors, radial orbit errors directly influence the precision of the measurement of SSH. These errors can be assessed by analyzing the difference of SSH at ground track intersections, so-called crossover differences (XO differences). An effective approach is to model the orbit error by minimizing the residual XO difference by the least-squares method. XO differences are assumed to be caused by the difference of radial orbit errors between ascending and descending arcs, the sea surface variation, mispointing, and measurement errors. Since the sea surface variation in a short time interval and measurement errors can be considered as a random variable, these residuals can be reduced by the method of XO adjustment.

3.1 Introduction

The polar oceans are often not included in the global sea level estimations. It can be seen in many global sea level maps that the Arctic region is usually blank. This is because of the difficulty to obtain polar sea level measurements, including seasonal to permanent sea-ice cover, low orbital inclinations of some altimetry satellites, insufficient geopotential models, and radial orbit errors of satellites (Rose et al., 2019). There are certain limitations of using radar altimeters for sea-ice surface measurements. Firstly, the radar signal's waveform can be complex and may have multiple peaks due to ice within the large radar footprint, making it difficult to extract the exact sea surface reflected signal. Secondly, the radar can penetrate snow cover, leading to errors in estimating ice-freeboard thickness. In contrast to radar altimeters, lasers have advantages that overcome certain drawbacks. One advantage is that the footprint of

the laser pulse is smaller, which can lead to more precise measurements. Additionally, laser reflection comes directly from the snow surface, avoiding potential errors caused by snow penetration.

In order to better understand the polar regions, ICESat laser altimetry satellite was launched in January 2003 and operated until August 2010. Its primary aim was to measure changes in the Earth's ice sheets, sea ice thickness, and land topography (Schutz et al., 2005; Xing et al., 2010; Zwally et al., 2002). ICESat-2, as the successor to the ICESat mission, carrying the Advanced Topographic Laser Altimeter System (ATLAS), has the same aim as its predecessor. Thanks to its small footprint, the technology of a laser system can provide relatively precise ranging measurements compared to radar altimetry. For instance, ATLAS produces overlapping footprints with a diameter of ~17 m and a spatial resolution of 70 m along the ground track (Markus et al., 2017). Even though nowadays altimeter orbits are precisely determined by orbit tracking systems (e.g. Laser, GPS and DORIS), residual radial orbit errors of satellite altimeters still can be identified. Therefore, analysis of residual orbit error due to geopotential model error and other forces is important for understanding the accuracy of the ICESat-2 satellite orbit, particularly for improving the quality of height observations over sea ice regions.

An effective method for estimating orbit errors is the so-called crossover adjustment, which is widely used for assessing the level of radial orbit errors and improving the quality of observations in satellite altimetry (Bosch, 2007). The ground tracks of a single satellite cross each other after certain time intervals. The intersection of two ground tracks is called *crossover* (XO), which will be observed by the satellite altimeter twice in one repeat cycle (Bosch, 2004; Bosch et al., 2014). If the sea surface does not change, the SSH values from two measurements at the XO should be identical. However, the XO difference cannot be avoided in reality due to radial orbit errors, even if the sea surface variation between two epochs and the altimetric measurement errors are known. In contrast to the static nature of the Mars surface during the XO analysis of laser altimetry data from the Mars (Neumann et al., 2001), the sea surface variability (Δh) within a short timeframe in the context of Earth's altimetry data should be taken into account as a stochastic model statistically, i.e. $\mathrm{E}\{\Delta h\} = 0$. Consequently, the parameters (unknowns) of an error function model describing radial orbit errors can be estimated by minimizing residual XO differences in a least-squares (LS) adjustment (Schrama, 1989; Shum et al., 1990).

In general, the error function model is described as a function of time or the track length (Bosch, 2007). The most popular parameterization for regional applications is a simple bias or bias-and-tilt model (Fu and Vazquez, 1988). The parameters (bias and tilt) for each track are determined by minimizing the residual XO differences (Cheney and Marsh, 1981; Fu and Chelton, 1985). When the length of a track is a small fraction of one revolution, this parameterization is adequate. However, this is not always the case. For global applications, enhanced parameterizations are to represent the radial orbit error using higher-degree polynomials (Rapp, 1979) or Fourier series (Douglas et al., 1984). Consequently, the choice of parameterization is a balance between efficiency and simplicity. XO analysis can be categorized into two distinct methods. The single-satellite XO analysis uses intersected points between ascending and descending segments of one satellite to estimate the orbit errors (Van Gysen and Coleman, 1997). On the other hand, dual-satellite XO analysis aims to evaluate the relative orbit error for one satellite, where the other satellite is assumed to be error-free and serves as the reference (Bosch et al., 2014). No matter which model is selected to represent the radial orbit error, it will have a corresponding null space that cannot be assigned to the radial orbit error of one satellite altimetry. The treatment of this rank defect requires special attention. It can be partially or fully determined through external measurements or constraints, for instance, in the comparison of the TOPEX/Poseidon (T/P) orbits with orbits obtained using the T/P GPS Demonstration receiver by Bertiger et al. (1994). In the case of the unavailability of any external references, alternative methods must be involved to overcome the singularity of the estimation problem. This has commonly been done by using master arcs, or by putting extra weight on the diagonal of the normal equation matrix of the XO adjustment (Douglas et al., 1984; Houry et al., 1994; Rapp, 1979; Tai, 1988).

In our study, we only use the single ICESat-2 satellite to evaluate its orbit error level over the Arctic region. To fulfill this aim, the XO analysis is normally operated by the following steps:

(1) identifying the XO points of ascending and descending tracks within a repeat period;

(2) calculating XO differences between ascending and descending measurements at the XO points (inverse barometer, sea state bias, tides, and other geophysical corrections should be applied);

(3) defining the functional model to apply the least-squares adjustment;

(4) solving the singular problem of the adjustment, which is necessary to choose some forms of constraints to ensure a unique solution (either fixing certain tracks or choosing a minimum-norm solution).

In this chapter, two different strategies for radial orbit error analysis over the Arctic region are followed, in the first strategy, the parameters of the error model represent one full revolution of the ground track. In the second strategy, the parameters of the error model represent one ascending or descending arc segment separately. We present the results of our analysis of satellite orbit differences in the radial direction and analyze the rank deficiencies of two strategies to solve the singular problem.

3.2 Study area and data

The study area for this research is the Arctic region, which includes the Arctic Ocean and surrounding land masses. The Arctic region is characterized by its unique geography and climate, with extensive sea ice cover, rapidly changing ice dynamics, and sensitive ecosystems (Yamanouchi and Takata, 2020). Therefore, the study area is of particular interest due to the need for accurate satellite altimetry measurements for monitoring and understanding changes in the cryosphere. The Arctic region is a polar region located from the Arctic Circle (66.5°N) to the north pole (90°N) of the Earth. The inclination of the ICESat-2 orbit is 92° (Markus et al., 2017), i.e. the northernmost data coverage is 88°N, so it can measure almost the whole area of the Arctic region. Thus, the advantages of ICESat-2 for the Arctic region are one of the reasons why we select it as our study area. A second reason is that previous studies of XO analyses chose rectangular or diamond-shaped regions. Consequently, XO analysis for the Arctic region will help to understand the performance of the LS adjustment over spherical cap geometry.

3.2.1 ICESat-2 ATL12 ocean surface elevation product

ICESat-2 carries the ATLAS with 3 pairs of beams (GT1L/GT1R, GT2L/GT2R and GT3L/GT3R) as mentioned in Chapter 2. As this study focuses on the radial orbit error, here we just use the data in the nadir beam. ATL12 Ocean Surface Elevation, which is one of the level-3 products of ICESat-2, is employed in this research. As the Arctic region is defined here as the spherical cap inside the Arctic Circle, only the SSH measurements with coordinates inside the region between 66°N and 88°N are used

from each ground track. In order to balance the influence of the non-stochastic SSH variation within a long timeframe and the number of redundant observation equations in the LS adjustment, we avoid using all ground tracks in the whole repeat cycle. In our research, we opted to focus on ground tracks spanning a 15-day duration, which corresponds to roughly one-sixth of a complete orbital cycle. Specifically, we examined data from March 30 to April 13, 2019, encompassing 228 revolutions. This period allowed us to analyze XO differences, with the expectation that SSH variation between two epochs behaves as a random variable within this 15-day timeframe.

3.2.2 ICESat-2 time specific orbits

The ICESat-2 team provides real ground track data for each repeat cycle, including the reference ground track time tags and coordinates for specific date ranges, which are stored in KML files. These files are posted at a reduced resolution in order to manage the file size, with data points spaced approximately every 7 km. With the help of the real coordinates of ground tracks, the actual location of each XO can be determined.

3.3 Methodology

3.3.1 The nominal orbit

Each full revolution of the satellite contains two segments: an ascending arc going from the southernmost to the northernmost orbit location and a descending arc in which the satellite moves in the opposite direction. The nominal orbit is assumed to be a near-circular trajectory. Theoretically, due to the steadiness of the motion of the satellite and of the rotation of the Earth, the satellite orbit projected onto the Earth's surface produces a fixed and regular pattern of ground tracks and XO points. However, in reality, the precession phenomenon arises from the non-spherical nature of a rotating celestial body, resulting in a non-uniform gravitational field and the presence of an equatorial bulge (Brown, 2002). As a consequence, the gravitational force acting on a satellite is not directed towards the center of the celestial body, but rather offset towards its equator. In the case of a typical prograde orbit around the Earth, the longitude of the ascending node undergoes a westward precession, while a retrograde orbit exhibits the opposite behavior. Therefore, the concept of a nominal orbit is normally employed for the approximate prediction of ground track positions.

Figure 3.1 shows the nominal orbit configuration (the subscript "i" refers to the inertial frame). The inclination I and the radius r are constant. φ is the latitude of the satellite in the Earth-fixed frame, and u is the argument of latitude. According to the geometry of the nominal orbit configuration, the relationship between φ and u follows the equation: $\sin\varphi = \sin I \sin u$. One ascending ground track crosses the equator forming an intersection, which is known as an ascending node. The longitude of the ascending node is Λ in the Earth-fixed frame, and the right ascension of the ascending node is Ω in the inertial frame. The inertial frame can be distinguished from the Earth-fixed frame through a rotation around the shared Z-axis. This rotation occurs by the hour angle of the Greenwich meridian, denoted as the Greenwich sidereal time θ.

For instance, when the satellite passes over the ascending node, the longitude of the ascending node is labeled λ_1. After one orbital period (T_{sat}), the nadir trace of the satellite crosses the equator a second time in the ascending direction. The longitude of this second intersection is labeled λ_2. Without the Earth's rotation, the two equatorial crossings would occur over the same site, i.e. $\lambda_1 = \lambda_2$. Since the Earth's rotation and nodal precession cannot be neglected, the longitude difference between the two ascending nodes is determined by

$$\Delta\lambda = \lambda_2 - \lambda_1 = \dot{\Lambda} T_{\mathrm{sat}}, \tag{3.1}$$

in which $\dot{\Lambda} = \dot{\Omega} - \dot{\theta}$ is the nodal precession rate in the Earth-fixed frame. The term $\dot{\theta}$ represents the Earth's rotation rate in the inertial frame and $\dot{\Omega}$ represents the nodal precession in the Earth-fixed frame.

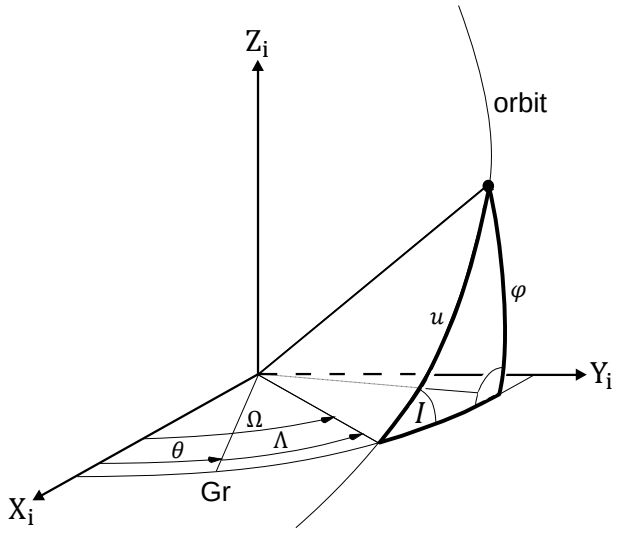

Figure 3.1: The nominal orbit in the inertial frame.

A repeat orbit is defined as an orbit, whose terrestrial ground-track pattern repeats after β revolutions and α nodal days, i.e. $\alpha = 91$ and $\beta = 1387$ for ICESat-2. A nominal orbit will be a repeat orbit if the orbital frequency $\dot{u}$ and $\dot{\Lambda}$ meet the following equation:

$$\frac{\dot{u}}{\dot{\Lambda}} = -\frac{\beta}{\alpha}. \tag{3.2}$$

The negative sign is used here because the value $\dot{\Lambda}$ will be negative for orbits lower than geosynchronous.

A nominal orbit is defined as (Cui and Lelgemann, 1993):

$$\begin{aligned} \Lambda(t) &= \Lambda_0 + \dot{\Lambda}t, \\ u(t) &= u_0 + \dot{u}t. \end{aligned} \tag{3.3}$$

If t_0 is the time tag when the satellite crosses the equator in the ascending direction, then $u_0 = 0$. The longitude of the crossing $\Lambda_0 = \lambda_0$. The travel time $t = \frac{u}{\dot{u}}$. These values are inserted into Eq. (3.3), yielding:

$$\Lambda = \Lambda_0 + \frac{\dot{\Lambda}}{\dot{u}}u = \lambda_0 - \frac{\alpha}{\beta}u. \tag{3.4}$$

3.3.2 Determination of crossover locations

Since the actual coordinates of the ground tracks are given as outlined in Section 3.2.2, the locations of XOs will be simply determined by intersecting ascending arcs with descending arcs, which means the locations of the intersections are the precise positions of XOs. There are 20 380 XOs in the Arctic region formed by 228 ground tracks as mentioned in 3.2.1, shown in Figure 3.2(b). Theoretically, all the XOs are arranged along latitude circles. In any given area, neighboring XO points create a diamond-shaped region, bounded by two ascending and two descending arcs. XO points at any latitude circle are equidistant. Equiangular: $\Delta\lambda = 2\pi/\beta$, see Figure 3.2(a). Near the Arctic Circle, the locations of nominal XOs predicted from the nominal orbit have a RMS of ~0.1° to real XOs in the across-track direction, which is equivalent to approximately 10 km. In reality, measurements of some XOs are missing due to the fact that they are located on land or data gaps are caused by atmospheric or instrumental reasons. Therefore, the XOs over the land should be eliminated.

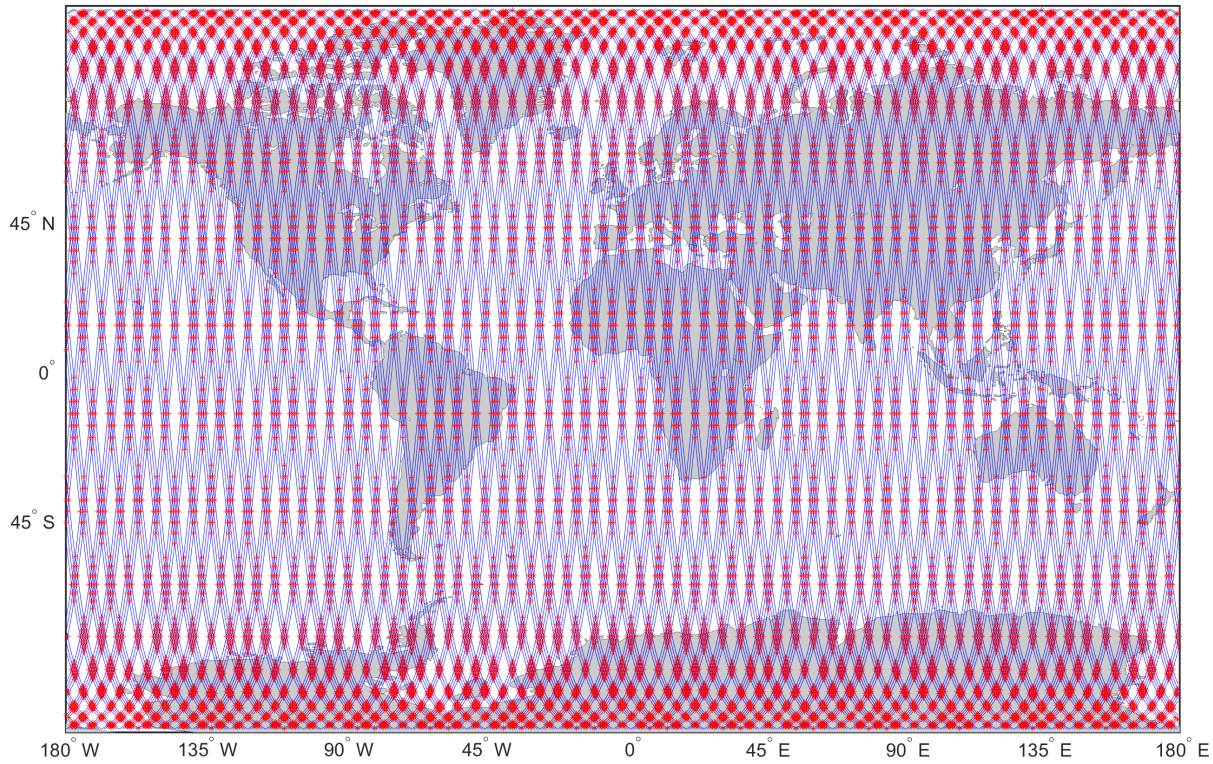

(a) Global distribution

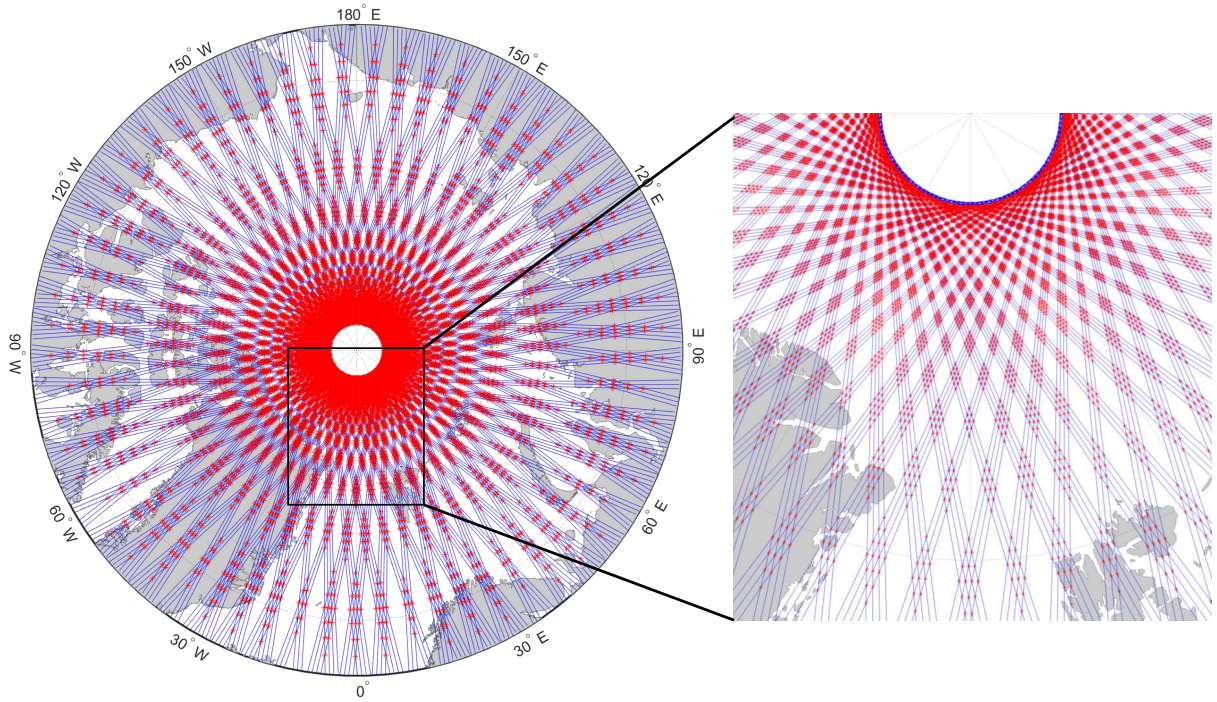

(b) Pan-Arctic distribution

Figure 3.2: Locations of Ground Tracks (blue) and XOs (red)

3.3.3 Crossover differences

The XO difference can be derived from h_{a} of the ascending track and h_{d} of the descending track at the XO location, which forms the following equation:

$$\Delta h_{\mathrm{ad}} = \Delta r_{\mathrm{a}} - \Delta r_{\mathrm{d}} + \Delta \zeta_{\mathrm{ad}} + \varepsilon, \tag{3.5}$$

in which Δr_{a} and Δr_{d} are the radial orbit errors of the ascending and descending arc segments, $\Delta \zeta_{\mathrm{ad}}$ is the sea surface variation between epochs t_{a} and t_{d}, and ε as the altimetric measurement error (the subscript "a" refers to ascending, the subscript "d" refers to descending). Here, $\Delta \zeta_{\mathrm{ad}}$ and ε are considered to be stochastic, i.e. in the XO adjustment the sum of $\Delta \zeta_{\mathrm{ad}} + \varepsilon$ is considered to be a single variable e, with $\mathrm{E}\{e\} = 0$, see Wunsch and Zlotnicki (1984).

To obtain the XO difference, it is necessary to calculate the SSHs accurately. The SSHs have a high sampling frequency (~100 Hz) in the ice-ocean, which corresponds to approximately 70 m along the track (as described in Section 2.4.2). We select the SSHs of each arc segment within 1 km of each XO, and we obtain the average value of the measurements after rejecting outliers by the method of median absolute deviation (MAD). Specifically, SSHs exceeding 2 times MAD are considered outliers, and the MAD is defined as:

$$\mathrm{MAD} = \mathrm{median}\left(\left|h_i - \tilde{h}\right|\right), \tag{3.6}$$

with h_i the SSHs derived from ATL12 measurements and $\tilde{h}$ the median of the SSHs. Upon eliminating the outliers, the resulting averaged value of the remaining SSHs will represent the SSH from a single arc segment at the XO.

Figure 3.3(a) shows the height difference of each XO. Some XOs with extremely large differences are distributed almost at all latitude circles. The large differences at lower latitudes are mostly caused by the ice-sea-land boundaries and the floating ice. At higher latitudes they are mostly caused by the time-variability of sea ice freeboard. The XO difference is nearly normally distributed, cf. Figure 3.3(b), with a mean difference of 0 and a RMS of 17.2 cm.

3.3.4 Crossover adjustment

The average altitude of the ICESat-2 satellite orbit is approximately 500 km, i.e. the orbit of the satellite is almost circular; thus, at least for local arc segments it can be

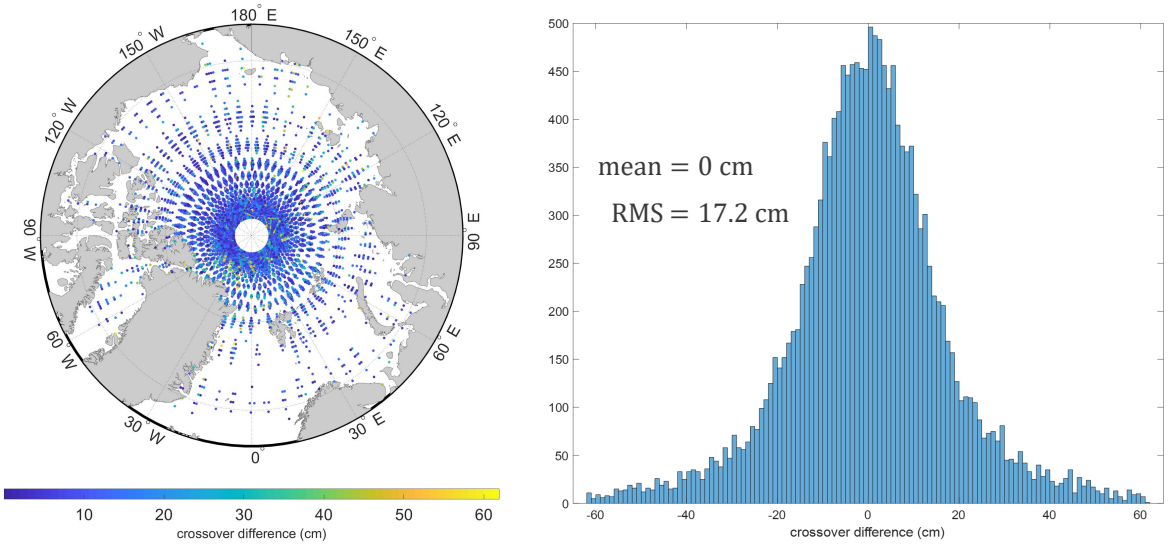

(a) Spatial distribution of XOs

(b) Histogram of XO difference

Figure 3.3: Distribution of XO difference.

described as a Kepler orbit. Its geometric radial distance is then

$$r = a\,(1 - e\cos E)\,, \tag{3.7}$$

with a the semi-major axis, e the eccentricity (nearly circular orbit, i.e. $e \approx 0$), and E the eccentric anomaly. Eq. (3.7) is linearized by

$$\begin{aligned} \Delta r &= \frac{\partial r}{\partial a}\Delta a + \frac{\partial r}{\partial e}\Delta e + \frac{\partial r}{\partial E}\Delta E \\ &= \Delta a + a\Delta M e\sin M - \Delta e a\cos M. \end{aligned} \tag{3.8}$$

where we assume the mean anomaly $M = E$, with $M = M_0 + \dot{M}t$ and $\dot{M} = n = \frac{2\pi}{T}$ (n = mean motion, T = orbit period). Δr describes the function of the radial orbit error. The perturbations Δa, ΔM, and Δe can be considered as constants of the arc segment. For relatively short arc segments (< 2000 km), $\cos M$ is near-constant and $\sin M \approx M$. Thus, the function model for the radial orbit error can be simplified into:

$$\Delta r = b + q \cdot \mu, \qquad \text{[relatively short arcs]}, \tag{3.9}$$

in which b and q are 2 parameters of the model. μ represents a portion of the time interval between the XO and the reference point, relative to the entire arc time interval.

A conventional method for defining a local area is to define a latitude-longitude bounding box, which can be seen in Figure 3.4(a). The disadvantage of this area definition is

that the length of arc segments in the corners is shorter than those in the center. This will cause the problem that different lengths of arc segments are not compatible with each other when the same adjustment function model is used. To solve this problem, observations of short arc segments can be down-weighted. However, the satellite travels arc segments of equal length, resulting in approximately the same travel time. For this reason, we define the local area as a diamond-shaped region bounded by two parallel ascending and two descending arc segments (Schrama, 1989), which can be seen in Figure 3.4(b). For a regional area, like Figure 3.5, a diamond-shaped region is bounded by ascending arcs 1 and 3, and descending arc segments 4 and 6. The reference time t_0 is selected such that μ is 0 when one track enters the area (the intersection on the boundary of the diamond shape). Ascending arc segments form intersections firstly with arc segment 4 and secondly with arc segment 5. The intersection time t_{35} from ascending arc segment 3 at XO F is transformed to a quantity μ_{35} by $\mu_{35} = (t_{35} - t_{34})/(t_{36} - t_{34})$. Analogously to μ_{35}, the parameter μ_{53} is defined where arc segment 5 intersects 3, accordingly $\mu_{53} = (t_{53} - t_{53})/(t_{51} - t_{53})$. Given that all arc segments are of approximately equal length in a diamond-shaped area, it is reasonable to assume that the time interval between consecutive XOs is also uniform.

The XO difference formed by the arc segment j and i results in:

$$\Delta h_{ij} = \Delta r_i \left(\mu_{ij}\right) - \Delta r_j \left(\mu_{ji}\right). \tag{3.10}$$

For linear function Δr_i and Δr_j we find:

$$\Delta h_{ij} = \left(b_i + q_i \mu_{ij}\right) - \left(b_j + q_j \mu_{ji}\right). \tag{3.11}$$

After these preparations, the linear model can be written as

$$y = Ax + e, \tag{3.12}$$

where e is the residual matrix with the assumption $\mathrm{E}\{e\} = 0$ and $\mathrm{D}\{e\} = \sigma_0^2 I$; here I is the unit matrix. x is the parameter vector. The corresponding structure of the design matrix A becomes:

$$A = \left[\begin{array}{cccccc|cccccc}
1 & \mu_{14} & & & & & -1 & -\mu_{41} & & & & \\
1 & \mu_{15} & & & & & & & -1 & -\mu_{51} & & \\
1 & \mu_{16} & & & & & & & & & -1 & -\mu_{61} \\
 & & 1 & \mu_{24} & & & -1 & -\mu_{42} & & & & \\
 & & 1 & \mu_{25} & & & & & -1 & -\mu_{52} & & \\
 & & 1 & \mu_{26} & & & & & & & -1 & -\mu_{62} \\
 & & & & 1 & \mu_{34} & -1 & -\mu_{43} & & & & \\
 & & & & 1 & \mu_{35} & & & -1 & -\mu_{53} & & \\
 & & & & 1 & \mu_{36} & & & & & -1 & -\mu_{63}
\end{array}\right]. \tag{3.13}$$

The normal equations are $A^{\mathrm{T}}Ax = A^{\mathrm{T}}y$. Then the estimated parameters of the linear model can be calculated by $\hat{x} = (A^{\mathrm{T}}A)^{-1}A^{\mathrm{T}}y$.

One problem of XO adjustment is the existence of singular solutions, which belong to a so-called null space of the normal equations. The situation is comparable to that of a leveling network. Networks of height difference observations are derived by the differential leveling. A closed leveling network is a loop that begins and ends at one point, with the measurements of height differences, but not absolute heights. Theoretically, the misclosure should be zero, but in fact random errors cannot be avoided, which can be subjected to a LS adjustment. There will be a datum problem when adjusting the errors. When the height of one arbitrary point is fixed as a constant, the datum for the entire leveling network becomes fixed, allowing for the estimation of heights for other points. The same holds true here; therefore, we fix parameters falling inside the null space of the XO minimization problem. In the case of the 2-parameter model (number of parameters $p = 2$), the rank defect of matrix A is 4. The datum problem can be solved by fixing p parameters of p non-intersecting arcs. This means, for the 2-parameter model two arbitrary parallel arcs (ascending or descending) must be fixed.

For the whole Arctic area, similar to the local XO adjustment, the function model for the radial orbit error (see Figure 3.6) is preferably written from Eq. (3.8) as follows:

$$\Delta r = x_0 + x_1 \sin u + x_2 \cos u, \qquad \text{[long arcs]} \tag{3.14}$$

with the argument of latitude $u = \frac{2\pi}{T}(t - t_0) = \dot{u}\Delta t$, and $\dot{u}$ the angular velocity. The starting time t_0 is the time tag at the equator of each arc segment and Δt is the time interval between a XO and the equator along the arc segment. Since the relationship between φ and u follows $\sin\varphi = \sin I \sin u$, u can be calculated when the XO location is determined. Unlike the local XO adjustment, where two parameters represent a single

arc, for the Arctic XO adjustment, three parameters (x_0, x_1 and x_2) represent each arc segment.

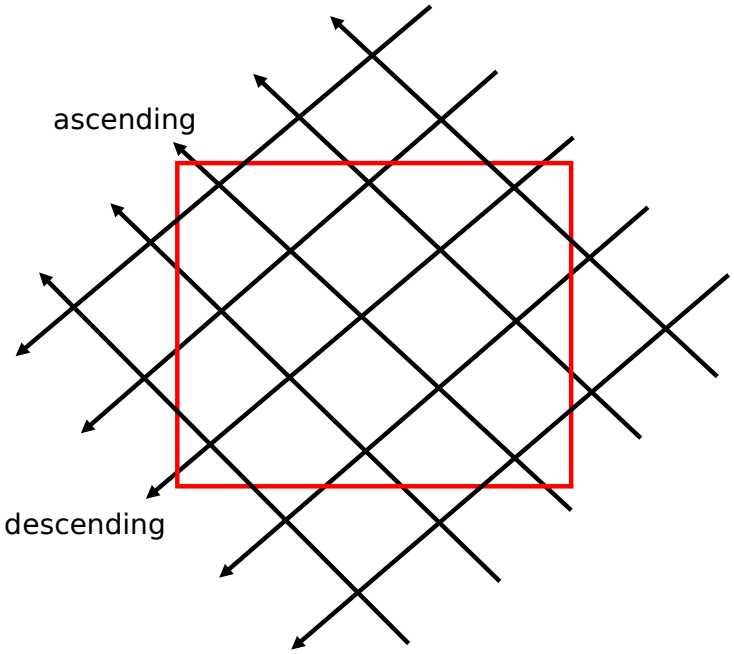

(a) Local area bounded by latitude and longitude

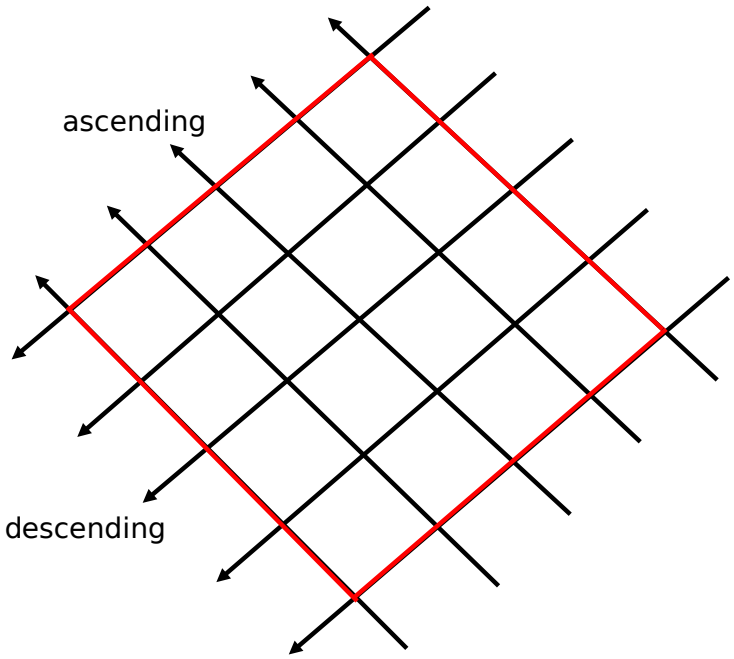

(b) Local area bounded by arc segments

Figure 3.4: Ground tracks in a local area.

For the first strategy mentioned in Section 3.1, the relative time tag Δt_a equals $\frac{T}{2} - \Delta t_\mathrm{d}$ at one XO, i.e. $u_\mathrm{d} = \pi - u_\mathrm{a}$. For instance, the XO of arc 3 and arc 4 locates on the

ascending part of arc 3 and the descending part of arc 4. Accordingly, the variable u at the XO for arc 3 is u_{a}, which is denoted as u_{34}, and for arc 4 the variable u is u_{d}, which is denoted as u_{43}. The value of the relative time tag Δt only depends on the latitude φ, which means all XOs at the same latitude have the same $|\Delta t|$. Therefore, the coefficients of the parameters in the linearized model can be determined by the latitudes of XOs.

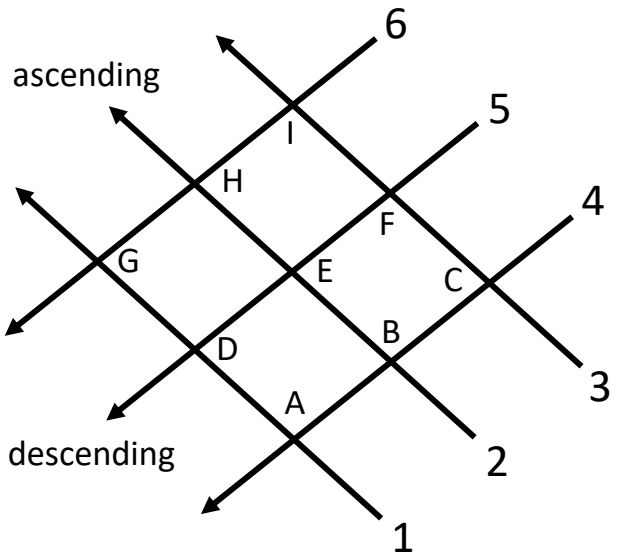

Figure 3.5: Local XO scheme.

The XO difference formed by the arc segment j and i results in:

$$\Delta h_{ij} = (x_{0i} + x_{1i} \sin u_{ij} + x_{2i} \cos u_{ij}) - (x_{0j} + x_{1j} \sin u_{ji} + x_{2j} \cos u_{ji}). \tag{3.15}$$

The vector of observations y contains all XO differences (n XOs) with l revolutions, which forms the coefficient matrix:

$$\underset{n\times m}{A} = \begin{bmatrix} A_{\mathrm{a}} \\ {\scriptstyle n\times 3l} \end{bmatrix} - \begin{bmatrix} A_{\mathrm{d}} \\ {\scriptstyle n\times 3l} \end{bmatrix}. \tag{3.16}$$

According to the arc segments distributed in Figure 3.6, the structure of the coefficient matrix A becomes to Eq. (3.17), as follows:

$$
A = \left[\begin{array}{cccccc|cccccc|cccccc|c}
1 & \sin u_{12} & \cos u_{12} & -1 & -\sin u_{21} & -\cos u_{21} & 0 & 0 & 0 & 0 & 0 & 0 & 0 & 0 & 0 & 0 & 0 & \cdots \\
-1 & -\sin u_{13} & -\cos u_{13} & 0 & 0 & 0 & 1 & \sin u_{31} & \cos u_{31} & 0 & 0 & 0 & 0 & 0 & 0 & 0 & 0 & \cdots \\
1 & \sin u_{14} & \cos u_{14} & 0 & 0 & 0 & 0 & 0 & 0 & -1 & -\sin u_{41} & -\cos u_{41} & 0 & 0 & 0 & 0 & 0 & \cdots \\
-1 & -\sin u_{15} & -\cos u_{15} & 0 & 0 & 0 & 0 & 0 & 0 & 0 & 0 & 0 & 1 & \sin u_{51} & \cos u_{51} & 0 & 0 & \cdots \\
0 & 0 & 0 & 1 & \sin u_{23} & \cos u_{23} & -1 & -\sin u_{32} & -\cos u_{32} & 0 & 0 & 0 & 0 & 0 & 0 & 0 & 0 & \cdots \\
0 & 0 & 0 & -1 & -\sin u_{24} & -\cos u_{24} & 0 & 0 & 0 & 1 & \sin u_{42} & \cos u_{42} & 0 & 0 & 0 & 0 & 0 & \cdots \\
0 & 0 & 0 & 1 & \sin u_{25} & \cos u_{25} & 0 & 0 & 0 & 0 & 0 & 0 & -1 & -\sin u_{52} & -\cos u_{52} & 0 & 0 & \cdots \\
0 & 0 & 0 & 0 & 0 & 0 & 1 & \sin u_{34} & \cos u_{34} & -1 & -\sin u_{43} & -\cos u_{43} & 0 & 0 & 0 & 0 & 0 & \cdots \\
0 & 0 & 0 & 0 & 0 & 0 & -1 & -\sin u_{35} & -\cos u_{35} & 0 & 0 & 0 & 1 & \sin u_{53} & \cos u_{53} & 0 & 0 & \cdots \\
0 & 0 & 0 & 0 & 0 & 0 & 0 & 0 & 0 & 1 & \sin u_{45} & \cos u_{45} & -1 & -\sin u_{54} & -\cos u_{54} & 0 & 0 & \cdots \\
\vdots & \vdots & \vdots & \vdots & \vdots & \vdots & \vdots & \vdots & \vdots & \vdots & \vdots & \vdots & \vdots & \vdots & \vdots & \vdots & \vdots & \ddots
\end{array}\right],
\tag{3.17}
$$

and the parameter vector x becomes to Eq. (3.18):

$$x = [x_{01}\ x_{11}\ x_{21}\ x_{02}\ x_{12}\ x_{22}\ x_{03}\ x_{13}\ x_{23}\ x_{04}\ x_{14}\ x_{24}\ x_{05}\ x_{15}\ x_{25}\ \cdots]^{\mathrm{T}}. \tag{3.18}$$

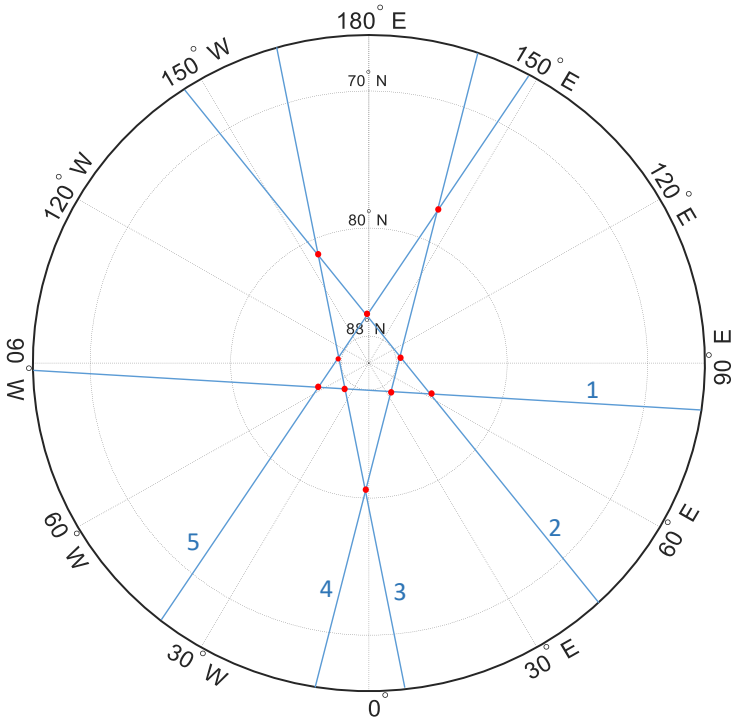

Figure 3.6: Pan-Arctic XO scheme: blue lines are ground tracks and red points are XOs.

For the LS adjustment, a necessary condition $n > m = 3l$ should be fulfilled in order to over-determine the parameters (vector of x has the dimension of $m \times 1$). The rank$(A) = r < m$, which leads to the singularity of the XO adjustment. Theoretically, adding the parameters of the fixed arcs to the linear system constraints will not affect the adjusted XO differences, with the equation:

$$\underset{d\times m}{D^{\mathrm{T}}}\ \underset{m\times 1}{x} = c. \tag{3.19}$$

The sinusoidal representation in a least-squares problem coupled with the constraint constitutes the constrained sinusoidal XO adjustment. In order to remove the rank deficiency of matrix A, matrix D must be under the condition of Eq. (3.20):

$$\text{rank}\left(\left[\underset{m\times n}{A^{\mathrm{T}}} \middle| \underset{m\times d}{D}\right]\right) = m. \tag{3.20}$$

Then we solve the least-squares problem by minimizing the constrained Lagrangian (Golub and Van Loan, 2013):

$$\begin{aligned}
\mathcal{L}_D(x,\lambda) &= \frac{1}{2}e^{\mathrm{T}}e + \lambda\left(D^{\mathrm{T}}x - c\right) \\
&= \frac{1}{2}y^{\mathrm{T}}y - y^{\mathrm{T}}Ax + \frac{1}{2}x^{\mathrm{T}}A^{\mathrm{T}}Ax + \lambda\left(D^{\mathrm{T}}x - c\right) \\
\frac{\partial \mathcal{L}_D}{\partial x} &= -A^{\mathrm{T}}y + A^{\mathrm{T}}Ax + D\lambda = 0 \\
\frac{\partial \mathcal{L}_D}{\partial \mathcal{L}} &= D^{\mathrm{T}}x - c \\
&\Rightarrow \underset{(m+d)\times(m+d)}{\begin{pmatrix} A^{\mathrm{T}}A & D \\ D^{\mathrm{T}} & 0 \end{pmatrix}} \underset{(m+d)\times 1}{\begin{pmatrix} \hat{x} \\ \hat{\lambda} \end{pmatrix}} = \begin{pmatrix} A^{\mathrm{T}}y \\ c \end{pmatrix} \\
\Rightarrow \hat{x} = N^{-1}\langle A^{\mathrm{T}}y + Dc - &\left\{D(D^{\mathrm{T}}N^{-1}D)^{-1}\left[D^{\mathrm{T}}N^{-1}A^{\mathrm{T}}y + (D^{\mathrm{T}}N^{-1}D - I)c\right]\right\}\rangle \\
N &:= A^{\mathrm{T}}A + DD^{\mathrm{T}}.
\end{aligned} \tag{3.21}$$

Then the adjusted XO differences $\hat{y} = A\hat{x}$.

For the second strategy mentioned in Section 3.1, an arc segment is defined as the ascending or descending part of the ground track. When we use this strategy, that means 3 parameters represent an ascending or descending arc segment separately, instead of representing one full revolution. The number of parameters will be doubled. Since the starting time t_0 is the time tag at the equator of each arc segment and Δt is the time interval passing through the equator to the XO location. Therefore, the relative time tag Δt_{a} from ascending equals $-\Delta t_{\mathrm{d}}$ from descending at one XO, i.e. $u_{\mathrm{d}} = -u_{\mathrm{a}}$. The vector of observations y contains all XO differences (n XOs) with l ascending and l descending arc segments, which will change the format of A matrix to:

$$\underset{n\times m}{A} = \left[\underset{n\times 3l}{A_{\mathrm{a}}} \middle| \underset{n\times 3l}{0}\right] - \left[\underset{n\times 3l}{0} \middle| \underset{n\times 3l}{A_{\mathrm{d}}}\right]. \tag{3.22}$$

Then the structure of the coefficient matrix A becomes to Eq. (3.23), as follows:

$$
A = \begin{bmatrix}
1 & \sin u_{12} & \cos u_{12} & & & & & & & & & & & & \\
1 & \sin u_{14} & \cos u_{14} & & & & & & & & & & & & \\
 & & & 1 & \sin u_{23} & \cos u_{23} & & & & & & & & & \\
 & & & 1 & \sin u_{25} & \cos u_{25} & & & & & & & & & \\
 & & & & & & 1 & \sin u_{31} & \cos u_{31} & & & & & & \\
 & & & & & & 1 & \sin u_{34} & \cos u_{34} & & & & & & \\
 & & & & & & & & & 1 & \sin u_{42} & \cos u_{42} & & & \\
 & & & & & & & & & 1 & \sin u_{45} & \cos u_{45} & & & \\
 & & & & & & & & & & & & 1 & \sin u_{51} & \cos u_{51} \\
 & & & & & & & & & & & & 1 & \sin u_{53} & \cos u_{53}
\end{bmatrix}
- \begin{bmatrix}
 & & & & & & & & & & & & & & \\
 & & & & & & & & & & & & & & \\
 & & & & & & & & & & & & & & \\
 & & & & & & & & & & & & & & \\
 & & & & & & & & & & & & & & \\
 & & & & & & & & & & & & & & \\
 & & & & & & & & & & & & & & \\
 & & & & & & & & & & & & & & \\
 & & & & & & & & & & & & & & \\
 & & & & & & & & & & & & & &
\end{bmatrix}_{10\times 15}
$$

$$
\begin{bmatrix}
 & & & & & & & & & & & & & & \\
 & & & & & & & & & & & & & & \\
 & & & & & & & & & & & & & & \\
 & & & & & & & & & & & & & & \\
 & & & & & & & & & & & & & & \\
 & & & & & & & & & & & & & & \\
 & & & & & & & & & & & & & & \\
 & & & & & & & & & & & & & & \\
 & & & & & & & & & & & & & & \\
 & & & & & & & & & & & & & &
\end{bmatrix}_{10\times 15}
\begin{bmatrix}
1 & \sin u_{21} & \cos u_{21} & & & & & & & & & & & & \\
 & & & 1 & \sin u_{32} & \cos u_{32} & & & & & & & & & \\
 & & & & & & 1 & \sin u_{41} & \cos u_{41} & & & & & & \\
 & & & & & & & & & 1 & \sin u_{52} & \cos u_{52} & & & \\
 & & & & & & & & & & & & 1 & \sin u_{43} & \cos u_{43} \\
1 & \sin u_{13} & \cos u_{13} & & & & & & & & & & & & \\
 & & & 1 & \sin u_{24} & \cos u_{24} & & & & & & & & & \\
 & & & & & & & & & 1 & \sin u_{54} & \cos u_{54} & & & \\
 & & & & & & 1 & \sin u_{35} & \cos u_{35} & & & & & & \\
1 & \sin u_{15} & \cos u_{15} & & & & & & & & & & & &
\end{bmatrix}, \tag{3.23}
$$

and the parameter vector x becomes to Eq. (3.24):

$$x = [(x_{01}\ x_{11}\ x_{21} \cdots x_{05}\ x_{15}\ x_{25})_{\mathrm{a}} \cdots (x_{01}\ x_{11}\ x_{21} \cdots x_{05}\ x_{15}\ x_{15})_{\mathrm{d}} \cdots]^{\mathrm{T}}. \tag{3.24}$$

To solve the least-squares problem, the process is identical to the first strategy using Eq. (3.20) and Eq. (3.21).

3.4 Results and discussion

For the first strategy, the histograms of XO differences before and after adjustment are demonstrated in Figure 3.7. The RMS is reduced from 17.2 cm to 8.7 cm using the method of the XO adjustment. Assuming the residual errors are independent in the XO difference function, 8.7 cm divided by $\sqrt{2}$ gives a value of 6.1 cm. That means the orbit error level of ICESat-2 in the Arctic region is generally 6.1 cm.

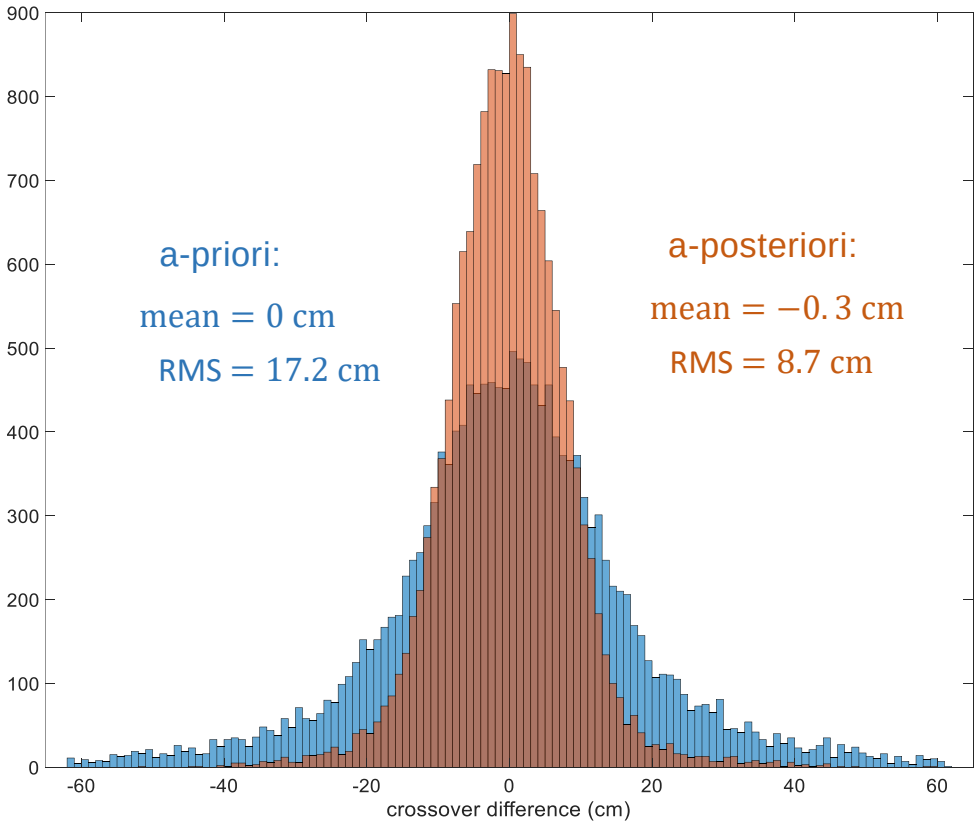

Figure 3.7: First strategy: a-priori/a-posteriori histogram of XO differences.

From Figure 3.8 we can see XO differences at different latitudes before and after adjustment. At the XOs closest to the North pole, the differences are reduced to about 6 cm to 7 cm. The reduced value of XO difference divided by $\sqrt{2}$ gives an approximate value of 4 cm to 5 cm. However, parts of the XO differences are not significantly reduced, which may be caused by the boundaries of sea-ice-land. For this reason, the altimetry will have large measurement errors influenced by these boundaries.

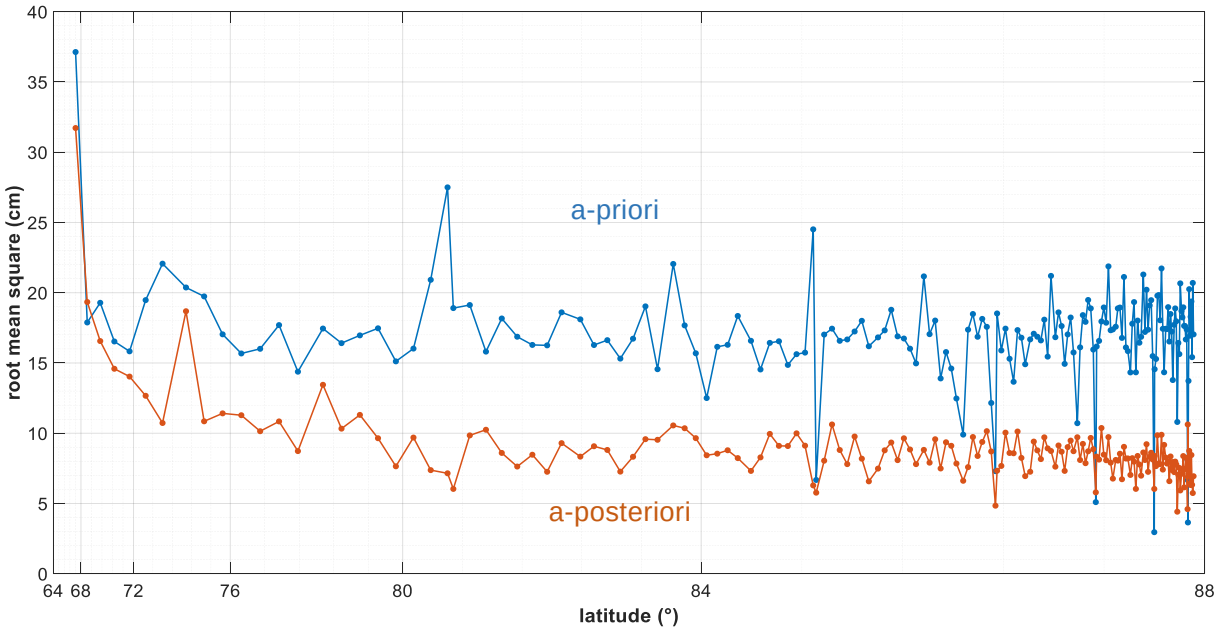

Figure 3.8: First strategy: comparison of XO differences at different latitudes before and after adjustment.

For the second strategy, the RMS XO differences is reduced from 17.2 cm to 11.8 cm, see Figure 3.9, and the XO differences at different latitudes before and after adjustment are shown in Figure 3.10. Then, 11.8 cm divided by $\sqrt{2}$ gives a value of 8.3 cm approximately. Compared to the results of the first strategy, residuals are not reduced that much.

For the first strategy, the rank deficiency $d = m - r = 2$ is caused by the dependency between the column vectors of the A matrix, which are the parameters of one arc. For the local XO adjustment, all parallel arcs are independent. However, for the Arctic XO adjustment, any one arc is dependent on others. This means only one arbitrary arc segment should be fixed. Since $\sin u_{\mathrm{a}} = \sin u_{\mathrm{d}}$ and $\cos u_{\mathrm{a}} = -\cos u_{\mathrm{d}}$, the XO difference $\Delta h_{\mathrm{ad}} = (x_{0\mathrm{a}} - x_{0\mathrm{d}}) + (x_{1\mathrm{a}} - x_{1\mathrm{d}}) \sin u + (x_{2\mathrm{a}} + x_{2\mathrm{d}}) \cos u$. For the 3-parameter model, XOs of the ascending part and the descending part are symmetric on one arc segment. Therefore, the parameter x_2 is linearly independent, i.e. two free variables x_0

and x_1 of one arbitrary arc should be fixed. For the second strategy, the rank deficiency $d = m - r = 3$. The reason is that any two ascending arcs or descending arcs are independent to each other, but ascending arcs and descending arcs are dependent. That means 3 free variables are from one arc. Therefore, to solve the problem of singularity, 3 parameters of any arbitrary arc segment should be fixed. In fact, when we use 3 parameters to represent an ascending or descending arc segment separately, there exists a problem of discontinuity at the highest latitude between two arc segments for one revolution. The average bias at the latitude of 88° is 18.3 cm. In addition to the discontinuity, there exists a problem of over-parameterization. The superfluous parameters tend to be poorly estimable, which should be avoided.

Although random residuals are adjusted using a proper function model, the error level is still on the order of 6 cm. Except for the radial orbit, the laser mispointing error also should be taken into account. Mispointing error refers to the deviation of the laser beam from its nominal pointing direction, which can affect the accuracy of the elevation measurements. The requirement for pointing stability after post-processing is about 6.5 m in the cross-track direction (Markus et al., 2017), which translates into an elevation error of several centimeters even over small surface slopes ($< 0.5°$).

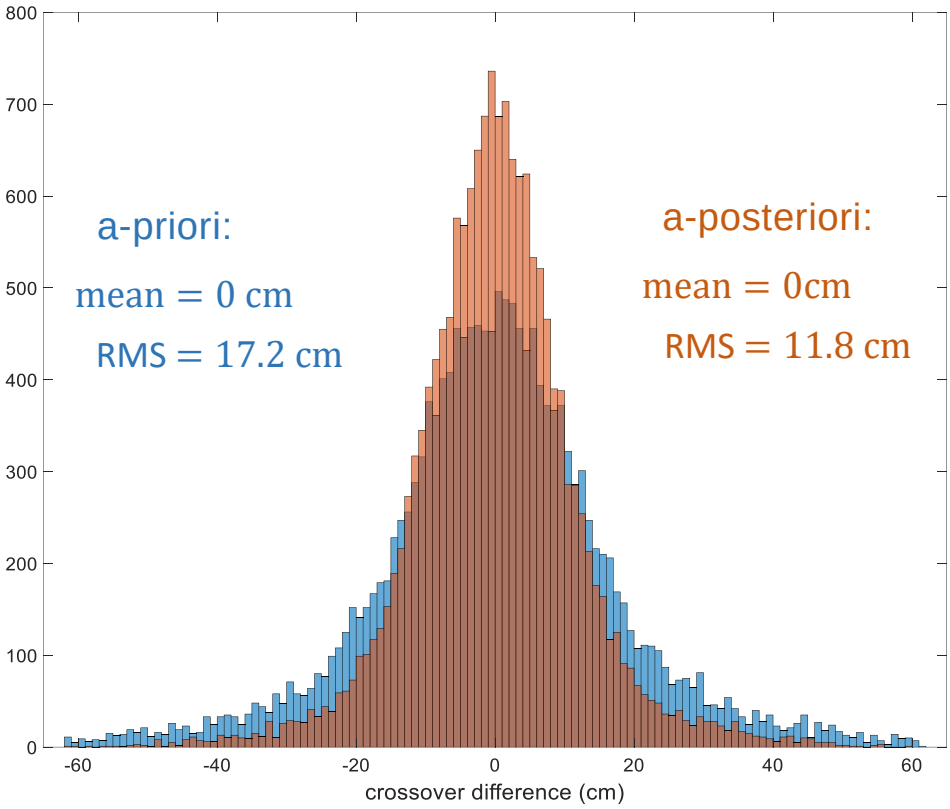

Figure 3.9: a-priori/a-posteriori histogram of XO differences.

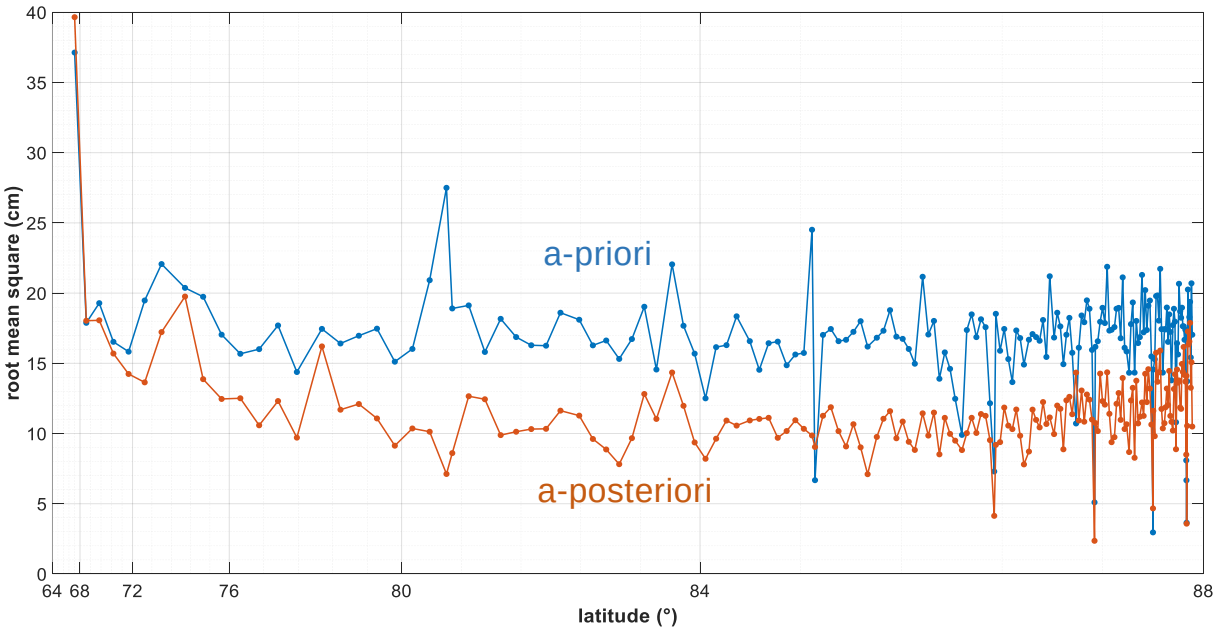

Figure 3.10: a-priori/a-posteriori XO differences at different latitudes.

3.5 Summary

In this chapter, we successfully quantified the radial orbit error level of ICESat-2 using LS adjustment. Depending on the size of the area the radial orbit error can be described by a 2 or 3-parameter model. For the local XO adjustment, 2 parameters represent an ascending or descending arc. It is recommended to define the area by two ascending and two descending arcs, like a diamond shape. For the Arctic region, 3 parameters represent one revolution arc. XO adjustment leads to a large reduction of the radial orbit error, with the RMS reduced from 17.2 cm to 8.7 cm. The linear system has a rank defect, but it depends on the chosen parameter model. For the diamond shape region, the linear system has a rank defect of p^2 (p is the number of parameters). It is eliminated by fixing the p parameters of p non-intersecting arc segments. For the Arctic region, the rank defect is 2, which means only one arc segment should be fixed. However, in a real XO adjustment with data gaps and interruptions due to islands and coastlines, the rank defect will be larger than the theoretical value, which can be considered as a null-space surface. However, to better understand the orbit error of ICESat-2, the mispointing error must be studied in further research.

Chapter 4

Monitoring lake level variation from ICESat-2 and Landsat data

4.1 Introduction

Conventionally, hydrologists have relied on lake water levels and in conjunction with a known bathymetric map to estimate the volume of a lake (Duan and Bastiaanssen, 2013). The acquisition of a bathymetric map for a lake is commonly accomplished through surveys conducted via shipborne sonar, echo-sounding equipment, and airborne LiDAR (Gao, 2009). The sound waves of shipborne sonar or echo-sounding travel through the water and reflect off the lake bottom. The time interval between the transmitted and received signal is measured, and with knowledge of the speed of sound through water, the depth of the lake at the point of reflection can be determined (Odhiambo and Boss, 2004). The airborne laser light can penetrate through water content relatively deep (up to tens of meters depending on the water clarity) (Hilldale and Raff, 2008). Nevertheless, the employment of these bathymetric methods is often hindered by their high cost and technical complexity, rendering them impractical for implementation in remote and politically sensitive regions (Peng et al., 2006), thereby imposing limitations on their application on a global scale.

In recent years, satellite-based remote sensing techniques have emerged as an essential tool for monitoring the volume variation of lakes. Satellites can provide frequent and spatially extensive data, as well as reduce costs and logistical challenges associated with traditional field-based measurements (Muller-Karger et al., 2018). One of the popular approaches relies on the estimation of water areas from satellite imagery to establish an empirical equation in order to infer water volume (Cai et al., 2016). However, water volumes from gauge stations are needed for the retrieval of the constant parameters in the empirical equations between water volume and water area. Other methodologies involve the utilization of the water level measurements from satellite altimetry

combined with water areas to estimate their volume, through the implementation of a particular water level-area relationship specific to a given water body (Crétaux et al., 2016, 2011; Elmi and Tourian, 2023; Zhang et al., 2017). Although the use of satellite radar altimetry and imagery enables remote estimation of water levels and volumes, it remains challenging to ensure the accuracy of empirical equation parameters due to the difficulty of acquiring corresponding data simultaneously. Additionally, radar altimetry may not be suitable for small lakes and reservoirs due to the limitations of large footprints (i.e. hundreds of meters to several kilometers in diameter) in obtaining water levels and spatial-temporal resolutions of satellite altimetry.

An alternative method called satellite-based bathymetry (SDB) has been increasingly recognized for acquiring high-resolution and large-scale bathymetric data in a cost-effective manner (Cahalane et al., 2019). By analyzing the differences in reflection of the electromagnetic spectrum, it is possible to estimate the depth of the water. However, the accuracy of SDB can be affected by the angle of the sun and the depth of the water being measured, and the depth estimated by SDB depends on the turbidity of the water. Zhang et al. (2021) used the digital elevation model (DEM) from SRTM and Landsat imagery to estimate changes in lake level and volume on the Tibetan Plateau. However, since the SRTM data were only collected once and the radar signal cannot penetrate the water surface, the bathymetric information below the water level at the SRTM acquisition time cannot be obtained. Despite the fact that remotely sensed data has been used to obtain empirical equations for estimating water volumes based only on water level measurements, it is worth noting that satellite altimeters were not capable of providing inland water level data until 1992. The launch of the Topex/Poseidon satellite in 1992 provided an opportunity to monitor inland hydrological cycles (Calmant and Seyler, 2006). As a consequence of the limitations in satellite altimetry technology prior to 1992, current methodologies relying solely on remote sensing data cannot accurately calculate water levels and volumes before 1992.

Since the launch of ICESat-2 laser altimetry, the situation has changed. The high-density ground tracks consisting of 1387 tracks with six beams and an operational off-nadir pointing technique over land areas are capable of covering a vast majority of the Earth's lakes and reservoirs. The quantitative results demonstrate that the RMS water level measurements obtained from ICESat-2 and gauge stations exhibit a margin of error within 5 cm (Zhang et al., 2022), indicating the provision of highly accurate water level data. The small laser footprint (~17 m in diameter) enables the observation of water levels in small lakes. Furthermore, the ICESat-2 altimeters employ 532 nm

green lasers that possess the ability to penetrate the water column, and research has revealed that it can capture up to 22 m of underwater topography, depending on the clarity of water (Ranndal et al., 2021). Thus, the bathymetric map of lakes can be generated in clear water situations, at least for the near-shore regions (Ryan et al., 2020).

In cases where water level data cannot be obtained from satellite altimetry, the water level can still be estimated by matching the lake boundary and topographic bathymetric profiles, if the lake boundary is available at one epoch. The Landsat imagery data have been available since 1972, enabling the extraction of lake boundaries from these images combined with DEM-like lake profiles, thereby facilitating the estimation of water level, area and volume from that time onwards. Water levels can be obtained using laser tracks of just a few days, without being limited by the temporal span of the altimetry data. In this chapter, a novel approach is proposed to estimate the variation of water level and volume time series using ICESat-2 laser data and Landsat imagery, from 1984 to 2021. This study investigated the capabilities of ICESat-2 and satellite imagery to monitor lake level-area-volume variations and compared the results with *in-situ* measurements. This method only relies on remotely sensed data, which can be applied to remote and wild lakes without *in-situ* stations at regional and global scales. The availability of these data has opened up new opportunities for understanding and managing lake resources, and can help to inform decision-making in water resources management, hydrology, and ecology.

4.2 Methodology

ICESat-2 provides the ability to measure the water level directly. However, water level measurements by ICESat-2 are only possible during the satellite's passage over the lake. Consequently, in this study, estimating water levels depends on the methods for obtaining accurate lake boundaries and nearshore profiles. Lake boundaries can be extracted from Landsat images, and lake nearshore profiles can be extracted from raw ICESat-2 data. When the lake boundary intersects with the nearshore profile, the two datasets effectively form a virtual gauge station, with the elevation of this intersection serving as the estimated water level, see Figure 4.1. The lake volume variations will be estimated after generating the water level and area time series. Consequently, the methods to accomplish this objective will be introduced in the following subsections.

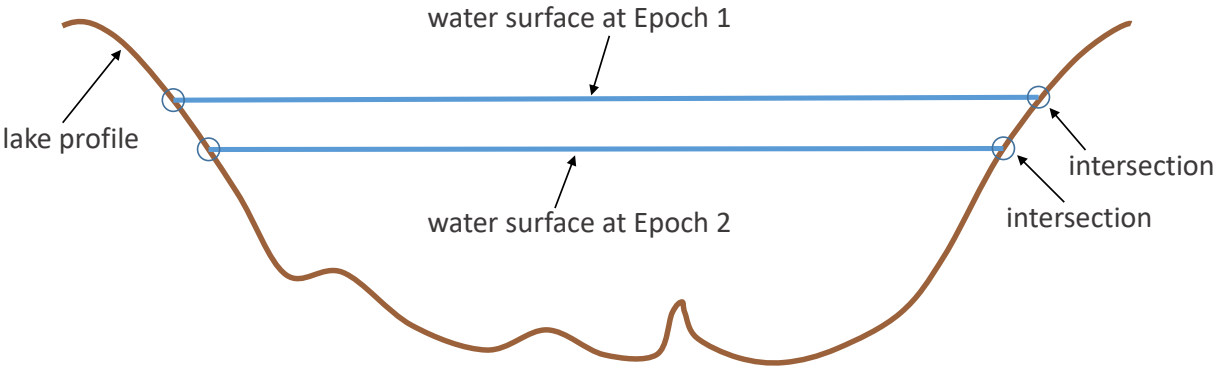

Figure 4.1: Schematic diagram of intersections of lake boundaries and topographic bathymetric profile.

4.2.1 Water mask extraction

Land-water classification is the basic step for lake extent from the imagery. The Normalized Difference Water Index (NDWI) was brought up by Gao (1996), which uses Near-Infrared (NIR) and Short-Wave Infrared (SWIR) bands to detect water. The formula for NDWI is:

$$\mathrm{NDWI} = \frac{\mathrm{NIR} - \mathrm{SWIR}}{\mathrm{NIR} + \mathrm{SWIR}}. \tag{4.1}$$

Water absorbs more SWIR radiation than NIR radiation compared to other land covers such as vegetation and soil. By taking the difference of these two spectral bands, NDWI enhances the contrast between water and other features. The resulting index values range from -1 to 1, where higher values indicate a higher likelihood of the presence of water in the corresponding pixels.

The Modified Normalized Difference Water Index (MNDWI) developed by Xu (2006) is the enhanced version of NDWI for classifying water bodies. The formula for MNDWI is:

$$\mathrm{MNDWI} = \frac{\mathrm{Green} - \mathrm{SWIR}}{\mathrm{Green} + \mathrm{SWIR}}. \tag{4.2}$$

MNDWI is often considered better at detecting water than NDWI in certain situations because it uses the Green band (which is sensitive to vegetation) instead of the NIR band used in NDWI. This makes MNDWI less sensitive to vegetation and more sensitive to water. In areas with a lot of vegetation, NDWI can sometimes have false positives, detecting vegetation as water. In contrast, MNDWI tends to produce fewer false positives in vegetated areas because the Green band helps to distinguish between vegetation and water.

The radiometric measure of each pixel is obtained after calculating MNDWI. The determination of the intensity threshold is a critical factor that can significantly influence the accuracy of water extent classification. The threshold for MNDWI can be determined by using various methods such as visual inspection, statistical analysis, or machine learning algorithms (Yang et al., 2018). One common method is to use Otsu's thresholding algorithm (Otsu, 1979), which is an automatic method to determine the threshold based on the histogram of the MNDWI image. Otsu's method is a variance-based algorithm that determines the threshold value by minimizing the weighted variance between the foreground and background pixels. In this method, the histogram of the MNDWI image is first generated, and then the threshold value that minimizes the intra-class variance is selected. The intra-class variance is a measure of the similarity of pixels within the same class, and minimizing this value ensures that the threshold separates the water pixels from non-water pixels as accurately as possible.

The formula for finding the intra-class variance at any threshold t is given by:

$$\sigma^2(t) = \omega_{\mathrm{b}}(t)\sigma^2_{\mathrm{b}}(t) + \omega_{\mathrm{f}}(t)\sigma^2_{\mathrm{f}}(t), \tag{4.3}$$

where $\omega_{\mathrm{b}}(t)$ and $\omega_{\mathrm{f}}(t)$ represent the probabilities of the background and foreground separated by a threshold t, and σ^2_{b} and σ^2_{f} are variances of these two classes.

The class probabilities $\omega_{\mathrm{b}}(t)$ and $\omega_{\mathrm{f}}(t)$ are computed from the L bins of the histogram:

$$\begin{aligned} \omega_{\mathrm{b}}(t) &= \sum_{i=0}^{t-1} p(i) \\ \omega_{\mathrm{f}}(t) &= \sum_{i=t}^{L} p(i), \end{aligned} \tag{4.4}$$

with p the probability of each pixel intensity. The histogram of the MNDWI image for Lake Mead acquired on August 26, 1998 is presented in Figure 4.2, with the Otsu's threshold identified at 0.178. As depicted in Figure 4.2(b), the threshold effectively distinguishes the two primary peaks in the histogram, where the left peak corresponds to land pixels and the right peak represents water pixels.

After the determination of the threshold value of the MNDWI image using Otsu's method, each pixel in the image with a radiometric measure value below the threshold is assigned a label of 0, indicating the surrounding land area, while each pixel with an intensity value exceeding the threshold is assigned a label of 1, indicating the water

mask.

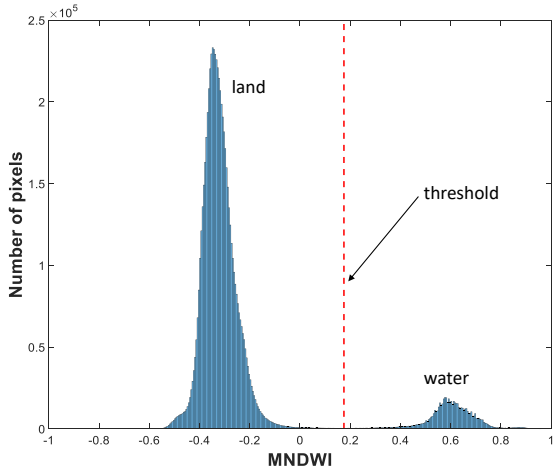

(a) Histogram of the MNDWI image.

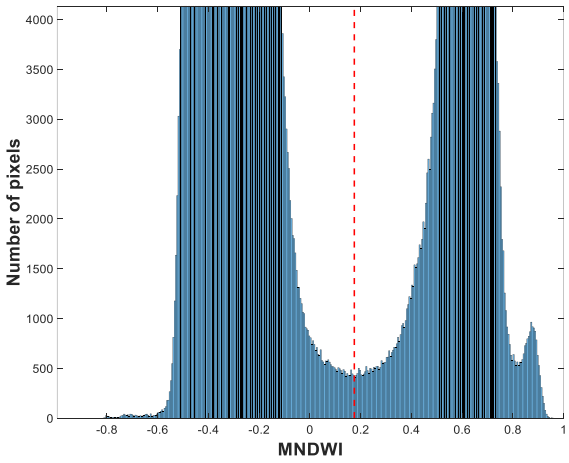

(b) Enlarged valley at the threshold between two peaks.

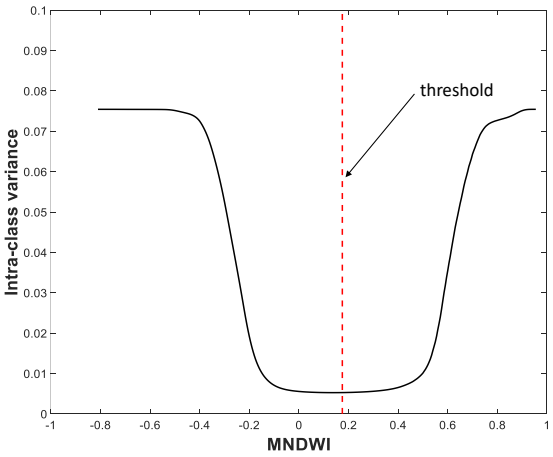

(c) Intra-class variance.

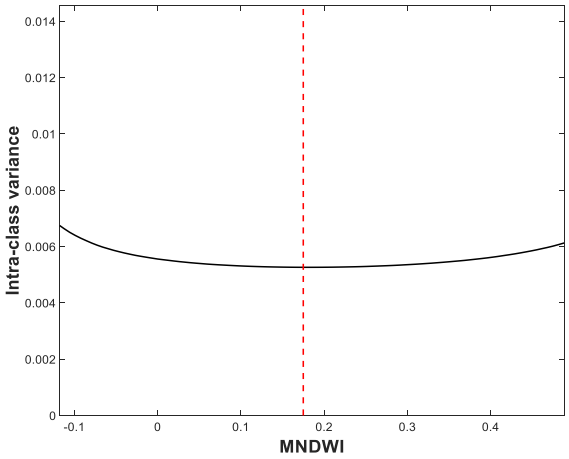

(d) Enlarged intra-class variance.

Figure 4.2: The result of the Otsu's algorithm classifying the water mask.

4.2.2 Lake profile extraction

To obtain bathymetry observations, it is necessary to extract nearshore topography from the ICESat-2 point cloud data along the track. In Figure 4.3(a), the track of the laser beam on the date of 18.01.2020 accompanied by a delineation of the clipped region, and the measurements of this region are shown in Figure 4.3(b). It can be seen that raw point data in the ATL03 product are noisy, with some noisy points resulting from the solar background and erroneous reflections of the water column. To obtain topography measurements that are relatively free of noise, the DBSCAN algorithm and the RANSAC algorithm are used to detect signal points of topography in this study.

These two algorithms will be introduced in detail as follows.

DBSCAN

DBSCAN stands for Density-Based Spatial Clustering of Applications with Noise, which is an algorithm first introduced by Ester et al. (1996) in their research. It is a popular clustering algorithm used in machine learning and data mining, which is particularly useful for datasets with arbitrary shapes, noisy data, and varying densities. DBSCAN groups points that are closely packed together in a dataset and identifies points that lie in low-density regions as noise or outliers. The algorithm requires two input parameters, which are ε and $MinPts$:

1. ε: The value of ε defines the radius of the neighborhood around each point. A point is considered to be part of a cluster if it is within the ε radius of at least $MinPts$ other points. The selection of ε is critical, as it heavily influences the clustering result. A common approach is to use a range of epsilon values and evaluate the resulting clusters based on their quality.

2. $MinPts$: The value of $MinPts$ determines how many points are required to form a cluster. If a point has fewer than $MinPts$ neighbors within the ε radius, it is considered to be an outlier. The choice of $MinPts$ also affects the clustering result, and it depends on the data and the problem domain.

In the context of DBSCAN clustering, the points to be clustered in a given space are subjected to a classification process based on a neighborhood radius parameter ε. This classification process distinguishes the points as core points, (directly-) reachable points and outliers, as described below:

- A point p is deemed a core point if there are at least $MinPts$ points within the distance of ε from it, including the point p itself.

- A point q is considered directly reachable from a core point p if it is within the distance of ε from p. It is important to note that points are only considered directly reachable from core points.

- A point q is deemed reachable from point p if there exists a path p_1, ..., p_n, with $p_1 = p$ and $p_n = q$, such that each p_{i+1} is directly reachable from p_i. Note that this implies that the initial point and all points on the path must be core points, with the possible exception of q.

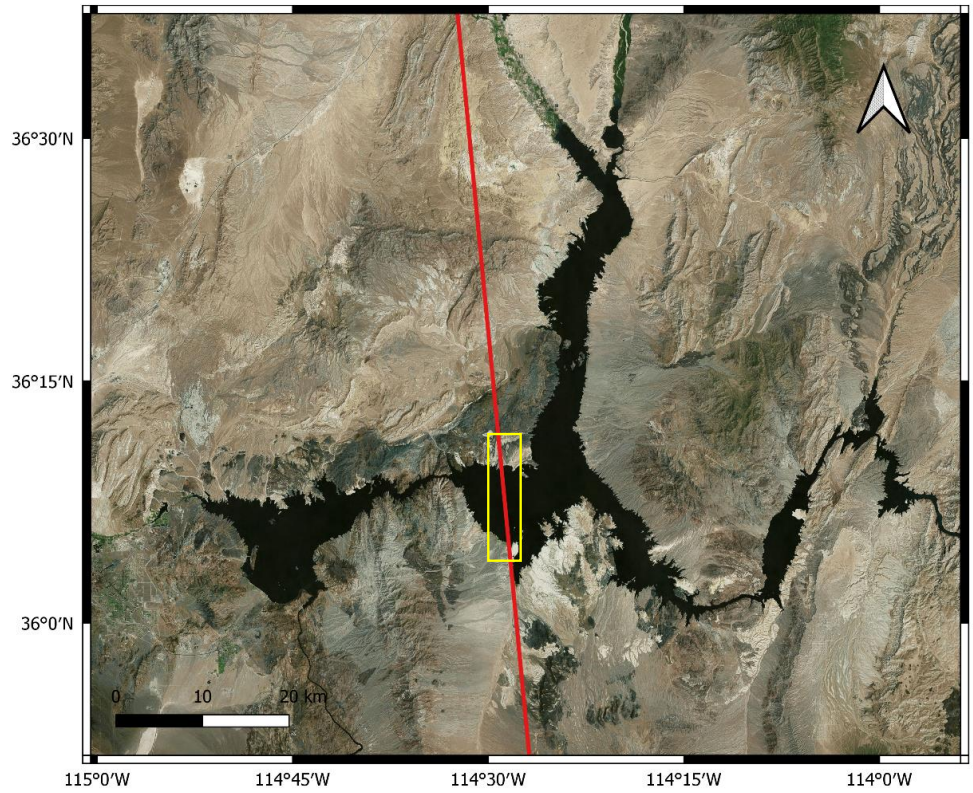

(a) The red line is the laser beam track and the yellow box is the clipped region.

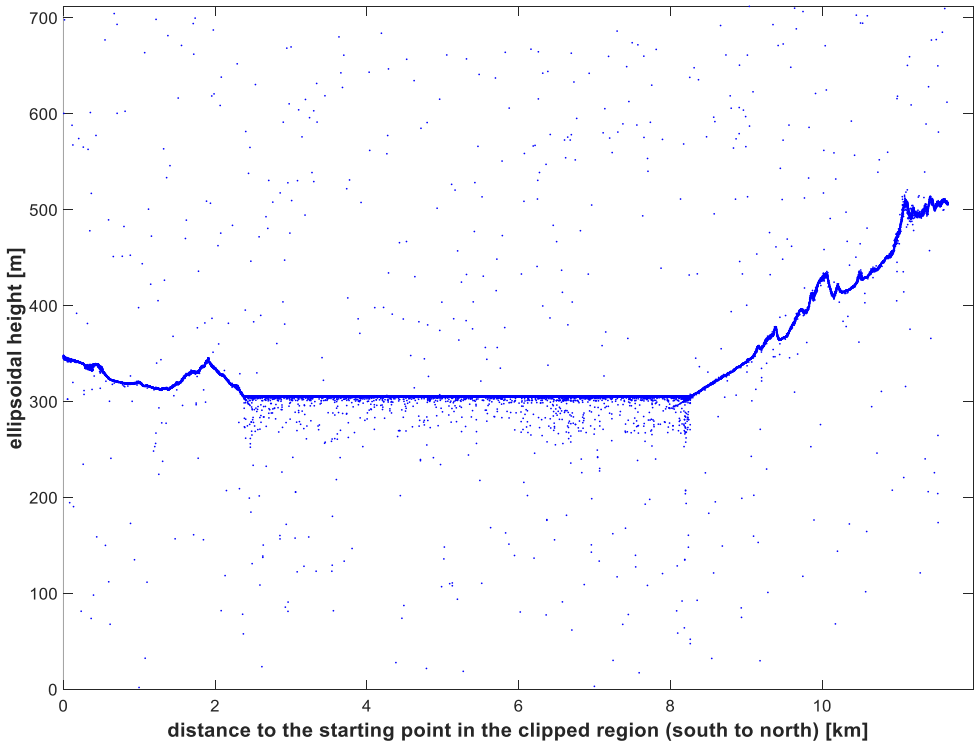

(b) The raw point cloud data along the track in the clipped region.

Figure 4.3: One example of the raw point cloud data from ATL03.

- Any point that is not reachable from any other point is classified as an outlier or a noise point.

An illustration of the DBSCAN procedure is depicted in Figure 4.4. The DBSCAN algorithm initiates by selecting a random point that has not been explored. The ε neighborhood of this point is then retrieved, and if it contains a sufficient number of points, a cluster is established. However, if the neighborhood has inadequate points, the point is labeled as noise. In order to formally define the extent of the clusters found by DBSCAN, a further notion of connectedness is required as reachability is not a symmetric relation. Only core points can reach non-core points, whereas the opposite is not true, and a non-core point may be reachable, but nothing can be reached from it. For this purpose, the notion of density-connectedness is introduced, where two points p and q are density-connected if there is a point o such that both p and q are reachable from o. Density-connectedness is a symmetric relation. A cluster satisfies two properties:

1. All points within the cluster are mutually density-connected.
2. If a point is density-reachable from some point of the cluster, it is also part of the cluster.

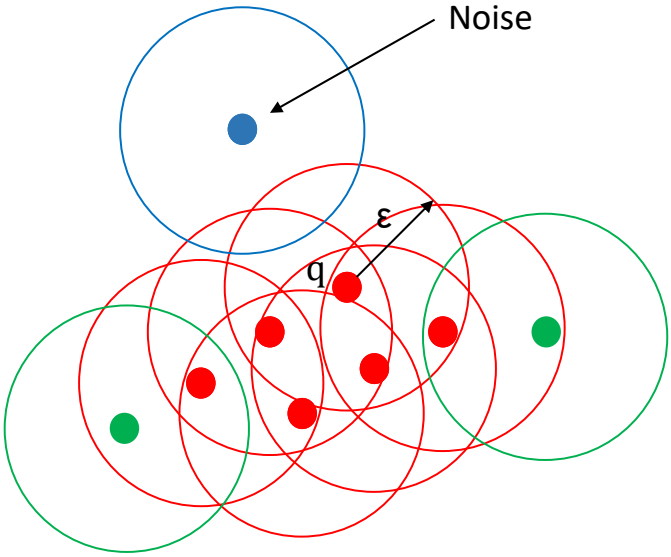

Figure 4.4: In this diagram, $MinPts = 4$. Point q and the other red points are core points because the area surrounding these points in an ε radius contains at least 4 points (including point q itself). Since they are all reachable from one another, they form a single cluster. Green points are not core points but are reachable from red points (core points), and thus belong to the cluster as well. The blue point is a noise point that is neither a core point nor a reachable point.

There is no fixed rule for choosing the values of the two parameters (ε and $MinPts$), as they depend on the densities of the different types of clusters and noises. In the process of DBSCAN, two parameters are influencing each other. Selecting an appropriate value for ε in DBSCAN is crucial, as a too small value may result in a significant portion of data remaining unclustered, while a large value can lead to the majority of data points being assigned to a single cluster. Typically, smaller values of epsilon are preferred, and it is recommended that only a small proportion of points should be within this distance of each other.

RANSAC

The Random Sample Consensus (RANSAC) algorithm is known to be less sensitive to noise and more sensitive to density (Fischler and Bolles, 1981). It has been successfully applied in many computer vision and image processing tasks, such as point cloud registration, object detection, and image segmentation (Tang et al., 2010). It is an iterative algorithm commonly used in computer vision and image processing to estimate model parameters from a set of observed data points that contain outliers or noise. The algorithm works by randomly selecting a minimal subset of data points (called a sample) and fitting a model to them. The model is then used to predict the parameters of the rest of the data points, and those that lie within a predefined threshold of the predicted values are considered as *inliers*. The RANSAC algorithm is designed to determine the optimal fitting result of a dataset that contains both inliers and outliers, by utilizing a voting scheme where data elements in the dataset are used to vote for one or multiple models. This voting scheme relies on two key assumptions: firstly, that the noisy features will not consistently vote for any single model (with few outliers); and secondly, that there are sufficient features to agree on a good model (with few missing data). The RANSAC algorithm is composed of two main iterative steps:

1. In the first step, a minimal subset of data elements is randomly selected from the input dataset, and a fitting model with model parameters is computed using only this subset of data elements. The number of data elements in this subset is sufficient to determine the model parameters.

2. In the second step, the algorithm checks which data elements from the entire dataset are consistent with the model instantiated by the estimated model parameters obtained from the first step. If a data element does not fit the model within some error threshold defining the maximum data deviation of inliers, it is

considered an outlier. The set of inliers obtained for the fitting model is known as the consensus set.

The RANSAC algorithm will continue to iterate these steps until the consensus set obtained in a certain iteration has the maximum number of inliers.

4.3 Study area and data

4.3.1 Study area

Lake Mead is selected as the study area for assessing and analyzing the performance of this method, see Figure 4.5. Lake Mead, formed by the construction of Hoover Dam in 1935, is the largest lake in the Colorado River basin in the United States. At an average inflow and lake volume, Lake Mead measures 180 km in length and 15 km in width, with a shoreline stretching 885 km; the maximum and mean depths of the lake are recorded at 158 m and 55.7 m respectively (Holdren and Turner, 2010). The Southwestern region of the United States, which is reliant on the Colorado River basin, has been experiencing drought periods in recent years. This lake is managed to guarantee a sufficient supply of water to the states involved. Especially the Southern Nevada population depends significantly on Lake Mead for their water supply, prompting concern that a persistent drought may cause the lake level to fall below the required pumping depth (Edalat and Stephen, 2019). Barsugli et al. (2009) has reported a probability of 50% that Lake Mead will become dry between 2035 and 2047, based on a simulation assuming a 20% reduction in inflow over 50 years due to climate change. For this reason, Lake Mead is a suitable study case due to its obvious variations in water level, area and volume. Another reason for selecting Lake Mead is that the surrounding areas have rare human activities, i.e. the DEM-like profiles from ICESat-2 are nearly constant. In preparation for the mission ICESat-2, a simulator called Multiple Altimeter Beam Experimental Lidar (MABEL), detected the bottom reflectance of the nearshore areas at Lake Mead sites, with a maximum depth of 10 m (Jasinski et al., 2016). ICESat-2 laser observations are supposed to be able to obtain the nearshore bathymetry of Lake Mead.

4.3.2 Data sets

In this study, the height measurements of the water and nearshore from the ICESat-2 ATL03 product, and the images from Landsat 5, 7 and 8 are used to estimate the water

level, area and volume of Lake Mead. To validate the method, *in-situ* data and other online databases are required. The following sections provide a brief introduction to these data sets.

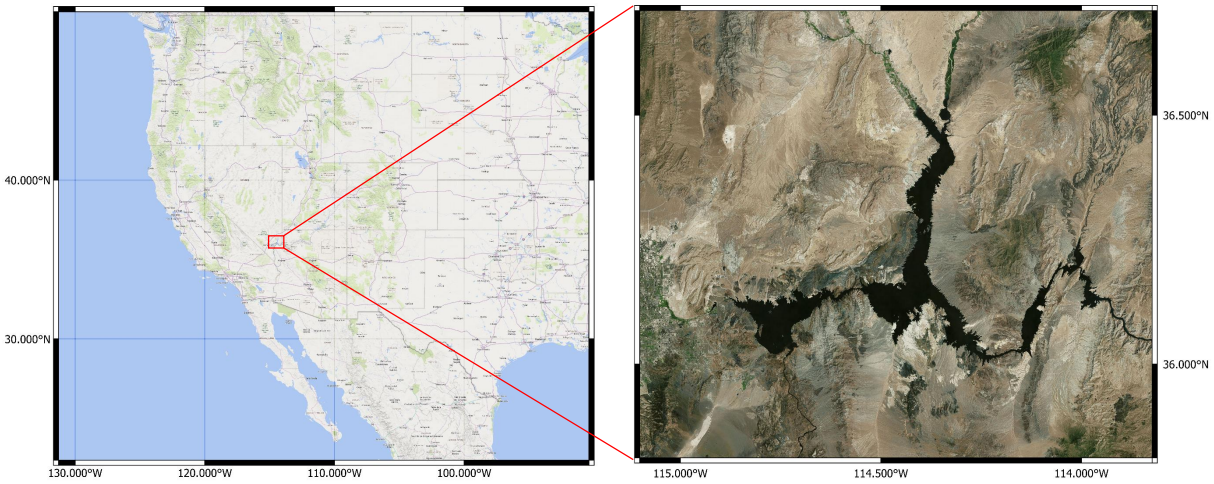

Figure 4.5: Location of Lake Mead, used as the study case in this thesis.

ICESat-2 ATL03

As the strong beams have a higher bathymetric capacity, this study only considers the data obtained from the strong beams. The data were obtained on 6 different epochs, with these data being on 20.10.2018, 12.02.2019, 14.05.2019, 18.01.2020, 15.01.2021 and 07.02.2021. These observations were intentionally selected in the middle region of the lake to minimize any effects on the water level and slope that could be caused by the narrow geometry, see Figure 4.6. Owing to the high sensitivity of photon counting detectors, the raw points in ATL03 datasets are very noisy. Noisy points are mainly caused by the solar background, especially in the daytime. Assuming a Poisson distribution for the noisy points (McGill et al., 2013), a confidence parameter ranging from 0 to 4 is provided, where higher values indicate greater confidence that the point is a signal (Neumann et al., 2021). However, the distribution of signal and noise points in the water column is significantly influenced by the attenuation and scattering effect, which makes the distribution of signal and noise points different from that of the atmosphere. Therefore, it is challenging to completely eliminate the noise points using the algorithm in ATL03 datasets.

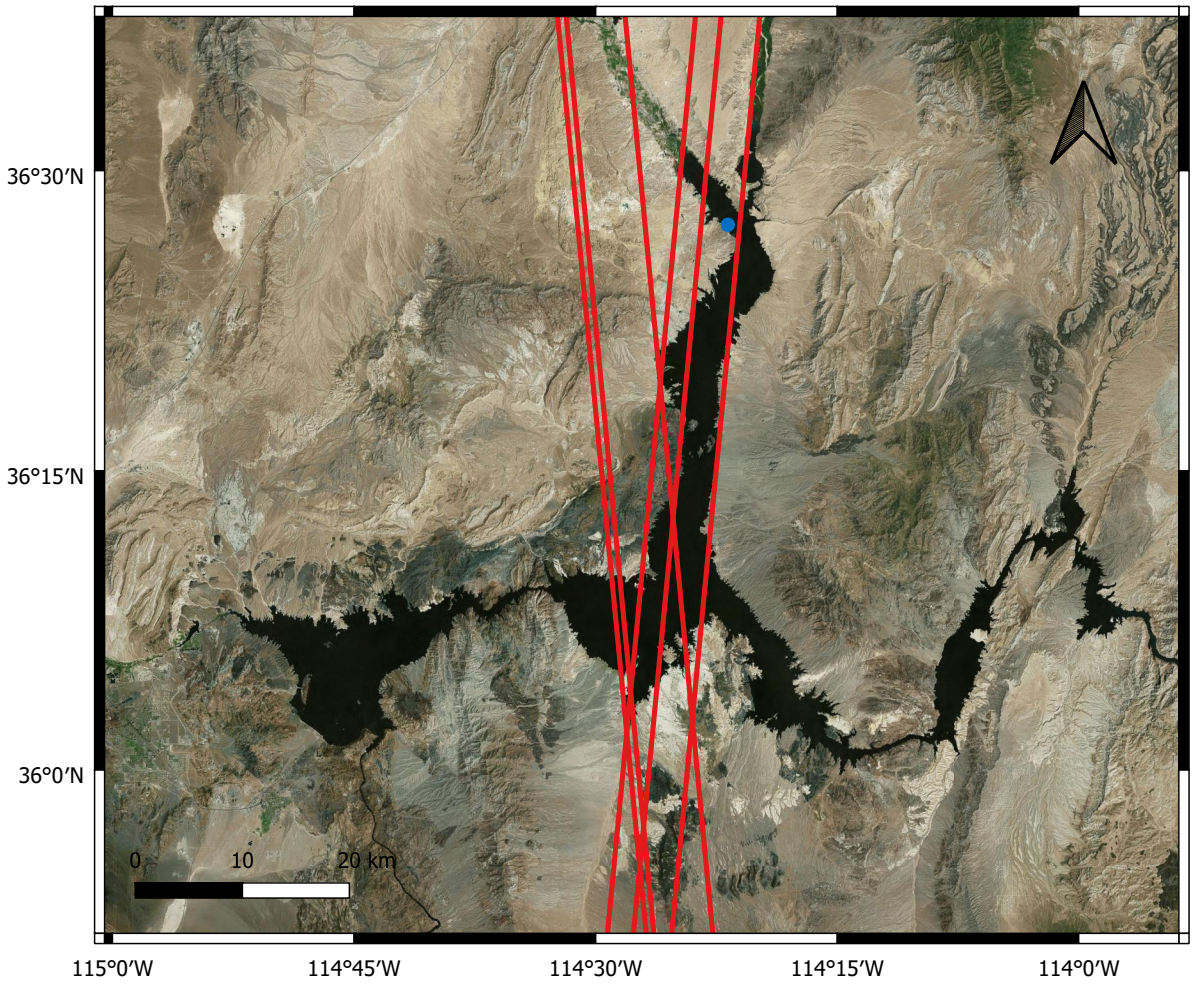

Figure 4.6: The distribution of 6 selected tracks (red lines) across Lake Mead and the *in-situ* station (blue point).

Landsat imagery

The Landsat satellites are a series of Earth-observing satellites jointly managed by the U.S. Geological Survey (USGS) and NASA. The Landsat program has been collecting satellite imagery of the Earth's surface since 1972, providing important data for a wide range of applications such as agriculture, land use and land cover change, natural resource management, and environmental monitoring. The most recent Landsat satellite, Landsat 9, was launched in September 2021 and continues the mission of its predecessors to provide high-quality and consistent Earth observations. Landsat 1 is the first Landsat satellite launched in 1972, and Landsat 2 and 3 are nearly identical copies of Landsat 1. The spatial resolution of these three satellites is 60 m in visible and near-infrared bands. Landsat 4 carried an updated Multi Spectral Scanner (MSS) used on previous Landsat missions, as well as a Thematic Mapper (TM), which improved the spatial resolution to 30 m. Landsat 5 operated from March 1984 until its retirement in June 2013. It was designed to be an improved version of Landsat 4. The Landsat 5 sensor has a higher signal-to-noise ratio (SNR), which makes the images it captures of higher quality. That's the reason images are selected from 1984 onwards in this study. Table 4.1 provides information of Landsat 5 spectral bands.

Table 4.1: Resolution of each band of Landsat 5 TM

Bands	Description	Spectral range [μm]	Spatial resolution [m]
1	Blue	0.45–0.52	30
2	Green	0.52–0.60	30
3	Red	0.63–0.69	30
4	NIR	0.76–0.90	30
5	SWIR-l	1.55–1.75	30
6	Thermal	10.40–12.50	120
7	SWIR-2	2.08–2.35	30

Landsat 6 was a satellite launched in 1993 by NASA with the goal of continuing the Landsat program. However, the satellite failed to reach orbit due to a rocket launch failure, and thus it never provided any data. Landsat 7 was launched in April 1999 and retired in April 2022. It carries the Enhanced Thematic Mapper Plus (ETM+) instrument, which has visible and infrared bands with a spatial resolution of 30 m, a thermal band of 60 m and a panchromatic band of 15 m. Table 4.2 provides information of Landsat 7 spectral bands.

Table 4.2: Resolution of each band of Landsat 7 ETM+

Bands	Description	Spectral range [μm]	Spatial resolution [m]
1	Blue	0.45–0.52	30
2	Green	0.52–0.61	30
3	Red	0.63–0.69	30
4	NIR	0.76–0.90	30
5	SWIR-l	1.55–1.75	30
6	Thermal	10.40–12.50	60
7	SWIR-2	2.08–2.35	30
8	Panchromatic	0.52–0.90	15

Landsat 8 was launched in February 2013 and is still active now. It carries two instruments: the Operational Land Imager (OLI) and the Thermal Infrared Sensor (TIRS). The OLI provides 8 spectral bands with a spatial resolution of 30 m and one panchromatic band with a spatial resolution of 15 m. The TIRS provides two long wave thermal bands with a spatial resolution of 100 m. Table 4.3 shows the details of Landsat 8 spectral bands.

Table 4.3: Resolution of each band of Landsat 8 OLI and TIRS

Bands	Description	Spectral range [μm]	Spatial resolution [m]
1	Coastal-Aerosol	0.43–0.45	30
2	Blue	0.45–0.51	30
3	Green	0.53–0.59	30
4	Red	0.64–0.67	30
5	NIR	0.85–0.88	30
6	SWIR-l	1.57–1.65	30
7	SWIR-2	2.11–2.29	30
8	Panchromatic	0.50–0.68	15
9	Cirrus	1.36–1.38	30
10	TIR-1	10.6–11.2	100
11	TIR-2	11.5–12.5	100

The satellites' tracks of Path 39 and Row 35 cover the study area, with a temporal resolution of 16 days for Landsat 5, 7 and 8. Landsat 7 has a well-known issue with its Scan Line Corrector (SLC), which is responsible for compensating for the forward motion of the satellite during imaging. In May 2003, a hardware failure caused the SLC to no longer function properly, resulting in the appearance of large diagonal gaps

or black stripes in the images known as "SLC-off" gaps, which ruin about 22% of each image (Elmi, 2019). Hence, the Landsat 7 images acquired after the SLC-off event will not be used. In this study, the Landsat 5 images were acquired from 1984 to 2011, followed by Landsat 7 images from 1999 to 2003, and Landsat 8 images from 2013 to 2021. In total, there are 484 cloud-free Landsat images from 1984 to 2021, except 2012. The annual average number of images is 12.9. Figure 4.7 displays the distribution of the images per year.

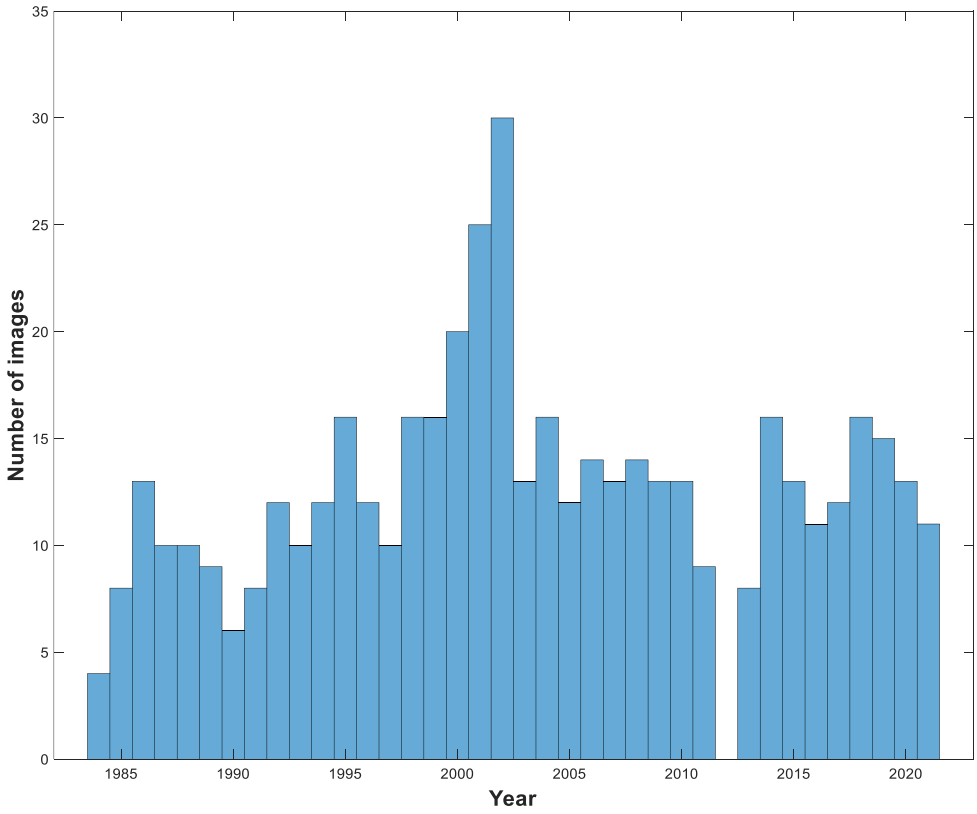

Figure 4.7: Number of images in each year from 1984 to 2021.

In-situ data

Lake Mead was created by the filling of water following the completion of Hoover Dam. Prior to construction, a meticulous survey of the inundated area was conducted, resulting in the production of a detailed topographic map. The gauge station started its recording once the reservoir began to fill with water. The *in-situ* data are available at https://lakemead.water-data.com/, which is the Lake Mead Water Database. The database contains daily recordings of water levels, volumes, inflows, outflows, and temperatures since 1935. The water levels and volumes of the *in-situ* data are used to evaluate the results estimated from the proposed method.

DAHITI

Since the *in-situ* data cannot provide the water area variations, the online database called DAHITI is utilized. DAHITI, the Database for Hydrological Time Series of Inland Waters, was developed by DGFI-TUM (Deutsches Geodätisches Forschungsinstitut, Technische Universität München) (Schwatke et al., 2015, 2019). The time series of the water surface area is generated from optical imagery with spatial resolutions of between 10 m (Sentinel-2) and 30 m (Landsat). The water area data are available from 1984 to 2020, also except 2012.

4.4 Estimation of water levels and volumes

4.4.1 Data processing

Figure 4.8(a) shows the original Landsat image with Green band and SWIR bands on August 26, 1998, and Figure 4.8(b) is the extracted water mask after water mask extraction.

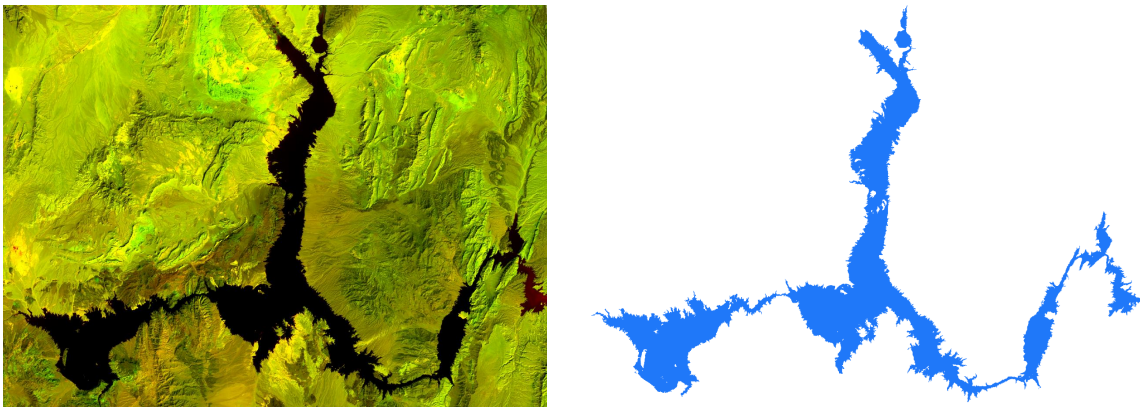

(a) Landsat image with Green and SWIR bands. (b) Extracted water mask.

Figure 4.8: The result of water mask extraction.

The Landsat image series are subjected to this procedure, resulting in the generation of a binary lake mask for each image. Considering the spatial resolution of 30 m, the area of each pixel amounts to 900 m^2. With N pixels indicating water, the lake area becomes

$$A = 900\ \mathrm{m}^2 \cdot N. \tag{4.5}$$

The extraction of the lake boundary is a straightforward process that involves identifying the boundary between pixels' values classified as 0 and 1. Subsequently, the identified boundary will be utilized to intersect the laser tracks and retrieve height information in the next step.

For the lake nearshore profile extraction, there are two steps required to extract the lake profile when implementing the DBSCAN algorithm. When operating the DBSCAN algorithm, the ICESat-2 points along the track are considered to be in a 2-dimensional framework, i.e. the vertical direction and the along-track direction. The first step, referred to as *Global Detection*, involves the removal of noise points. Empirically, radius ε should be larger than 2 m to detect ground topography (Zhang and Kerekes, 2014). Thus, in this study the radius ε is set to 2.5 m, and the selection of $MinPts$ depends on the value of ε. A corresponding adaptive threshold $MinPts$ is given in Eq. (4.6), which is based on the empirical rule of minimum point number for DBSCAN algorithm (Ma et al., 2019).

$$MinPts = \frac{2SN_1 - SN_2}{\ln\left(\frac{2SN_1}{SN_2}\right)}. \tag{4.6}$$

SN_1 represents the estimated total number of points (including noise and signal points) within the given circular neighborhood. The equation is expressed as:

$$SN_1 = \frac{\pi\varepsilon^2 N_1}{hl}, \tag{4.7}$$

where N_1 is the number of points in total (including noise and signal points), h is the vertical range, and l is the along-track range. For the case of Figure 4.3(b), the vertical range is approximately 700 m and the along-track range is about 12 km.

SN_2 is an indicator for the estimated number of noise points within a specific neighborhood. The size of the vertical window of ICESat-2 varies depending on the area, terrain type, and elevation changes, and can range from tens to hundreds of meters (Markus et al., 2017). Typically, signal photons from the Earth's surface are concentrated in the middle of the vertical window, while noise points are distributed throughout the entire window. In particular, almost all points at the top and bottom of the window are noise points, with the dominant source being solar-induced background noise scattered by atmospheric and water column particles. Noise point density is generally higher in the water column, where the underwater bottom corresponds to lower elevation values compared to the ground surface. To accommodate different regions and surface types, the points at the top and the bottom parts of the window are used (where

most photons are noise photons) to estimate SN_2 within the given neighborhood using the following equation:

$$SN_2 = \frac{\pi\varepsilon^2 N_2}{h_2 l}. \tag{4.8}$$

N_2 represents the number of points located in the top or bottom vertical range, while h_2 denotes the height of the selected vertical range. For the case of Figure 4.3(b), the vertical range is 200 m at the bottom. The basic criterion for identifying a signal point is that, for each point p in a cluster, its point density within a 2D circular neighborhood is calculated. If the point density exceeds the threshold value of $MinPts$, point p is designated as a signal point. The circular neighborhood is defined by the Euclidean distance between points p and q. Then after the *Global Detection* process, most solar background noise points are discarded, which forms a relatively clean point cloud, see Figure 4.9.

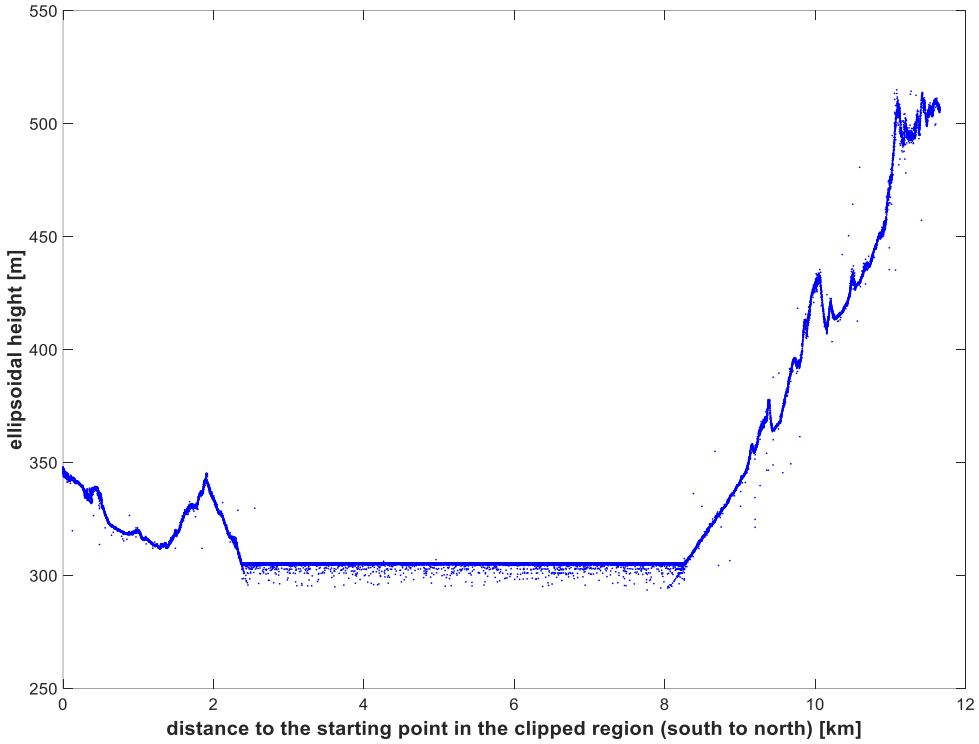

Figure 4.9: Most noise points are removed by the first step, creating a relatively clean topography.

In order to derive the bathymetry of the nearshore region, it is essential to preserve the lake floor beneath the water surface. Thus, the reflections from the water should be removed, which can also be clustered by the DBSCAN algorithm. That is the second step, which is referred to as *Local Detection*. Due to the stability of the lake surface, the

vertical range of the reflections from the interface and subsurface column backscattering layer is about 40 cm. The radius ε is set to 20 cm. Because of the attenuation and scattering effect in the water column, the density of the signal points from the 2D layer is much higher than that of other types of topography. The parameter $MinPts$ is set to half the density of the layer. The water surface is then clustered by the *Local Detection*, as depicted by the blue points in Figure 4.10.

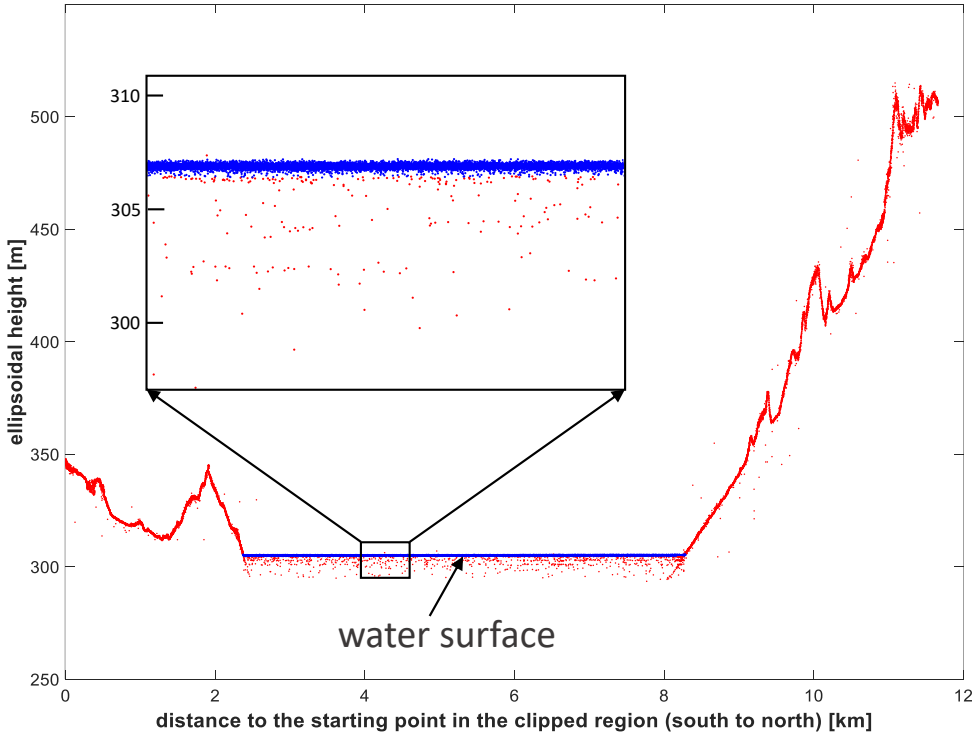

Figure 4.10: Clustered water surface.

After the water surface is removed, there may still be a considerable amount of noise present below the water surface. To mitigate the effects of noise in the nearshore region, we partition it into smaller segments that can be assumed as linear slopes. The RANSAC algorithm is then applied to each segment. Figure 4.11 shows the detected nearshore topography observations (red points) by the RANSAC algorithm with the exclusion of water column noise.

RANSAC allows us to extract the topography under the water, which expands the boundaries of the bathymetry. However, the topography under the water surface must be corrected due to the impact of water refraction. At present, the refraction and its effect on the speed of light at the interface between air and water are not taken into consideration in the ICESat-2 products. This causes the measured locations below the water surface to appear deeper and deviate further from the nadir direction than their

actual positions. Since the satellite rotates at an angle (0°–1.65°) to measure more topographies when it passes over the land areas, the three pairs of laser beams are always off-nadir (Neumann et al., 2021). The geometry of the refraction scheme is depicted in Figure 4.12, illustrating the angle of incidence that occurs when the laser light travels from the air to the water.

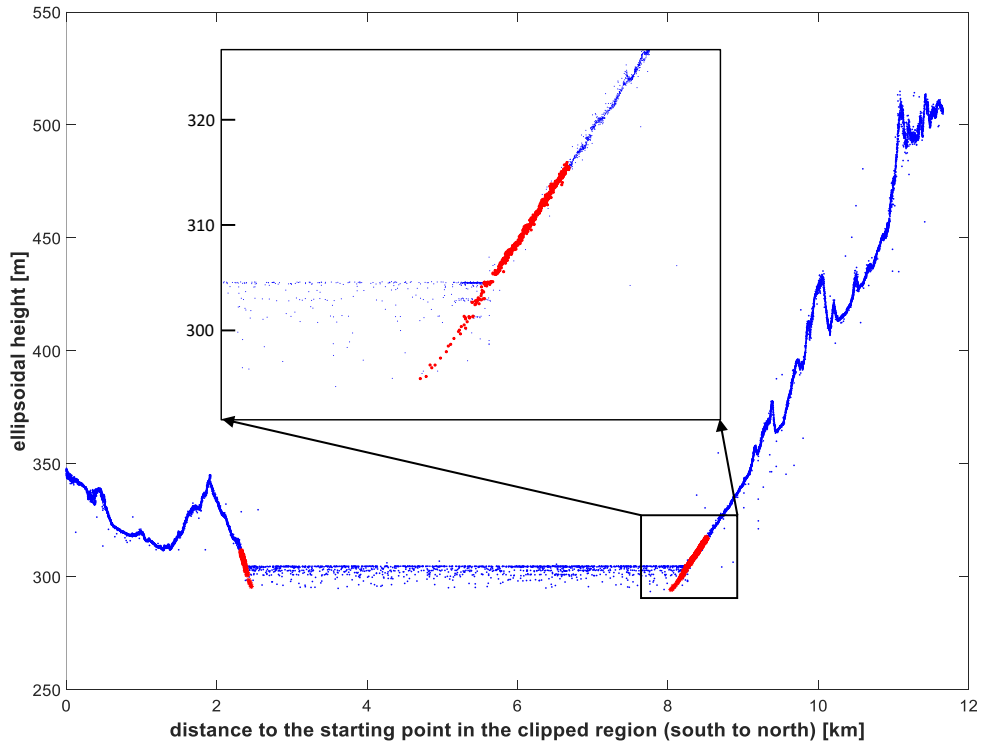

Figure 4.11: Detected nearshore topography observations.

In Figure 4.12, θ_1 represents the angle of incidence, θ_2 is the angle of refraction ($\theta_3 = \theta_1 - \theta_2$), D denotes the uncorrected depth that is obtained by taking the difference between the Z coordinates of the water surface and uncorrected bottom return points, S represents the slant range to the uncorrected bottom return point location, R is the corrected slant range, P represents the distance between the uncorrected and corrected photon return points in the plane, and the other angles and distances are as labeled in the figure. The refraction indexes of air and water are n_1 and n_2 respectively. In order to calculate the true positions of the observations under the water, Snell's law should be referred to as follows:

$$\frac{\sin\theta_1}{\sin\theta_2} = \frac{n_1}{n_2}, \tag{4.9}$$

where the parameters θ_1, n_1 and n_2 are known.

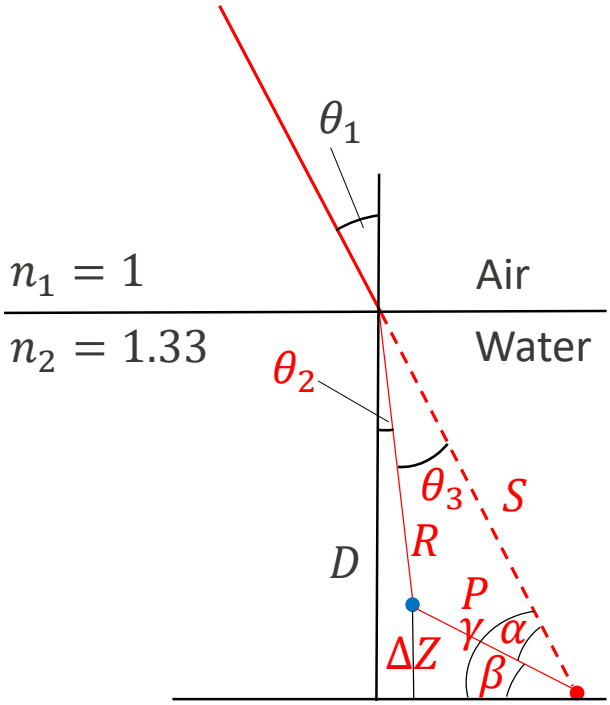

Figure 4.12: Scheme of geometry of refraction.

The uncorrected depth D can be obtained from ATL03 data. The relationship between D and S in the triangle follows:

$$S = \frac{D}{\cos\theta_1}. \tag{4.10}$$

As a consequence of the variation in the speed of light at the air-water interface, the relationship between R and S can be expressed as follows:

$$R = \frac{Sn_1}{n_2}. \tag{4.11}$$

Then, solving the geometry problem, yields

$$P = \sqrt{R^2 + S^2 - 2RS\cos\theta_3}. \tag{4.12}$$

then,

$$\alpha = \arcsin\left(\frac{R\sin\theta_3}{P}\right). \tag{4.13}$$

Since $\gamma = \frac{\pi}{2} - \theta_1$ and α is calculated, then $\beta = \gamma - \alpha$. Finally, the vertical correction is obtained as:

$$\Delta Z = P\cos\beta. \tag{4.14}$$

Figure 4.13 shows the nearshore bathymetry following the application of refraction correction. It can be seen that the deepest measurement is situated about 8 m below

the water surface with the corresponding vertical correction of 2.7 m. That means the limit of bathymetry is enlarged by about 8 m in this case. Since the angle of incidence θ_1 (0°–1.65°) and the bathymetry depth (up to 30 m depending on the turbidity of the water) are relatively small, the horizontal correction can be considered insignificant when compared to the 30 m pixel size of the image.

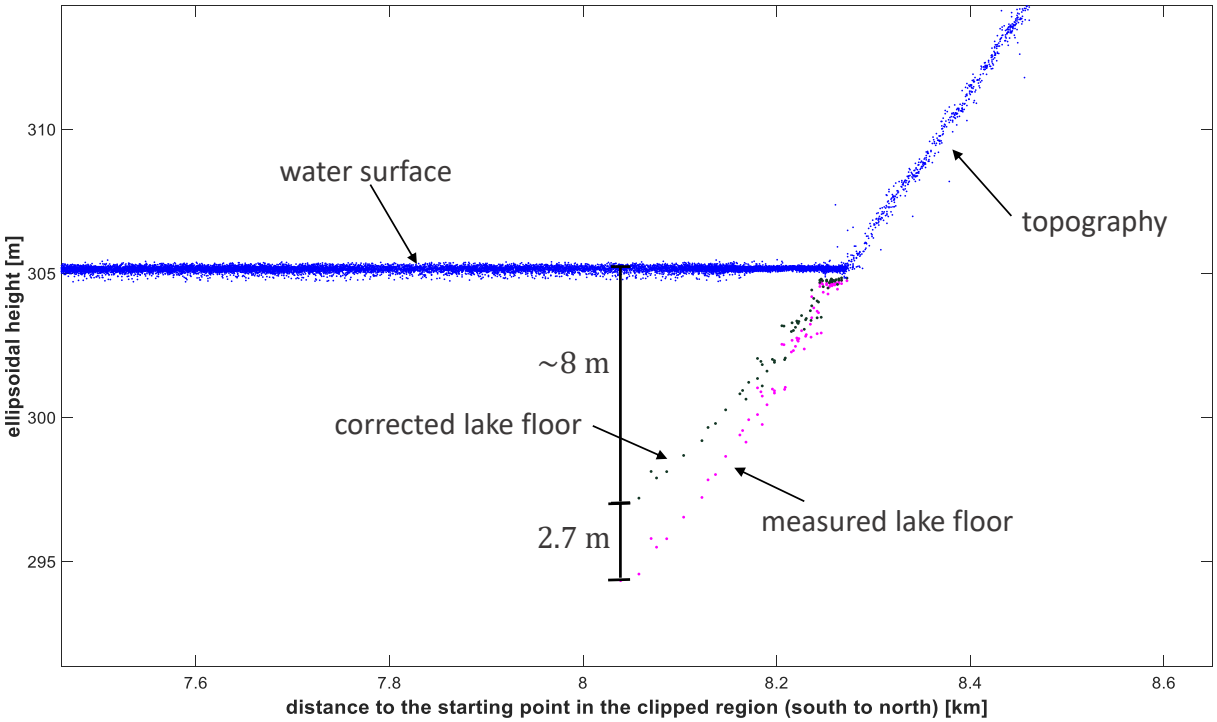

Figure 4.13: Nearshore bathymetry after refraction correction: pink points are original lake floor measurements; dark green points are corrected lake floor measurements.

4.4.2 Estimation of water levels

Since the surrounding areas of Lake Mead lack human activities, it may be assumed that the nearshore topography remained relatively stable from 1984 to 2021, i.e., the measurements of 6 laser tracks in Section 4.3 can serve as a representative sample of the ground profiles and lake floor profiles in the whole time period. After discarding the noise points and extracting the nearshore topography measurements, a more refined profile of the point cloud can be obtained with accurate positions and elevations.

Once the position of the intersection between the nearshore profile and the water boundary has been determined as mentioned above, the laser points within a 30 m radius of the intersection will be selected, considering that the spatial resolution of the

boundary is 30 m. Assuming a linear slope for a small segment of 60 m, the elevations of measurements in the segment can be fitted as a linear model using the RANSAC algorithm. Since the coordinates of the intersection are known, the elevation of the intersection can be estimated. When 6 laser tracks project on the classified water mask of one date, there will be at least 12 intersections (depending on the area of the water mask in each date) between the water boundary and tracks, see Figure 4.14. Using the same approach, all elevations of intersections of the 6 tracks are estimated. In order to eliminate gross errors, the 3σ-criterion is employed. Subsequently, the median elevation value is used to define the water level at the time the image was acquired. All water levels corresponding to the dates of image acquisition will be estimated by replicating the aforementioned procedure.

4.4.3 Estimation of water volumes

A contour-based methodology is proposed to estimate the water volume of the lake during the study period, which integrates Landsat-derived water areas (see Subsection 4.4.1) and laser profile-derived water levels (see Subsection 4.4.2). The methodology involves sorting the water levels in ascending order of time, followed by sorting the lake areas based on the determined order of the water level data. By combining various lake boundaries with their corresponding water levels, a three-dimensional (3D) topography of the lake can be generated. Consequently, the volume change between two adjacent dates can be calculated by assuming the shape of the lake volume between two contours as a 3D trapezoid, as follows:

$$\Delta V_i = V_{i+1} - V_i = \frac{H_{i+1} - H_i}{3} \left(S_{i+1} + S_i + \sqrt{S_{i+1} S_i} \right). \tag{4.15}$$

H_{i+1} and H_i are the water levels of two adjacent dates, while S_{i+1} and S_i are the corresponding lake areas respectively. The water volume variation between two adjacent dates can be either positive or negative. The water volume of the date of the first image acquisition is defined as the reference V_1. Then, the water volume difference between Day_1 and a specific date Day_n can be calculated by accumulating all water volume changes of the adjacent dates before Day_n. As a result, the water volume of Day_n can be expressed as:

$$V_n = V_1 + \sum_{i=1}^{n-1} \Delta V_i. \tag{4.16}$$

Finally, the water volume of each date of image acquisition from 1984 to 2021 can be calculated by repeating the aforementioned procedure.

Thus far, estimations have been made regarding the water level, area, and volume for each image acquisition date. It is possible to establish a relationship between the level, area, and volume using a large amount of imagery data collected between 1984 and 2021 and the nearshore profiles obtained from ICESat-2. Consequently, once the water level is obtained through the use of satellite altimeters or *in-situ* methods, it would be feasible to predict the other two variables. Similarly, if the water area is determined through satellite imagery, it would be possible to predict the remaining two variables.

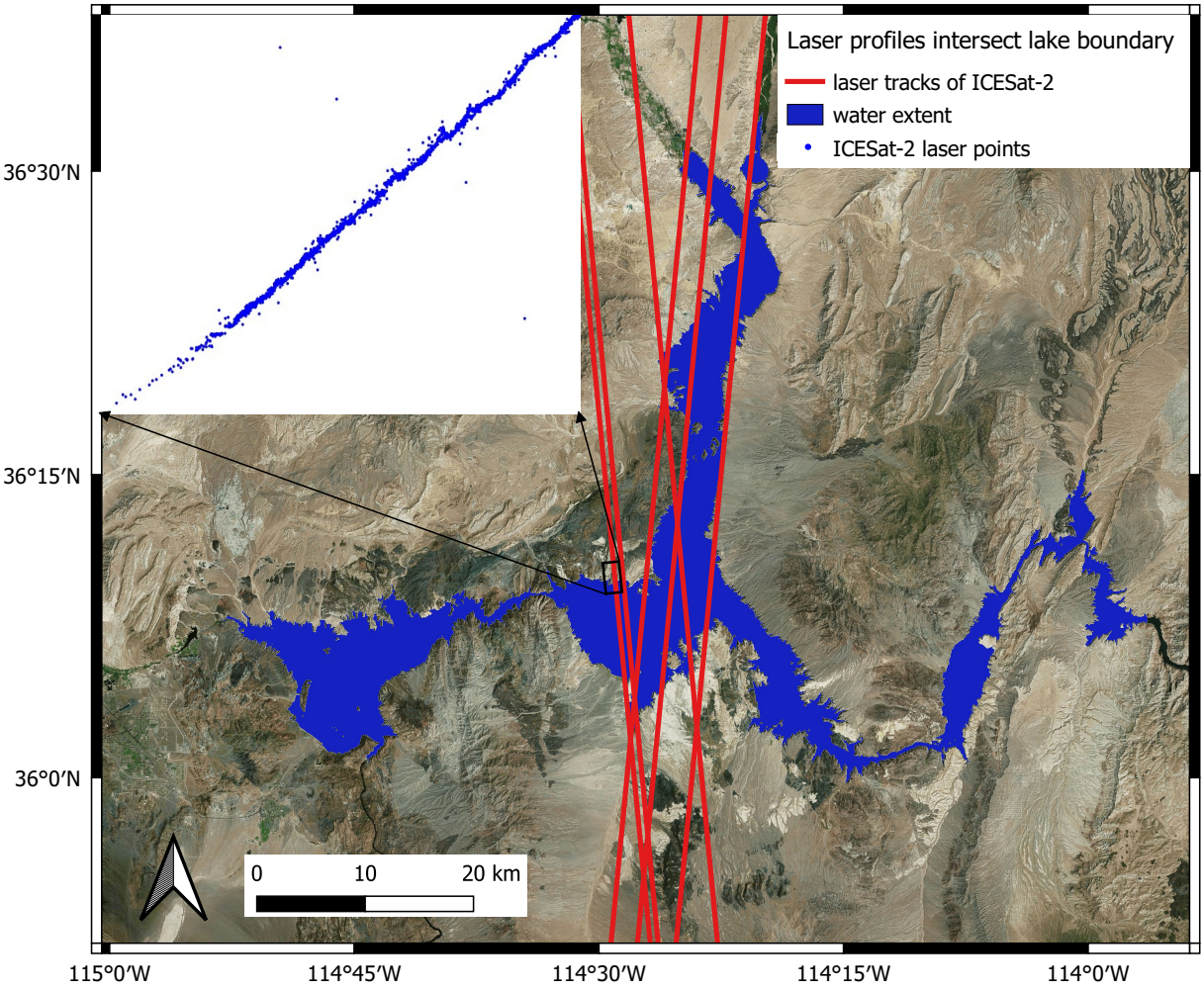

Figure 4.14: The laser tracks of ICESat-2, shown as red lines intersect with the derived water mask. The nearshore section profile is displayed in an enlarged rectangular in the upper left corner. The measurements of the lake floor are illustrated in the lower left corner of the rectangular and exhibit a lower density than the other segment of the profile.

4.5 Results and validation

4.5.1 Estimated water levels comparison with *in-situ* data

Using the methods mentioned in Subsection 4.2, the process of extracting water masks from Landsat images of Lake Mead spanning the years 1984 to 2021 was carried out. Subsequently, surface profiles pertaining to both the underwater bottom and ground were identified from the ATL03 data. Finally, a matching of laser profiles and the lake mask was undertaken to determine the water level corresponding to each image acquisition date within the aforementioned time frame.

As mentioned in Section 4.3, the laser tracks were obtained on 6 acquisition dates, with these dates being on 20.10.2018, 12.02.2019, 14.05.2019, 18.01.2020, 15.01.2021 and 07.02.2021, i.e., the water levels of these dates were directly measured by ICESat-2 laser altimeter. Assuming hydrostatic equilibrium of the lake surface, it theoretically serves as an isosurface of gravity potential (Zlinszky et al., 2014). Given the relatively minor fluctuation in gravitational acceleration at the central lake under study, it is assumed that any difference in along-track anomalies between dynamic height and orthometric height can be negligible, i.e., we assume that the orthometric height of the central lake surface is nearly constant. Therefore, the water level can be represented by the median value of orthometric heights of the water surface measurements along the track from ATL13 data. The water levels of these 6 epochs are calculated to be shown in Table 4.4. The *in-situ* data has a temporal resolution of 1 day; thus, to enable a comparison with ICESat-2 measured water levels, water level variation within 1 day is not taken into account. The root mean square error (RMSE) water levels between ICESat-2 measured and *in-situ* data is calculated to be 4.7 cm.

Table 4.4: Orthometric height comparison between ICESat-2 and *in-situ*

dates	ICESat-2	*in-situ*
20.10.2018	328.87 m	328.81 m
12.02.2019	331.01 m	330.95 m
14.05.2019	331.71 m	331.65 m
18.01.2020	333.18 m	333.16 m
15.01.2021	330.71 m	330.68 m
07.02.2021	331.30 m	331.32 m

If the underwater bottom profile cannot be observed, it is imperative to lower the water level as much as possible in order to produce more bathymetric topography. The lowest water level of these 6 dates occurred on the date of 20.10.2018 with a water level of approximately 329 m. That means if the water level is below 329 m, it becomes unfeasible to estimate the water level. The method detailed in Subsection 4.4.1 yielded the deepest lake floor with a depth of approximately 8 m, and subsequently reduced the limit of the estimated water level to around 321 m.

The 6 tracks and corresponding water masks will exhibit more than 12 intersections, and the water level of each intersection can be estimated, as illustrated in Figure 4.15. For each image acquisition date, outliers in water levels will be identified and discarded through the application of a threefold standard deviation method. After outlier rejection, the standard deviation of water levels across each acquisition date ranges from 21 cm to 52 cm. Subsequently, the estimated water level for each acquisition date can be derived by computing the median value of all intersecting water levels, excluding outliers. The estimated water levels from 1984 to 2021 are compared with *in-situ* water levels in Figure 4.16; both datasets are in orthometric height (H) (the estimated water levels are labeled by blue points and the *in-situ* water levels are labeled by a red curve). The orange dashed line represents the water level that was captured by ICESat-2 on 20.10.2018. The green dashed line shows the lowest water level that can be estimated theoretically due to the extraction of the underwater lake floor. According to the *in-situ* data, the lowest water level of Lake Mead occurred at the end of 2021, with a value of about 324 m. Because the ICESat-2 laser light penetrates the water to get the nearshore underwater topography, all the images can be used to estimate the water level even if the actual water level of that image acquisition time is lower than the water level when captured by ICESat-2. The figure illustrates a higher density of blue data points between 1999 and 2003 in comparison to the other temporal intervals. This can be attributed to the combination of images obtained from Landsat 5 and Landsat 7 during this period. Obviously, no image is used in the year 2012, resulting in the absence of estimated water level data for that year. The average difference and the RMSE of water levels between our results and *in-situ* measurements are computed to be 65 cm and 73 cm, respectively. The correlation coefficient (ρ) and the coefficient of determination (R^2) between the estimated water levels and *in-situ* water levels are both 0.998. The estimated water levels using Landsat 5, Landsat 7 and Landsat 8 are also compared with *in-situ* data separately, as shown in Table 4.5.

Table 4.5: Comparison between estimated water levels and *in-situ* data

Parameters	Landsat 5	Landsat 7	Landsat 8
Mean absolute difference (cm)	58	58	87
RMSE (cm)	68	65	92
ρ	0.998	0.999	0.995
R^2	0.998	0.998	0.996

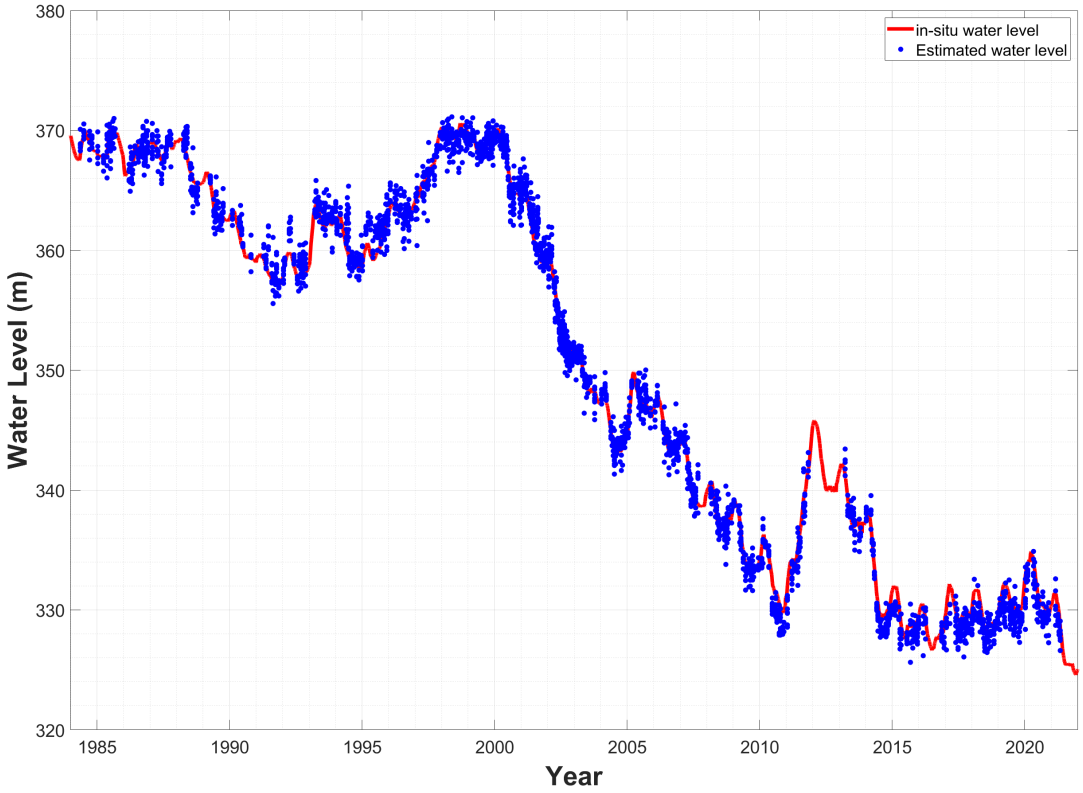

Figure 4.15: The estimated water levels of all the intersections of each image acquisition date and *in-situ* water levels of each date.

The assessment parameters show minimal differences between Landsat 5 and Landsat 7. However, the estimated water levels from Landsat 8 show considerably larger errors in comparison with Landsat 5 and 7. Landsat 8 images span the years from 2013 to 2021. As shown in Figure 4.16, it's noteworthy that numerous water level values after 2013 rely on ICESat-2 track profiles situated beneath the water's surface. This is likely the primary factor contributing to the amplified estimation error, as the larger error in the profile beneath the water's surface has a cascading effect on the overall accuracy.

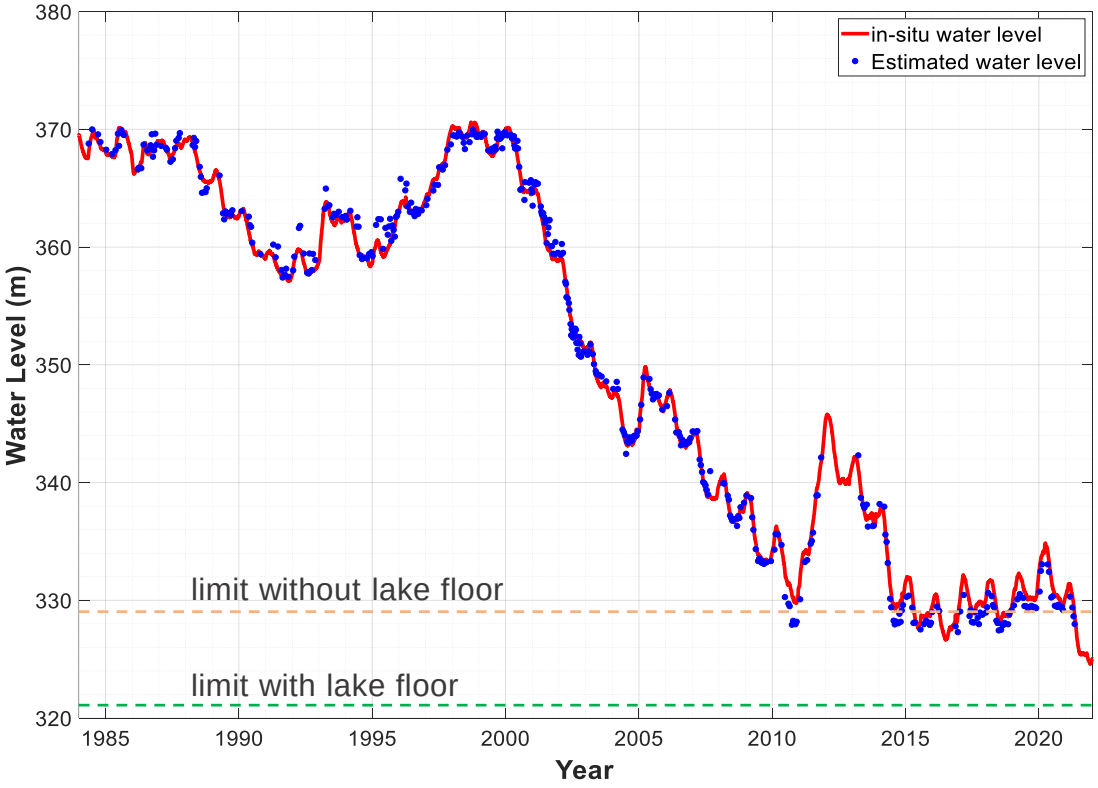

Figure 4.16: Comparison between the estimated water levels using our method and *in-situ* water levels.

4.5.2 Estimated water areas comparison with DAHITI data

The water area of each image acquisition date was estimated in Subsection 4.2.1. As the area of one pixel is known, the water area depends on the number of water pixels classified. From the results of classified water masks, the largest water area appeared on December 27, 1999 and the smallest water area appeared on August 1, 2018. Figure 4.17 clearly shows an obvious variation in the boundaries of the lake on the two respective dates. The corresponding area values illustrate a difference between a maximum of 550.96 km^2 and a minimum of 297.36 km^2.

Since no *in-situ* measurements for Lake Mead surface areas are available, we employed the water area time series of Lake Mead from the DAHITI data set. The lake area comparison between our results and the DAHITI data set is shown in Figure 4.18 (the water areas from our method are labeled by blue points and the DAHITI water areas are labeled by a red curve). The data gap in the red curve occurs in 2012 because of the SLC-off of Landsat 7. The difference between the two data sets is large before 2001, which can be up to about 60 km^2. It is difficult to evaluate the accuracy of our classification method because both data sets are not compared with the ground truth.

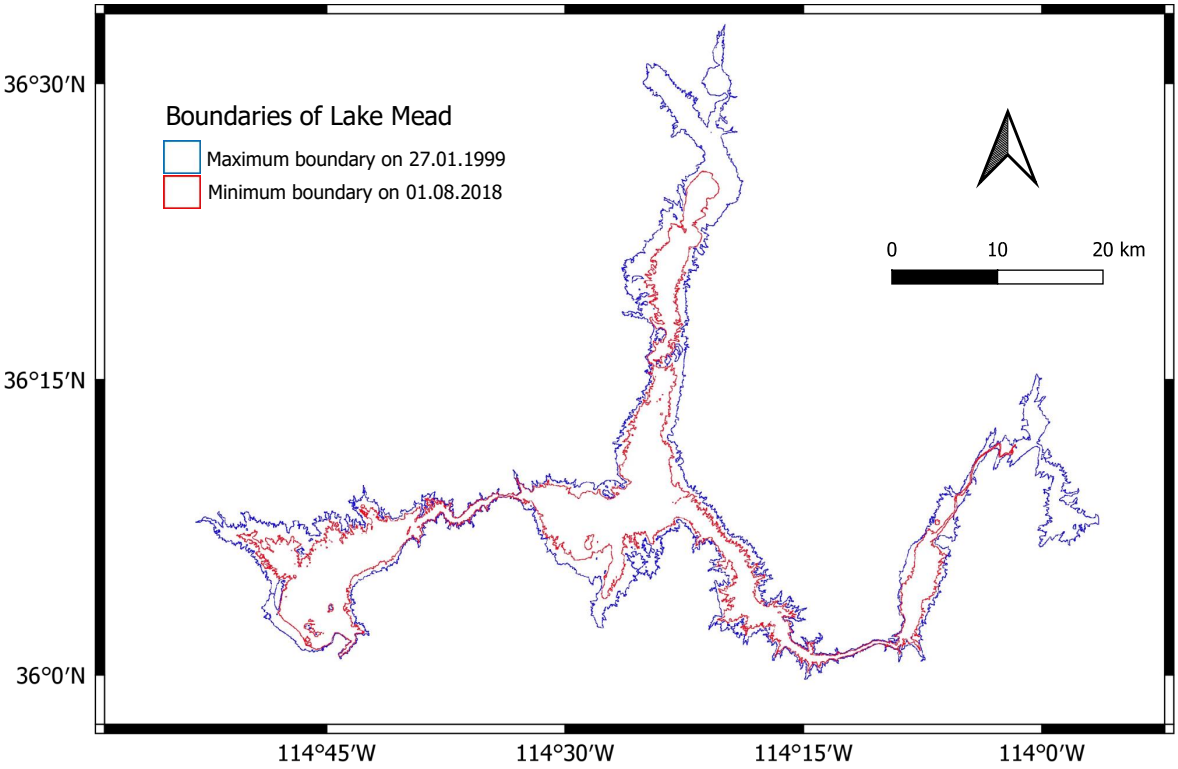

Figure 4.17: Comparison between the maximum lake boundary and the minimum lake boundary.

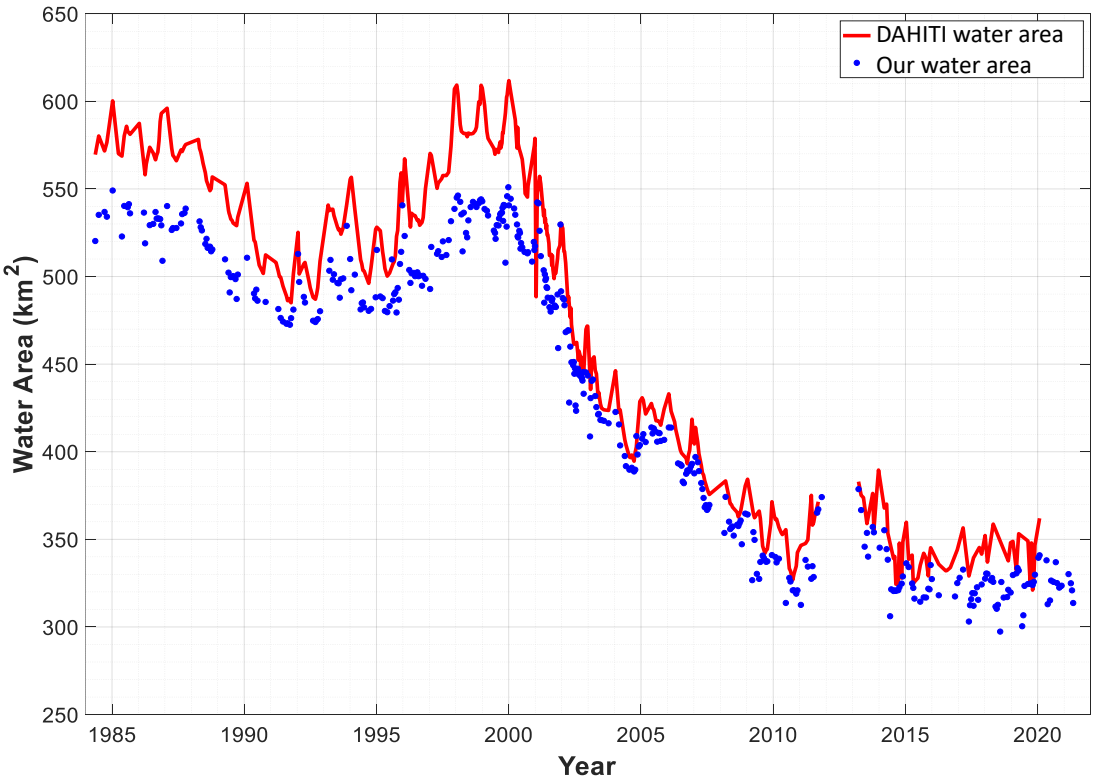

Figure 4.18: Comparison between our estimated water areas and DAHITI data set.

Nevertheless, we can make the *in-situ* water level as the reference, i.e. DAHITI water area and our water area can be comparable with *in-situ* water level. In Figure 4.19, we can see the agreement for DAHITI is better than ours, with $R^2 = 0.980$ and $\rho = 0.990$. The RMS relative difference between our water area and DAHITI water area from 1984 to 2000 is 9.1%. On the other side, if we consider the water levels are estimated depending on our water area classification method, the results presented in Figure 4.16 serve to demonstrate the robustness of our method in accurately classifying water areas, at least in regions where ICESat-2 laser tracks passed. However, the areas between the two data sets after 2001 exhibit a high degree of similarity. The difference between the two data sets after 2001 can be up to approximately 20 km^2, with a RMS relative difference of 4.6%.

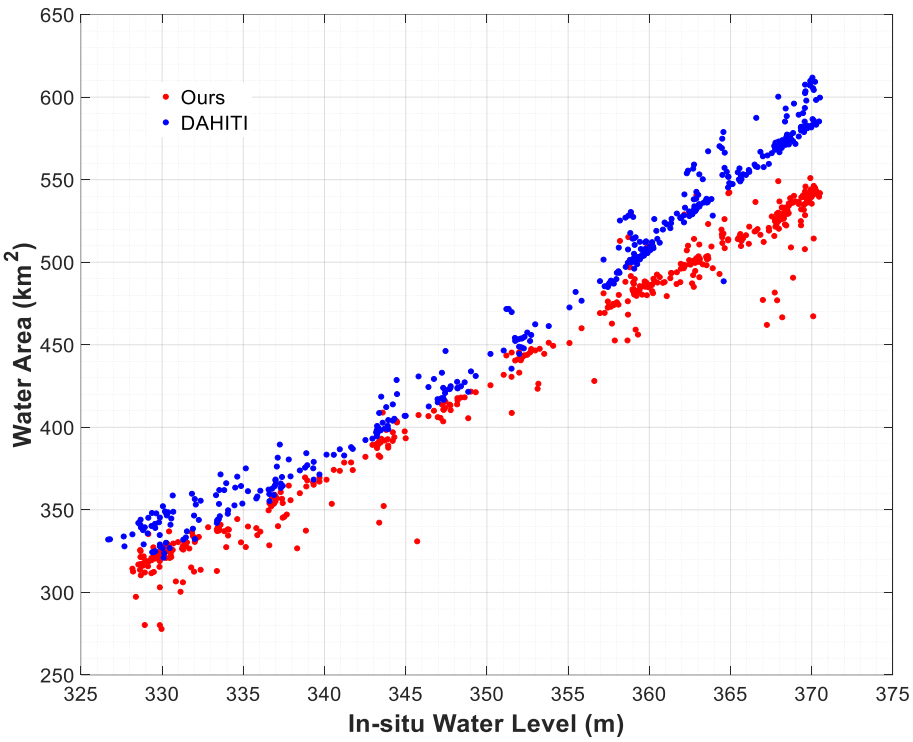

Figure 4.19: Compare our water area and DAHITI water area with *in-situ* water level.

As our method was employed to estimate the time series of both water level and water area, we are now able to establish the connection between these two variables using the LS method. Specifically, we employ linear, quadratic polynomial, and cubic polynomial functions to establish these relationships, which are shown in Figure 4.20. The linear function is $y = 5.371x - 1452$, the quadratic polynomial function is $y = 0.01623x^2 - 5.954x + 520.2$, and the cubic polynomial function is $y =$

$-0.001178x^3 + 1.878x^2 - 655.1x + 75890$, with y the water area (km^2) and x the water level (m). All three functions show good agreements, with the R^2 of 0.975, 0.976 and 0.977 respectively.

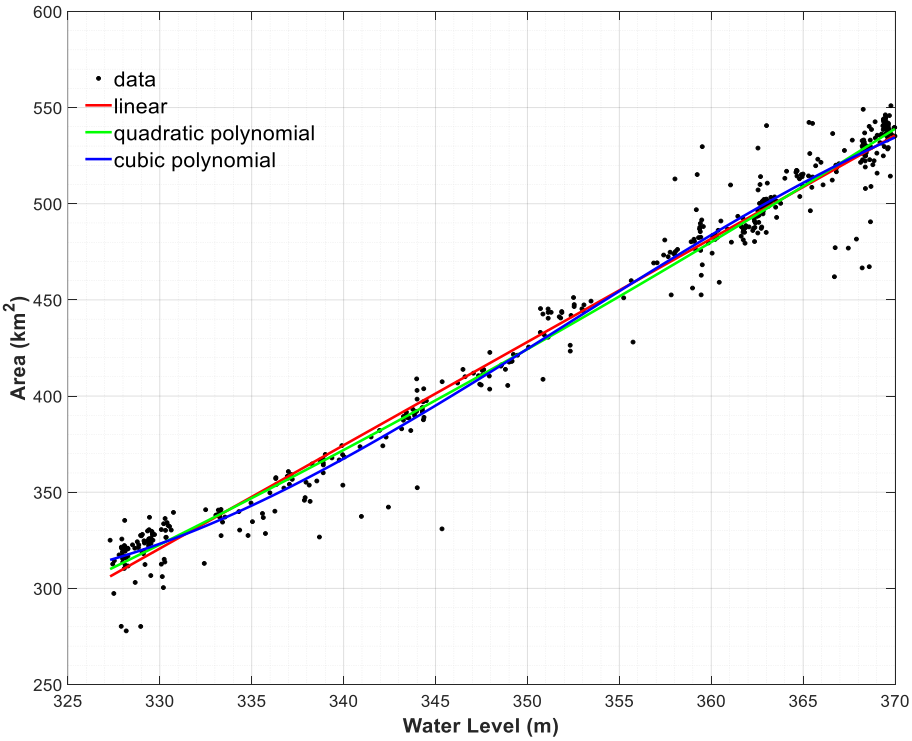

Figure 4.20: The relationships between the estimated water levels and water areas.

4.5.3 Estimated water volumes comparison with *in-situ* data

Based on the lake boundaries extracted from Landsat images, the corresponding water levels are estimated. The water volume of each image acquisition date can be calculated by the method in Subsection 4.4.3. The estimated water volumes using our water areas from 1984 to 2021 are compared with *in-situ* water volumes in Figure 4.21 (the estimated water volumes are labeled by blue points and the *in-situ* water volumes are labeled by a red curve). The average volume difference is 0.70 km^3, and the RMSE of the estimated water volumes is 0.62 km^3. ρ and R^2 between our results and *in-situ* water volumes are 0.996 and 0.991, respectively. The analysis reveals that the differences between the two data sets are comparatively smaller prior to 2003, with a RMSE of 0.47 km^3, in contrast to those after 2003, with a RMSE of 0.71 km^3. As the reference absolute water volume is chosen at the starting time of the time range, the error tends

to accumulate as time progresses.

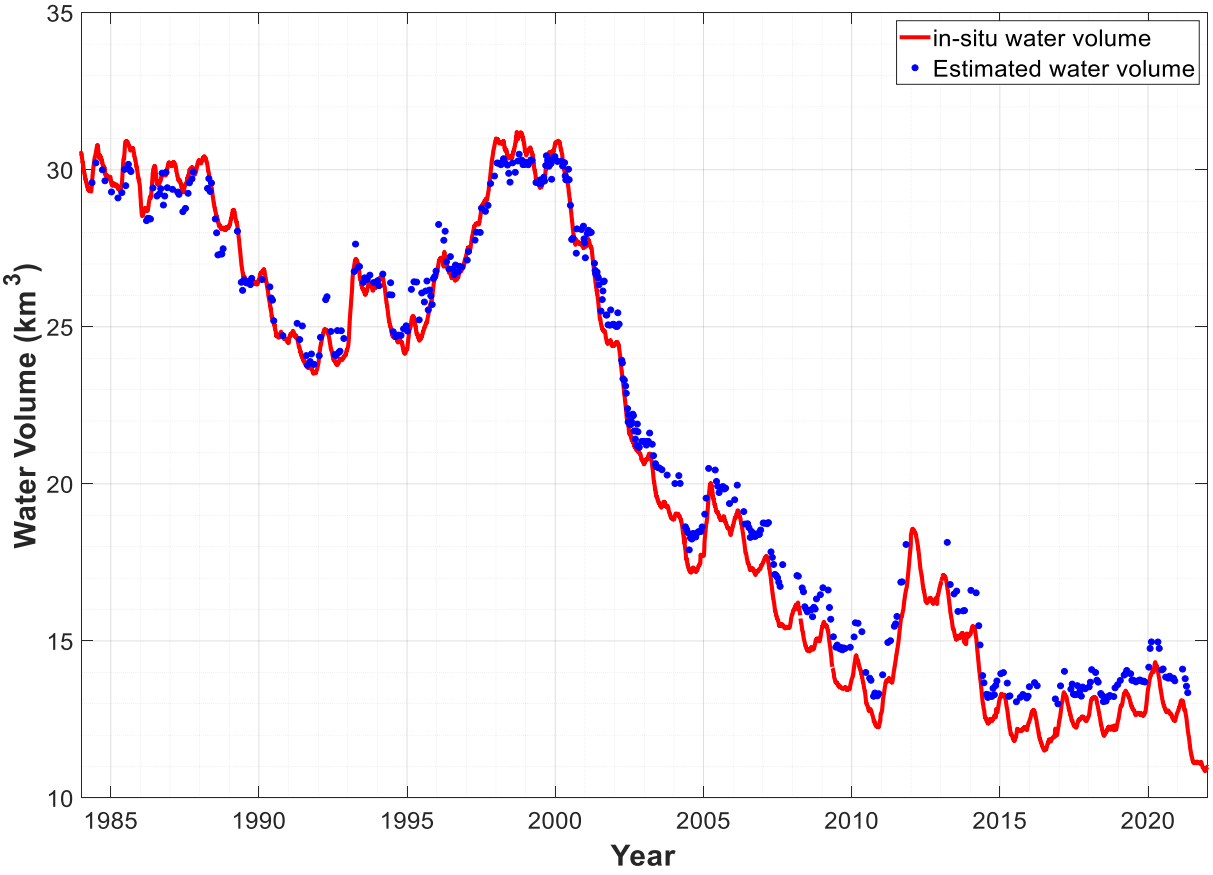

Figure 4.21: Comparison between the estimated water volumes using our estimated water areas and *in-situ* water volumes.

Similarly, we can also estimate the water volumes using DAHITI water areas, and compare them with *in-situ* volumes, as shown in Figure 4.22. The average volume difference is 0.70 km^3, and the RMSE of the estimated water volumes is 0.48 km^3. ρ and R^2 between the estimated and *in-situ* water volumes are 0.996 and 0.991, respectively. The bias between the estimated water volumes using DAHITI water areas and the *in-situ* volumes appears to be smaller than when using our water areas.

Since then, we have three data sets for water volumes: estimated using our water levels and areas, estimated using our water levels and DAHITI areas, and *in-situ*. Over the whole period, water volume change rates are calculated to be -0.55 km^3/year, -0.60 km^3/year and -0.59 km^3/year, respectively. While the overall trend for Lake Mead's water volume is decreasing, it's important to note that the trends in different time spans do not consistently exhibit a decrease. We've also computed the trends over

varying time intervals, as shown in Table 4.6.

Table 4.6: Water volume trends comparison between 3 data sets [km^3/year]

Time Spans	ours	DAHITI	*in-situ*
1984–1991	−0.83	−0.85	−0.95
1992–1999	0.76	0.73	0.91
2000–2010	−1.37	−1.39	−1.45
2011	4.89	5.01	4.59
2013–2021	−0.16	−0.14	−0.16

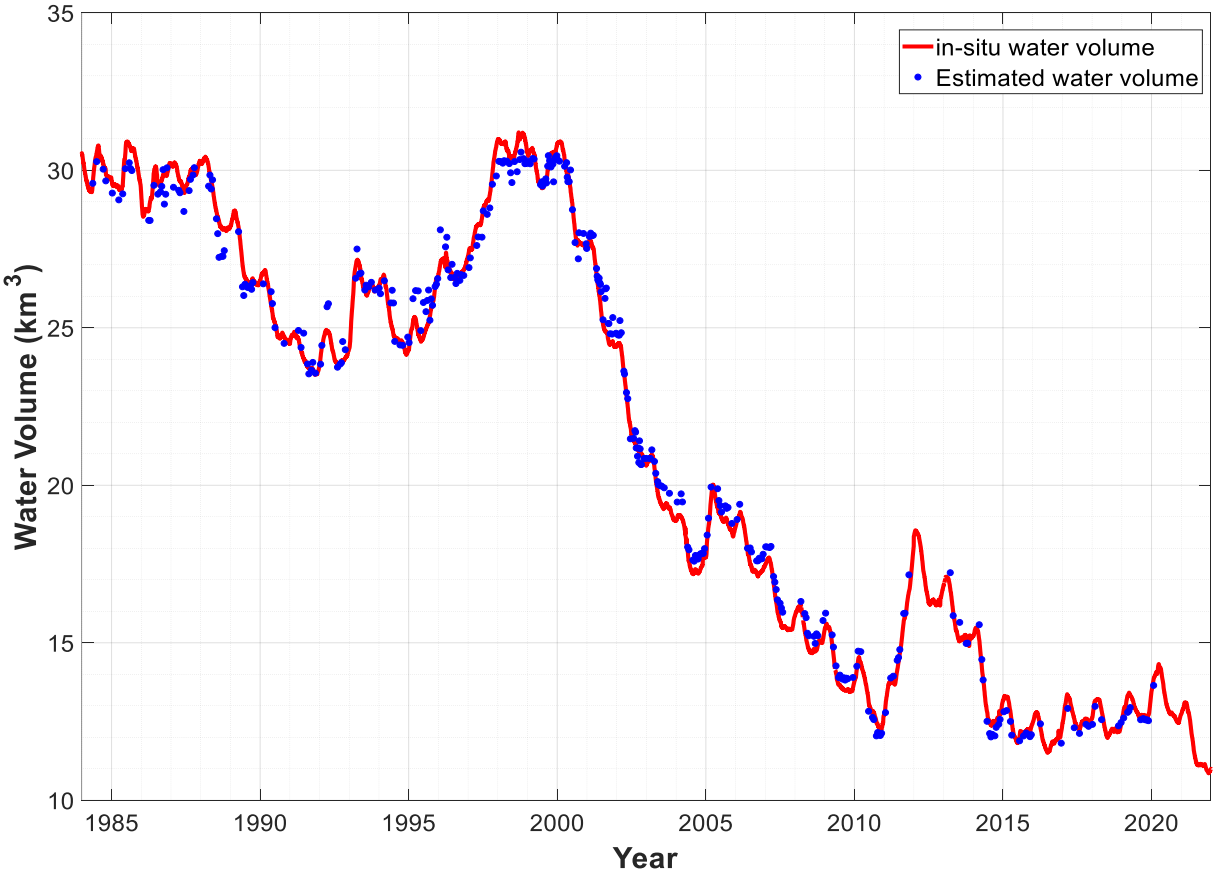

Figure 4.22: Comparison between the estimated water volumes using DAHITI water areas and *in-situ* water volumes.

If we use the linear relationship between water level and area, it will suggest a corresponding quadratic relationship between water level and volume. The relationship between the estimated water level and our water area-based volume is shown in Figure 4.23. Figure 4.24 shows the relationship between the estimated water level and

DAHITI water area-based volume. Both relationships show a good agreement with the quadratic model. R^2 values for both relationships are 0.975, consistent with the corresponding values obtained for the relationship between water level and area.

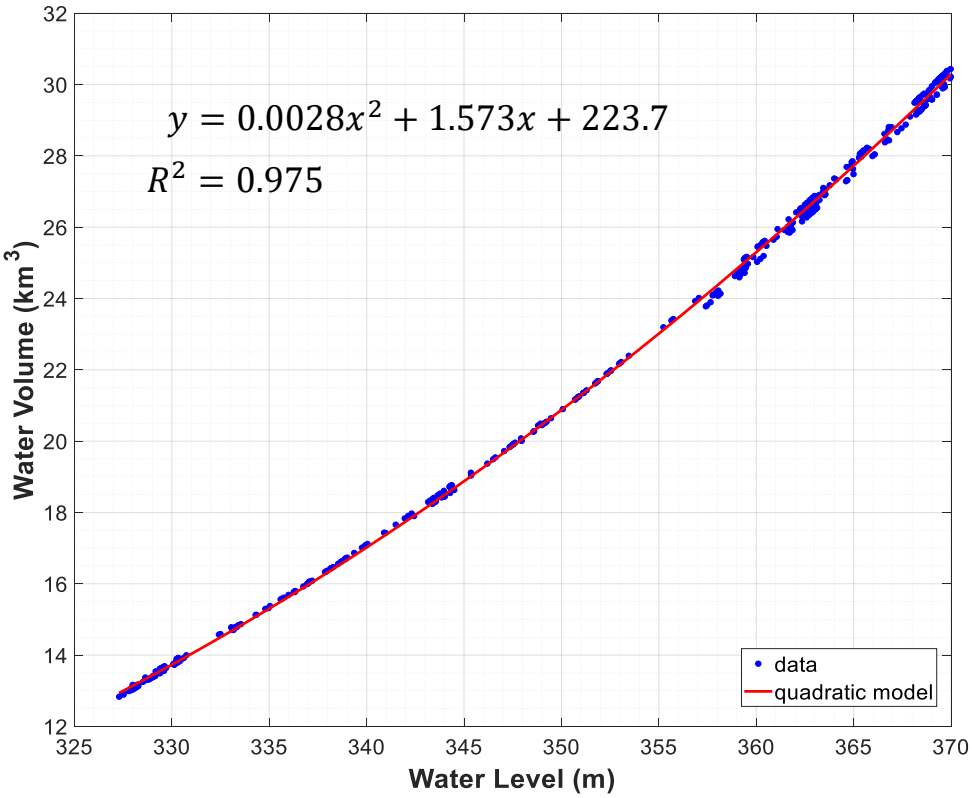

Figure 4.23: The linear relationship between the estimated water levels and water volumes using our water areas. The quadratic function is $y = 0.0028x^2 + 1.573x + 223.7$, with y the water volume (km^3) and x the water level (m).

Till now, both the Elevation–Area and Elevation–Volume relationships have been established, with Figure 4.20 and Figure 4.23 indicating that the resulting relationships for Lake Mead are highly robust, as reflected by the R^2 values of 0.975. Given the established Elevation–Area relationship and Elevation–Volume relationship, obtaining one accurate parameter allows for the estimation of the remaining two parameters accurately. Since only nearshore bathymetry is derived, the estimation of the other two parameters could potentially be substantially less accurate in the event of extreme droughts and floods. While the Elevation–Area and Elevation–Volume relationships may not always predict any two parameters of three, they can be adopted within a certain elevation range from 325 m to 370 m or area range from 250 km^2 to 550 km^2 or volume range from 12 km^3 to 31 km^3.

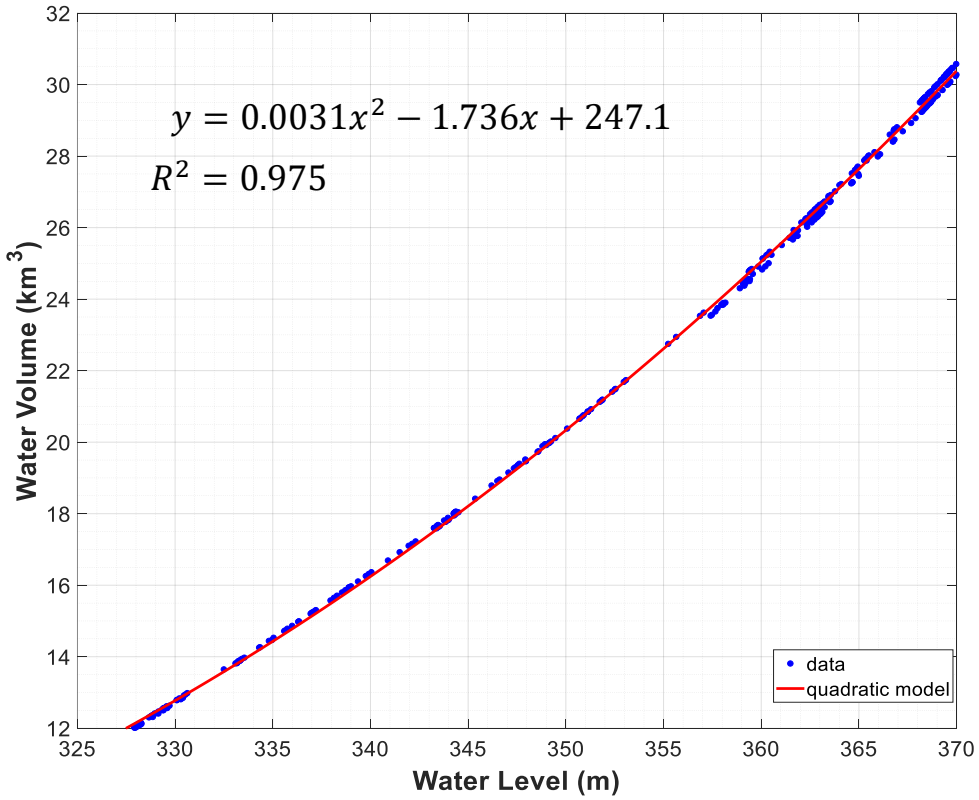

Figure 4.24: The linear relationship between the estimated water levels and water volumes using DAHITI water areas. The quadratic function is $y = 0.0031x^2 - 1.736x + 247.1$, with y the water volume (km^3) and x the water level (m).

4.6 Discussions

4.6.1 Performance of ICESat-2 data

As described in Subsection 4.5.1, the RMSE of water levels obtained directly from ICESat-2 is 4.7 cm, compared to the *in-situ* data. While various errors above the water surface, such as atmospheric delay, solid tide, and systematic pointing bias have been addressed, the bathymetric errors resulting from the refraction effect are not corrected for underwater lake floor measurements in ATL03 data. In Subsection 4.4.1, Snell's Law was employed to adjust the vertical errors. As illustrated in Figure 4.16, some water levels from 2015 to 2018 are estimated using the corrected lake floor profiles. These water levels are well in accordance with the *in-situ* water levels, which can prove that the bathymetry results from ICESat-2 are reliable. However, the inclination angle may be altered by water surface waves, leading to errors during refraction correction. Additionally, the horizontal correction has not been accounted for, which can also result in deviations in the actual position of the lake floor profile. The errors caused by these factors cannot be easily avoided. In general, ICESat-2 data demonstrate good performance.

4.6.2 Importance for establishing H–A and H–V relationships

The establishment of H–A and H–V relationships of Lake Mead is of great importance in water resource management and planning. These relationships can provide a better understanding of the lake's hydrological characteristics and aid in the development of water management policies. Lake Mead is one of the largest reservoirs in the United States and is used for various purposes, including irrigation, drinking water, and hydropower generation. Therefore, accurate measurements of the lake's water level, area, and volume are critical for the effective management and planning of these resources.

The H–A relationship can be used to estimate the surface area of the lake at different water levels, which is crucial for various uses such as irrigation, municipal, and industrial purposes. Additionally, the H–V relationship can be used to estimate the volume of water stored in the lake at different water levels, which is essential for assessing water supply and demand, and for predicting water availability during droughts or floods.

Furthermore, the H–A and H–V relationships can also aid in predicting the lake's ecological response to changes in water levels. For example, changes in the water level can affect the lake's shoreline, vegetation, and habitats for aquatic species, which can impact the lake's ecosystem. Accurate H–A and H–V relationships are essential for monitoring changes in the lake's water level, area, and volume over time. This information can be used to identify potential environmental concerns, such as changes in the lake's ecosystem, and to inform decision-making processes related to water management and allocation.

Finally, the establishment of H–A and H–V relationships of Lake Mead can serve as a reference for other lakes and reservoirs in the region and worldwide. The methodologies used to establish these relationships can be replicated for other bodies of water, which is essential for accurate water management and conservation efforts globally.

4.6.3 Error analysis

Although the correlation coefficient and R^2 indicate a strong agreement between our water level results and the *in-situ* data, with a value of 0.998, the RMSE for water level, which is 73 cm, is still relatively large. In this section, we will analyze the potential error resources that might affect the estimated results. First, the estimation of water levels in our study relies on the nearshore profiles from ICESat-2 laser altimetry and the water masks from Landsat imagery, making the accuracy of both factors crucial for the accuracy of the estimated water level. Figure 4.25 shows two nearshore profiles derived from a single ICESat-2 track. It is noticeable that the topography slope in the left figure is steeper compared to the right figure, and the underwater measurements in the right figure are more densely spaced than those in the left figure. In addition to the errors analyzed in Subsection 4.6.1, the classification errors of water masks should also be considered. Although we use cloud-free Landsat images, atmospheric conditions may vary in different places in one image, leading to intensity variations of each pixel for the Green and SWIR bands. The accuracy of the intersection position, which determines the water level, is also affected by the spatial resolution. If the nearshore topography slope is steep, the vertical height can vary significantly within a horizontal distance of 30 m.

Second, in this study, we assumed that the above-water and underwater topography near Lake Mead shore remained unchanged or changed only slightly during the period

1984–2021. However, it should be noted that small changes may still exist, and mismatches between the Landsat lake boundaries and the laser profiles could introduce errors in the estimated water levels. The laser points within 30 m of any of the intersections were selected to calculate the water level. The RANSAC algorithm was applied by assuming a linear slope within a distance of 60 m, which may not be small enough, and the topography slopes could vary within this distance, leading to potential errors in the estimated water levels. The bias between the estimated and *in-situ* water levels could be caused by the water surface slopes between the virtual stations and the *in-situ* station.

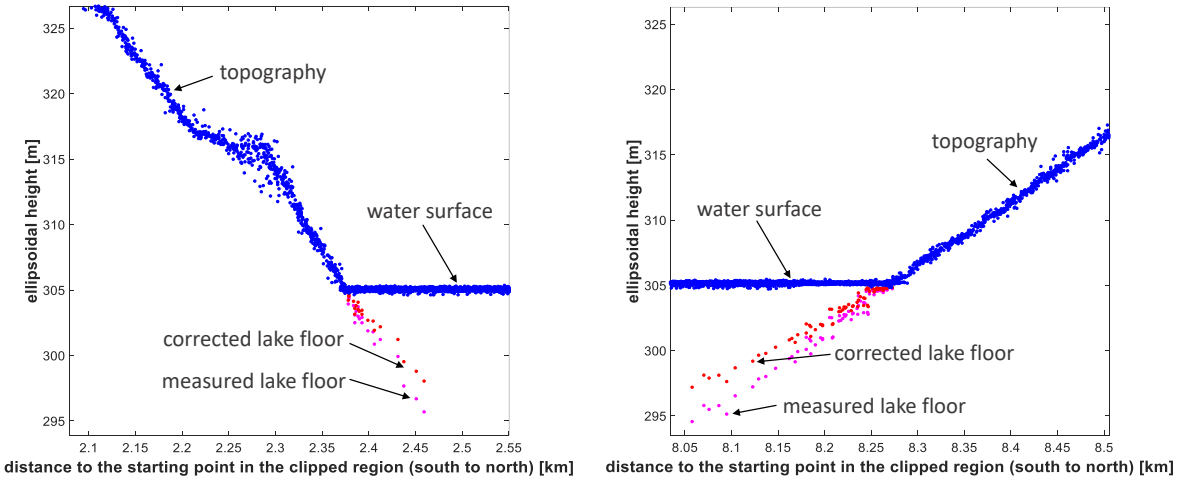

(a) Nearshore profile (b) Nearshore profile

Figure 4.25: Comparison of two nearshore profiles from a single track.

Third, the accuracy of estimating water volumes relies on the accuracy of corresponding water levels and water areas for each date. It is possible to obtain an accurate estimation of water levels even if the water area is classified with a large error. This is due to the significant variations in the slopes of nearshore topographies in different areas, leading to variations in classification accuracy. Hence, despite accurately estimating the corresponding water level, the estimated water volume may still contain a significant error.

Furthermore, it should be noted that this method has a limitation in case of extreme events, such as droughts or floods, as the actual water level may fall outside the range of extracted nearshore profiles.

4.6.4 Bathymetric map

Bathymetric maps are important because they provide valuable information about the depth, shape, and contours of the lake bottom. This information is essential for a variety of applications, such as:

1. Navigation and safety: Bathymetric maps allow boaters and other watercraft users to navigate the lake safely by identifying shallow areas, underwater hazards, and deep channels. This information can help prevent accidents and protect both human life and property.

2. Fisheries management: Bathymetric maps can be used to identify key habitats and fishing areas, allowing fisheries managers to develop effective management strategies for maintaining healthy fish populations.

3. Environmental monitoring: By mapping the lake bottom, scientists can better understand the lake's physical and biological processes, including sediment deposition, nutrient cycling, and habitat availability for aquatic organisms.

4. Water resource management: Bathymetric maps are important for managing water resources, including water quality monitoring, watershed management, and flood control.

5. Recreational activities: Bathymetric maps can also be used for recreational activities such as scuba diving, swimming, and other water sports, by identifying the best areas for these activities and ensuring user safety.

A global topographic map can be generated using SRTM DEM data, but the limitations of this method have been described in Section 4.1. Multiple datasets are available for obtaining global bathymetric maps, including GEBCO (General Bathymetric Chart of the Oceans) (Weatherall et al., 2015). However, the dataset is limited to ocean bathymetry and has a relatively low spatial resolution of 450 m. Our proposed method enables the generation of high-resolution nearshore profiles from ICESat-2 data and water occurrence percentiles (0%–100%) from Landsat imagery. The water occurrence percentile image indicates the frequency of water classification for each pixel by calculating the ratio of the time classified as water to the total observation time. This image can serve as a base map for bathymetry and provide information on slopes. The laser profiles are projected onto the occurrence percentile image, and each percentile value is associated with a specific elevation, which can be considered as a contour. The generated bathymetric map of Lake Mead is shown in Figure 4.26, which is an additional

product of our method. The elevation range is from 328 m to 370 m.

The Global Surface Water Explorer dataset (Pekel et al., 2016) offers a means of obtaining a global occurrence map for inland water bodies, which can be converted into a bathymetric map using the approach described in this chapter. Furthermore, the bathymetric map produced by this method has the potential to enhance the SRTM DEM by providing more accurate information on the elevation range and spatial resolution of bathymetry.

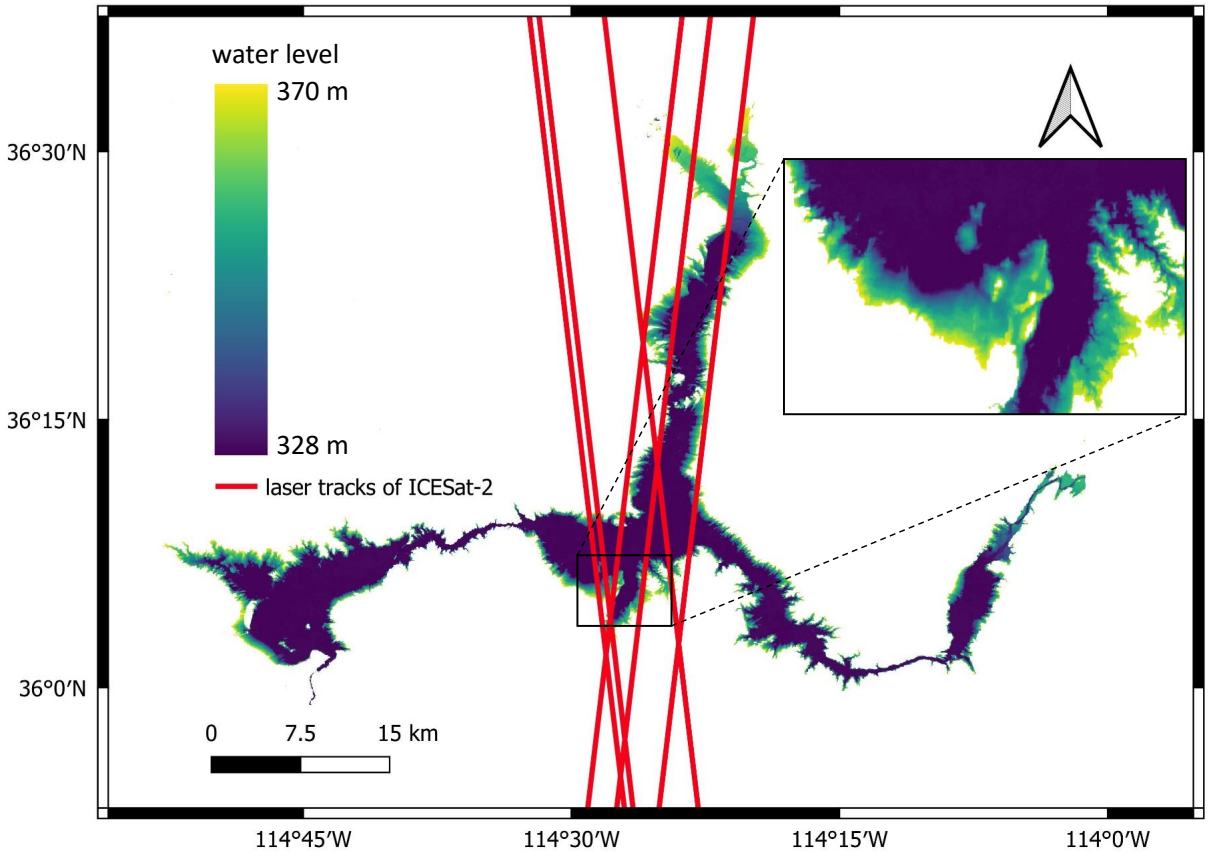

Figure 4.26: Generated nearshore bathymetric map of Lake Mead by our method.

4.6.5 Limitations

Using the available ICESat-2 ATL03 datasets in combination with our proposed method, it is potentially achievable to accurately monitor the long-term changes in water levels and volumes of lakes and reservoirs globally. It is important to note that this method has several limitations. Firstly, ICESat-2 bathymetric measurements are not feasible

when the water clarity is low. Secondly, in cases where lakes experience little to no significant water level changes over a long period, the precise linear regression between lake water levels and water areas may not be established. Moreover, the ICESat-2 laser altimetry can detect signal points reflected from underwater bottoms only up to a depth of approximately 10 m, which is dependent on the water's clarity. While this method offers an advantage in bathymetric data compared to its previous generation ICESat and radar altimetry, it cannot predict the water level if the water surface decreases more than 10 m.

4.7 Summary

A novel method has been introduced to evaluate temporal variations in water levels and volumes of lakes using solely remotely sensed data. First, the MNDWI thresholding method was employed to identify lake masks on various dates from Landsat imagery. Second, nearshore profiles including the ground and underwater bottom were extracted from ICESat-2 laser point data using a combination of DBSCAN, RANSAC, and refraction correction algorithms. Third, the water levels were calculated from the elevations of the intersections, the coordinates of which were obtained by projecting the nearshore profiles onto the lake masks. Subsequently, the water volume of each date was calculated based on the estimated water levels and water areas.

For this study, Lake Mead as a case study was analyzed. ICESat-2 laser altimetry data of 6 days and Landsat imagery spanning from 1984 to 2021 were used to estimate the water levels, areas and volumes. the findings revealed that this approach aligns well with the *in-situ* measurements, with R^2 values of 0.998 and 0.975 for the water levels and water volumes, respectively, and RMSE values of 73 cm and 0.62 km^3 for water levels and water volumes, respectively.

The novel method proposed in this chapter offers several advantages over previous studies. Thanks to the smaller laser footprints (~17 m diameter) and the denser along-track point clouds (70 cm interval) captured by ICESat-2 laser altimetry, water levels can be estimated using just a few days' laser tracks, without being limited by the temporal resolution of altimetry data. In contrast, radar altimetry could not estimate inland water levels before 1992 with remotely sensed data alone. This study estimates water levels and volumes for a longer period, from 1984 to 2021. Moreover, ICESat-2

altimetry uses 532 nm green lasers that can penetrate the water surface, enabling measurements of the lake floor. This study calculates the water levels for recent years using underwater lake floor data (up to approximately 8 m in depth), which can help predict the precise loss of water volume if the water level drops by up to 8 m. The water occurrence percentile image, generated from Landsat imagery, serves as a base map of the bathymetry and allows for the conversion of occurrence maps to bathymetric maps. In addition, ICESat-2 together with Landsat series has the capability to monitor new lakes, shrinking lakes and expanding lakes. This method will be potentially applicable to monitor rivers for long-term periods.

However, there are limitations to this method. The accuracy of the estimated water levels is dependent on the quality of the ICESat-2 laser point data and Landsat imagery. Additionally, the method is only applicable to lakes with clear water, as the ICESat-2 laser altimetry signals are not able to penetrate turbid water. In addition, it will be difficult to establish precise relationships of H–A and H–V for lakes without significant water level changes, and it has the inability to predict water levels for water surfaces decreasing more than 10 meters.

The accuracy of water level estimation depends heavily on the accuracy of water mask classification, which is restricted by the 30-meter spatial resolution of Landsat imagery. If higher resolution images, such as Sentinel-2 imagery (20 m), are employed, the accuracy of the estimation can be improved accordingly. However, Sentinel-2 imagery was only obtainable after 2015, which is not suitable for long-term water area estimation.

All in all, the proposed method represents a promising approach for estimating water levels and volumes in lakes and reservoirs using only remotely sensed data, without the need for *in-situ* measurements. This method has the potential to improve our understanding of water resources and hydrological processes by providing a means to monitor and quantify changes over time. As such, this method may prove useful in informing policy and decision-making processes related to water resource management, including the allocation of water resources, the management of drought and flood events, and the protection of aquatic ecosystems.

Chapter 5

River surface slope determination from ICESat-2

5.1 Introduction

The river surface slope (RSS), defined as the change in elevation per unit distance along the channel, is a fundamental characteristic influencing the behavior and functioning of fluvial systems (Dunne et al., 1998; Lighthill and Whitham, 1955; Mertes et al., 1996). It represents the inclination or steepness of the water surface as it flows downstream. The RSS is primarily influenced by the underlying river channel's bed slope, which dictates the direction and velocity of water flow (He et al., 2018). In hydrologic applications, the RSS is a key parameter for estimating flow velocity and discharge (Manning, 1891). The flow velocity derived from RSS is essential for densifying spatial or temporal low-resolution water level measurements from non-repeating altimetry satellites (Tourian et al., 2016). Therefore, the RSS can be used to validate the water level obtained from any satellite altimetry at fixed locations. The RSS is also a significant indicator in determining the energy and momentum of the flowing water (Parsaie, 2016). The RSS influences the movement of sediment particles, erosion and deposition processes, as well as the formation and evolution of river features such as pools, riffles, and meanders (Hohensinner et al., 2018). Measuring and analyzing the RSS is essential for understanding the behavior and dynamics of river systems. It helps in predicting water flow patterns, flood propagation, and hydraulic conditions within the river channel. Accurate estimation of the RSS is crucial for various applications, including flood modeling, river engineering, water resource management, and ecological assessments (Yaseen et al., 2019).

There are several methods widely used to determine the RSS at local scales. Field surveying has long been a traditional method for estimating RSSs. It involves measuring the elevations of the river channel at specific locations using surveying equipment

such as gauge stations and differential GPS (DGPS). Field surveys provide accurate slope measurements but can be labor-intensive, time-consuming, and limited to specific locations. Due to the limited number of gauge stations along a river, the slopes of the entire river will not be capable. Even though the slope between two gauge stations can be estimated, the estimated slope may not be meaningful, especially for the long distance between the two stations. Additionally, for the global scale, the number of *in-situ* stations is declining as mentioned in Chapter 1, which makes the challenge to determine the RSSs using this traditional method. DGPS uses GPS receivers with improved accuracy to measure elevation differentials between points along the river channel (Altenau et al., 2017). It provides a faster and more flexible way to determine the slopes of the place of interest. It offers good accuracy, especially in open areas without significant vegetation or obstructions. However, DGPS may still require ground control points for calibration, and the accuracy can be affected by satellite coverage and atmospheric conditions. Nonetheless, they serve as a valuable reference for validating slope estimations derived from other methods (Knighton, 2014).

Remote sensing techniques, such as airborne LiDAR (Mandlburger et al., 2020) and radar (Jiang et al., 2020), coupled with the generation of DEMs, have revolutionized the estimation of RSS. High-resolution topographic data obtained through remote sensing can be used to derive DEMs representing the elevation of the river channel and its surroundings. Slope estimation can then be derived from the DEM by analyzing elevation changes over a given distance. Remote sensing methods offer wide coverage and data of RSS at various scales, but they require careful consideration of data processing techniques, resolution limitations, and accuracy assessment (Paz and Collischonn, 2007). Due to the considerable personnel and cost requirements associated with airborne LiDAR, its application to nationwide and global river systems is always costly and inefficient. As a result, it is not suitable for continuous monitoring of the RSS across the entire river network. DEM measurements of the SRTM are regularly used to derive RSS for the global scale (Cohen et al., 2018). However, because of its relatively large height error, RSS estimates from SRTM data are only appropriate on a large scale (LeFavour and Alsdorf, 2005). The problem is that RSS is a dynamic and spatially varying parameter that undergoes continuous changes over time. SRTM captured the global DEM only once, and the RSS observed during this time may not represent the respective average RSS.

Since satellite altimetry provides water levels regularly, by comparing altimetry data at different points along the river, the RSS can be estimated. However, the intersections

between altimetry ground tracks and rivers do not exhibit regular distribution patterns. This is attributed to scenarios where the ground track may not intersect the river when the river flows parallel to it, or in cases where the river meanders, resulting in multiple crossings within a short distance. Satellite altimetry is particularly useful for large rivers and allows for continuous monitoring the RSS variation over extended periods. However, it may have limitations in narrow or shallow rivers with limited satellite coverage, and accuracy can be influenced by factors such as river width, vegetation, and river stage variability (Fu and Cazenave, 2000). For low-resolution mode (LRM) altimeters, water surface elevations can be derived with a RMSE of a few decimeters if the river is wider than 200 m (Sulistioadi et al., 2015). Water surface elevations obtained from synthetic aperture radar (SAR) have been found to be applicable with comparable accuracy for rivers up to a width of 40 m, as demonstrated by the work of Halicki and Niedzielski (2022). Furthermore, more advanced techniques such as interferometric SAR (InSAR) and laser altimeters offer even better precision and applicability, allowing for accurate measurements in narrower river systems. Scherer et al. (2022) studied 815 reaches and found ICESat-2 can be used to estimate RSS with a median absolute error of 2.3 cm/km relative to gauge data.

In spite of the limitations and uncertainties involved, satellite radar altimetry is still widely employed for the estimation of RSS, primarily focused on the derivation of river discharge (Sichangi et al., 2016). In a research investigation encompassing two arctic rivers, Zakharova et al. (2020) employed InSAR and SAR data acquired from the CryoSat-2, SARAL, and Sentinel-3A missions. These datasets were used to construct a time-variable cubic spline function for modeling the longitudinal river profile. By employing this methodology, the researchers successfully estimated RSS at any given location and time along a 175 km segment of the Ob River. Nevertheless, synchronous observation for two virtual stations using multi-satellite is still a challenge that cannot be solved. Except for the water levels from satellite altimetry, hydraulic modeling is normally involved in simulating the flow of water in rivers to estimate RSSs (Bates and De Roo, 2000). These models consider the hydraulic characteristics of the river, such as water velocity, channel roughness, and bed slope. By simulating the flow behavior, the model can estimate the RSS. Hydraulic modeling provides a detailed analysis of flow patterns and sediment transport, aiding in understanding the complex interactions between water and sediment. However, it requires comprehensive data on river geometry, hydraulic parameters, and calibration, making it computationally intensive and reliant on accurate input data.

As introduced in Chapter 2, ICESat-2 measures the topography along the ground track of 3 parallel pairs of laser beams spaced 3.3 km apart. This increases the probability of simultaneous water surface elevation measurements at different locations within a river reach. In this study, we will introduce a novel approach that capitalizes on the unique measurement geometry of ICESat-2 to obtain instantaneous estimates of reach-scale RSS. This approach combines two methods, namely the across-track and along-track approaches. The along-track method involves fitting the RSS to all water surface elevations from each individual beam intersecting the river reach and projecting it onto the river's centerline. Additionally, the across-track method calculates the RSS by analyzing the simultaneous water surface elevations from ICESat-2's parallel beams that intersect a particular river reach. By combining these methods, a time-variable RSS is generated to maximize both temporal and spatial coverage. Moreover, an average reach-scale RSS is computed, aiming to derive the global average reach-scale RSS and its variability in future investigations.

5.2 Methodology

In this study, we will estimate two types of RSS: (a) along-track-based river slope using a single beam, and (b) across-track river slope between two points on the centerline from two beams. We also use the estimated slopes to generate the slope time series and the averaged RSSs along the river. Figure 5.1 shows the schematic of ICESat-2 tracks intersecting the river extent. The river boundaries are represented by the blue curves, while the ground tracks of the 6 beams are depicted by the green lines. The red segments of the ground tracks indicate the areas where observations are made over the water surface. The centerline of the river is denoted by the blue dashed curve, and the orange points represent the intersections between the centerline and the ground tracks. Each red segment is characterized by an angle formed between the ground track and the centerline, which determines the slope of the segment, referred to as the along-track slope (i.e. the slope of each red segment). When the water level observations of one red segment are projected onto the centerline, it allows for the derivation of the along-track based river slope. Each intersection (P_i) between the centerline and ground track has a water level value. By determining the distance between two intersections along the river's centerline, it becomes possible to estimate the across-track slope (e.g. the slope between P_1 and P_2). In the case depicted in Figure 5.1, it is observed that even a single beam, such as GT2L, can yield multiple intersections, as seen with the points of P_1 and

P_2, while GT2R results in intersections P_3 and P_4.

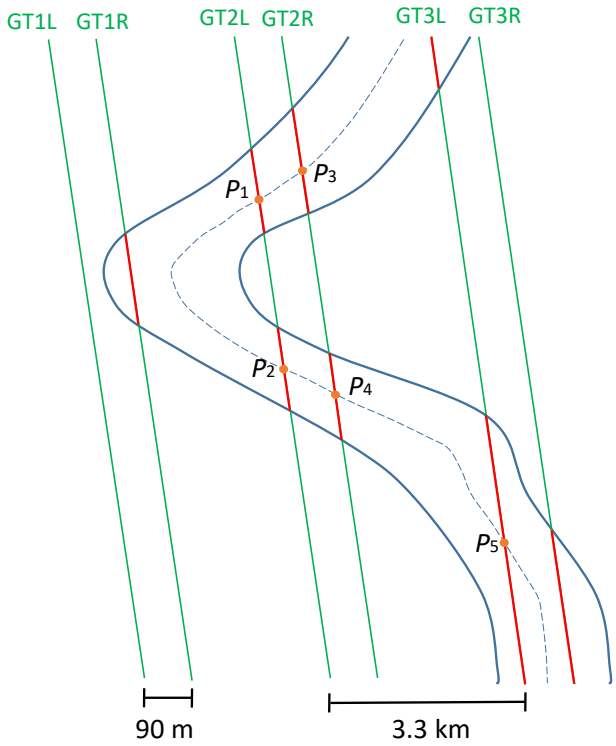

Figure 5.1: Schematic of ICESat-2 tracks intersecting the river extent.

5.2.1 Along-track based river slope estimation

ICESat-2 ATL13 measurements of each beam are situated exclusively on the water surface (Jasinski et al., 2021), serving as the basis for estimating the along-track based river slope. An angle exists between the ICESat-2 ground track and the river's centerline. When the angle measures 90°, denoting that the track is orthogonal to the centerline, it can be inferred that the water levels along the track persist as constant even though the water slope is detectable with the single photon LiDAR (Mandlburger et al., 2020), i.e. potential slopes across the flow direction are ignored. However, this is hardly ever the case. In cases where the ground track deviates from being perpendicular to the river centerline, even a short segment can lead to a surface slope, i.e. along-track based slopes are very local measurements of RSS. Therefore, projecting the ground track segment onto the river centerline allows us to represent the water levels of the river centerline by those observed along the ground track segment, as depicted in Figure 5.2.

By projecting the observations of a single beam onto the river centerline, we can determine the length of the segment along the centerline, starting from the first observation

and extending to the last one. Consequently, all the observations along the centerline can be referenced to the length measured from the first observation. Subsequently, the relationship between the length (l) and the water height (H) can be modeled using a linear regression equation of the form $H = al + b + e$, where a and b represent the parameters of the fitting line, and e denotes the residual vector. The fitting process for the linear regression can be carried out using the Gauss-Markov model of LS adjustment, as outlined below:

$$\underset{y}{\begin{pmatrix} H_1 \\ H_2 \\ \vdots \\ H_i \end{pmatrix}} = \underset{A}{\begin{pmatrix} l_1 & 1 \\ l_2 & 1 \\ \vdots & \vdots \\ l_i & 1 \end{pmatrix}} \underset{x}{\begin{pmatrix} a \\ b \end{pmatrix}} + \underset{e}{\begin{pmatrix} e_1 \\ e_2 \\ \vdots \\ e_i \end{pmatrix}}. \tag{5.1}$$

The slope of the fitting line a, which is also the slope of the river slope along the centerline for the segment, can be estimated by

$$\underset{2\times1}{\hat{x}} = (A^{\mathrm{T}} {Q_y}^{-1} A)^{-1} A^{\mathrm{T}} {Q_y}^{-1} y, \tag{5.2}$$

in which Q_y is the diagonal variance matrix of observations.
The precision of the estimated parameters $x = \binom{a}{b}$ can be calculated by the procedure:

$$\begin{aligned} \hat{e} &= y - A\hat{x} \\ \Longrightarrow {\hat{\sigma}_0}^2 &= \frac{\hat{e}^{\mathrm{T}} {Q_y}^{-1} \hat{e}}{m-n} \\ Q_{\hat{x}} &= (A^{\mathrm{T}} {Q_y}^{-1} A)^{-1} \\ \Longrightarrow \hat{Q}_{\hat{x}} &= {\hat{\sigma}_0}^2 Q_{\hat{x},} \end{aligned} \tag{5.3}$$

where m is the number of observations and n is the number of parameters (here n is 2). $\hat{Q}_{\hat{x}}$ is variance-covariance matrix of vector x, which can be written as:

$$\hat{Q}_{\hat{x}} = \begin{bmatrix} {\sigma_a}^2 & \sigma_a \sigma_b \\ \sigma_a \sigma_b & {\sigma_b}^2 \end{bmatrix}. \tag{5.4}$$

σ_a is the precision of the parameter a, which is also the precision of the along-track based river slope.

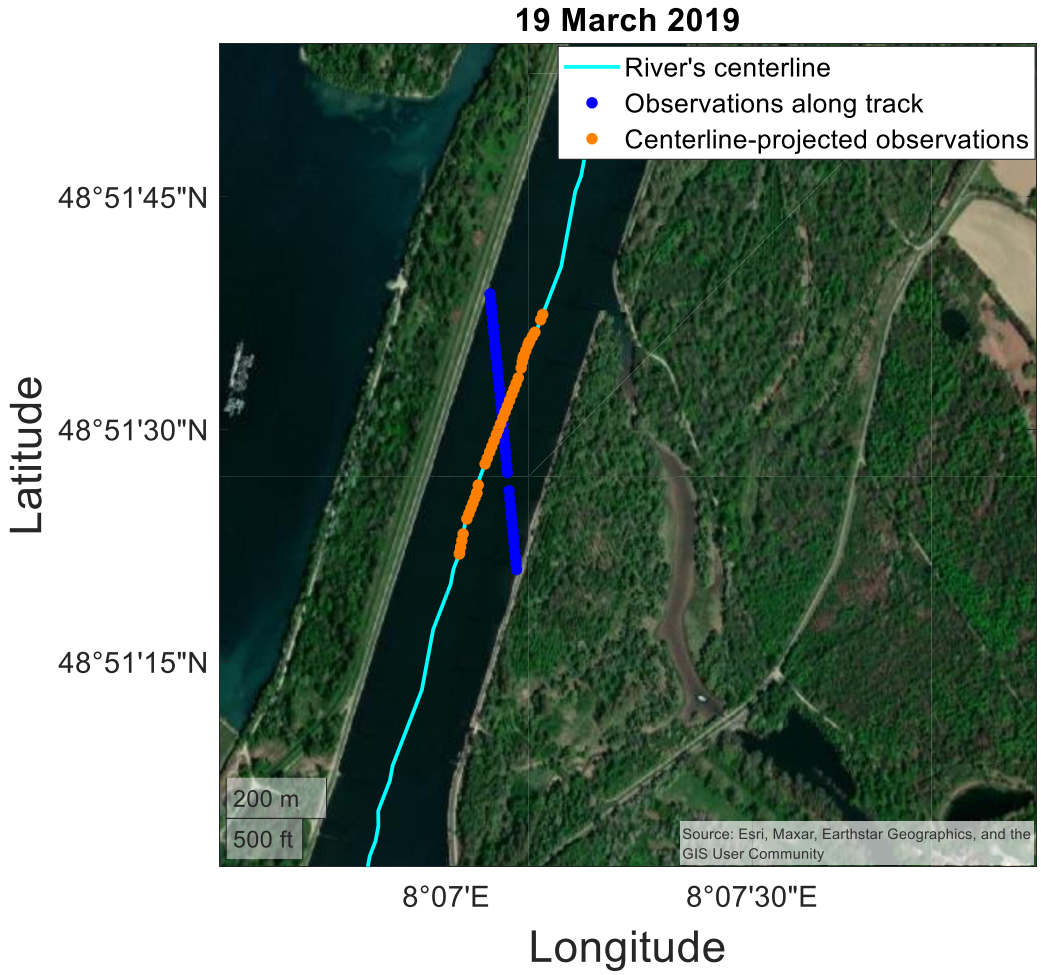

Figure 5.2: Schematic of observation of one beam projected onto the river's centerline.

5.2.2 Across-track river slope estimation

Once the fitting line for a specific beam has been estimated using the aforementioned procedure, the water height (H) at the intersection point between the ground track and the river centerline can be determined using the linear function. Similarly, the water heights at the intersection points of two different beams, denoted as H_1 and H_2, can be estimated using the same method. The river length (l) between two strong or two weak beams can be computed using the SWORD centerline of the river, see Figure 5.3. Subsequently, the across-track river slope (S) between the beams can be calculated using the following formula:

$$S = \frac{H_1 - H_2}{l}. \tag{5.5}$$

The estimation of the precision of H at the intersection point, can be determined using the following formula:

$$\sigma_H = \sqrt{\frac{\hat{e}^{\mathrm{T}}\hat{e}}{m}}, \tag{5.6}$$

where m is the number of observations from one beam. According to the error propagation, the precision of across-track river slope can be estimated by:

$$\sigma_{\mathrm{slope}} = \frac{\sqrt{\sigma_{H_1}^2 + \sigma_{H_2}^2}}{l}. \tag{5.7}$$

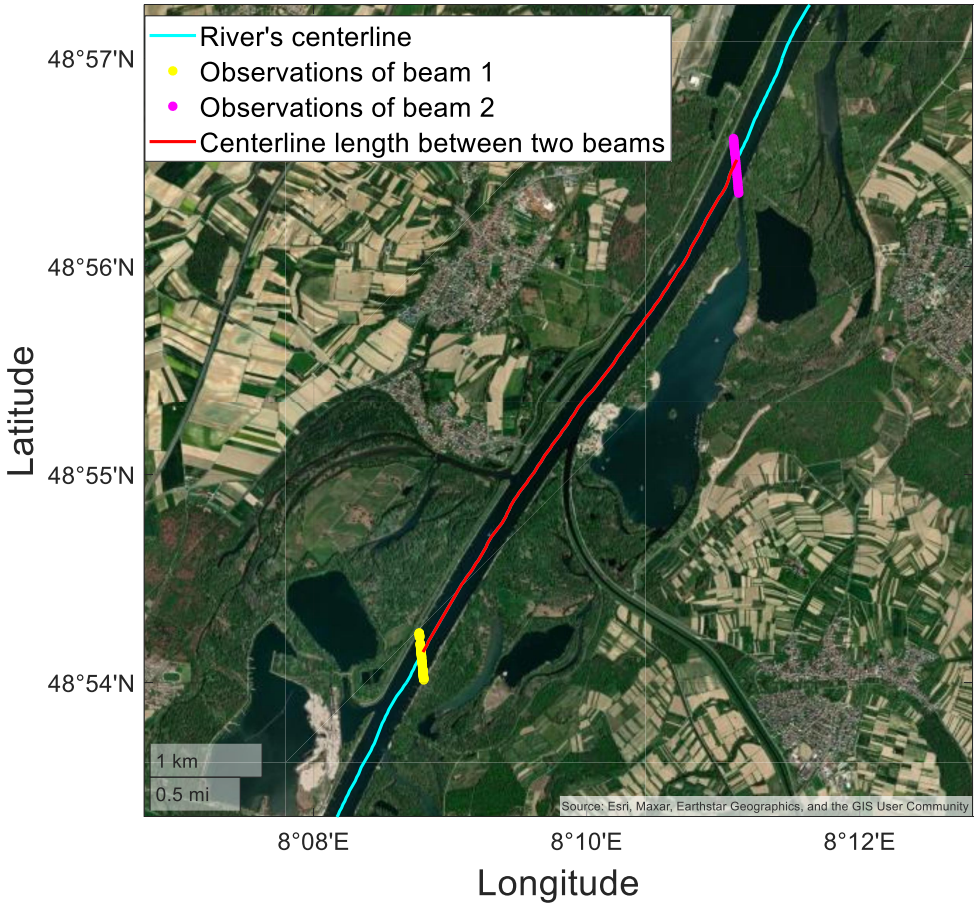

Figure 5.3: Schematic of the across-track river slope estimation. Yellow and pink points are observations of two beams of one reference ground track pass and the red polyline is the centerline between two intersection points.

5.3 Study area and data

5.3.1 Study area

For the purpose of this study, we select the Rhine River within Germany as our study case. The selected study area begins at Lake Constance (German: Bodensee) and extends until the border with the Netherlands. The Rhine River is the second longest river in Central and Western Europe (after the Danube), at about 1230 km with an average discharge of about 2900 m^3/s. River width varies between 50 m and 750 m (Frings et al., 2019). The selected part of the Rhine River is shown in Figure 5.4, which is highlighted in dark blue. There are dams, weirs, riffles and confluences along the river. Therefore, it includes diverse reaches, so that the RSSs in different conditions can be analyzed.

5.3.2 ICESat-2 ATL13 inland water surface height product

The main dataset used in this study consists of water surface elevation measurements obtained from ICESat-2. These ATL13 measurements were derived from the ATL03 Level 2 data provided as locations and orthometric heights, as described in the paper of Jasinski et al. (2021). Unlike radar altimetry, lidar sensors are unable to penetrate through clouds, resulting in missing observations during overcast conditions. However, due to the ability of green laser beams to penetrate water, the sensor can detect a maximum of 2.9 photons per meter over inland waters, depending on the water and atmospheric conditions (Jasinski et al., 2021). In the ATL13 product, dense photon-level observations are not included. Instead, representative values are provided for short segments comprising 75–100 consecutive received photons above inland water bodies. The length of these segments along the track can vary from 30 to several hundred meters, depending on the number of signal photons received per pulse.

5.3.3 SWOT river database

In order to determine the river reach distance and the angle at the ICESat-2 ground track intersecting a river, we employ the river centerlines from SWOT River Database (SWORD) (Altenau et al., 2021). The primary data source used in the SWORD project is the Global River Widths from Landsat (GRWL) database (Allen and Pavelsky, 2018). GRWL offers high-resolution centerline locations (30 m) for rivers worldwide that are

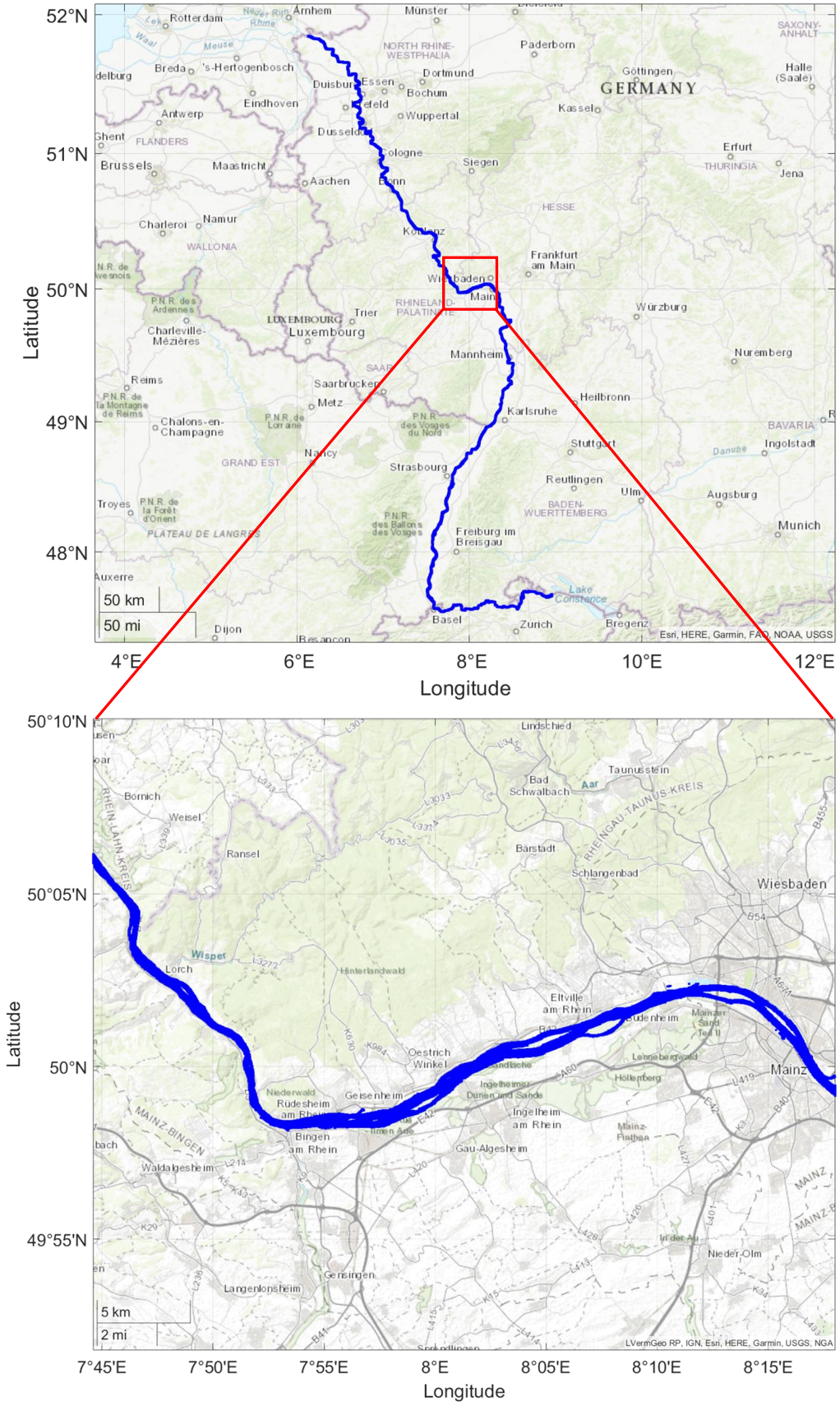

Figure 5.4: Location of Rhine River, used as the study case in this thesis.

30 m wide or wider. Along with the centerline locations, SWORD also provides corresponding attributes such as channel width, number of channels, and water body type for each location. SWORD was developed by processing Landsat imagery at approximately mean annual flow, generating and refining river masks, and subsequently generating centerlines along the final river masks. Detailed information regarding cross-sectional width and the number of observed channels is available for each centerline point in the GRWL database. In addition, in the SWORD dataset, we incorporate consistent RSS data for each river reach. These data serve as a reference point for comparing our results. The RSS values in SWORD are estimated by applying linear regression to elevation data obtained from the Multi-Error-Removed Improved-Terrain (MERIT) Hydro dataset (Yamazaki et al., 2019). The MERIT Hydro dataset is derived from the MERIT DEM, which combines remote sensing data from SRTM and the Advanced Land Observing Satellite (ALOS). The MERIT DEM undergoes preprocessing to remove noise, correct height errors, and mitigate tree canopy biases, as outlined by Yamazaki et al. (2017). Moreover, the SWORD dataset also includes the width of each river reach at mean annual flow, which we employ to eliminate the other water bodies in the selected region.

5.3.4 Water occurrence map

The global surface water occurrence map in the Global Surface Water Explorer (GSWE) (Pekel et al., 2016), is used as a filtering criterion for the ICESat-2 observations. The dataset combines multiple satellite observations, including optical and radar data, to classify the presence or absence of water in global surface water bodies from 1984 to 2021. It incorporates data from various satellite missions, such as Landsat, Sentinel-1, and Sentinel-2. The dataset undergoes extensive processing and analysis to produce the water occurrence map, which provides information on the spatial distribution of water bodies worldwide. The water occurrence percentage image shows how often each pixel is classified as water (0%–100%), which is calculated as the ratio of the time classified as water versus the total observation time. In order to ensure that the observations from ICESat-2 fall within the boundaries of the river extent, only pixels with a percentage of 85% or higher will be chosen.

5.4 Data processing

The preprocessing is to determine the effective ICESat-2 data over the river extent. To ensure that the ICESat-2 data exclusively covers the Rhine River and excludes surrounding water bodies, a preliminary step involves buffering the SWORD reach centerline by 1.5 times the width of the reach. Subsequently, any ICESat-2 data points falling outside the buffered region along each ground track are eliminated from the analysis. The remaining ICESat-2 data generally cover the Rhine River, although certain observations may extend beyond the river banks. The next step involves ensuring that only the ICESat-2 observations falling within the water extent are considered. To achieve this, we use the water occurrence map and exclude ICESat-2 observations that align with pixels where the water occurrence exceeds 85%. This filtering process helps remove observations that potentially occur over the river banks.

After these processes, there may be still some ICESat-2 outliers remaining. Statistical hypothesis tests are employed to determine the validity of an observation, distinguishing between erroneous and accurate data points. Among these tests, data snooping is a widely used approach, which incorporates the concept of reliability introduced to geodesy by Baarda (Baarda, 1967, 1968). Baarda's data snooping method operates under the assumption that at least one single outlier exists within the set of observations, which is provided in Appendix A. Consequently, a one-dimensional local hypothesis test is conducted on each observation to detect the presence of the outlier. The result after data snooping is shown in Figure 5.5. The along-track based river slope can be estimated by the method of Subsection 5.2.1. The fitting line of observations from one beam is shown in Figure 5.6. Once we've estimated the along-track based river slopes, we can then proceed to estimate the across-track river slopes using the approach detailed in Subsection 5.2.2.

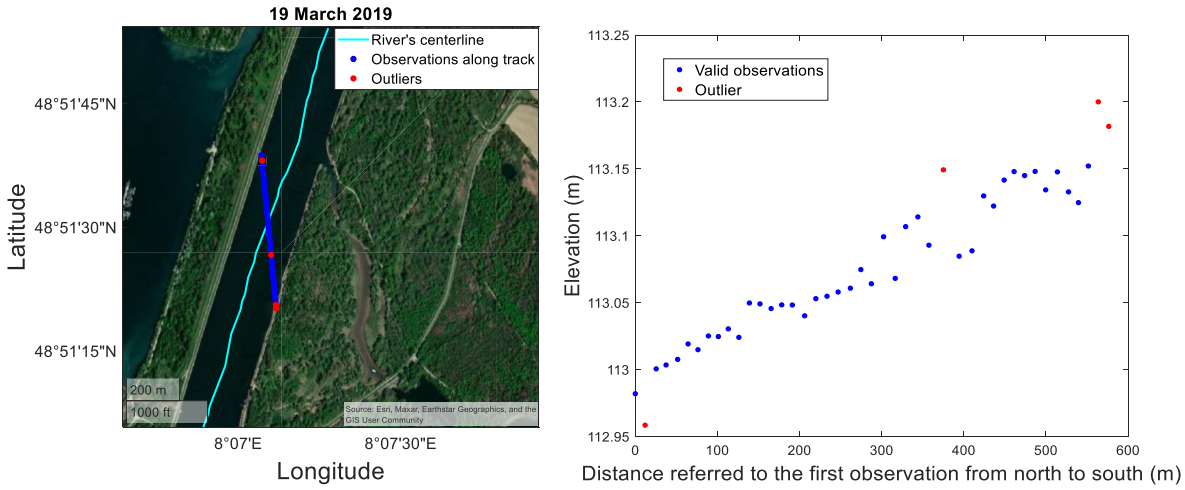

(a) ICESat-2 observations of one beam crossing the river's centerline.

(b) The elevation profile of the beam.

Figure 5.5: Performance of data snooping.

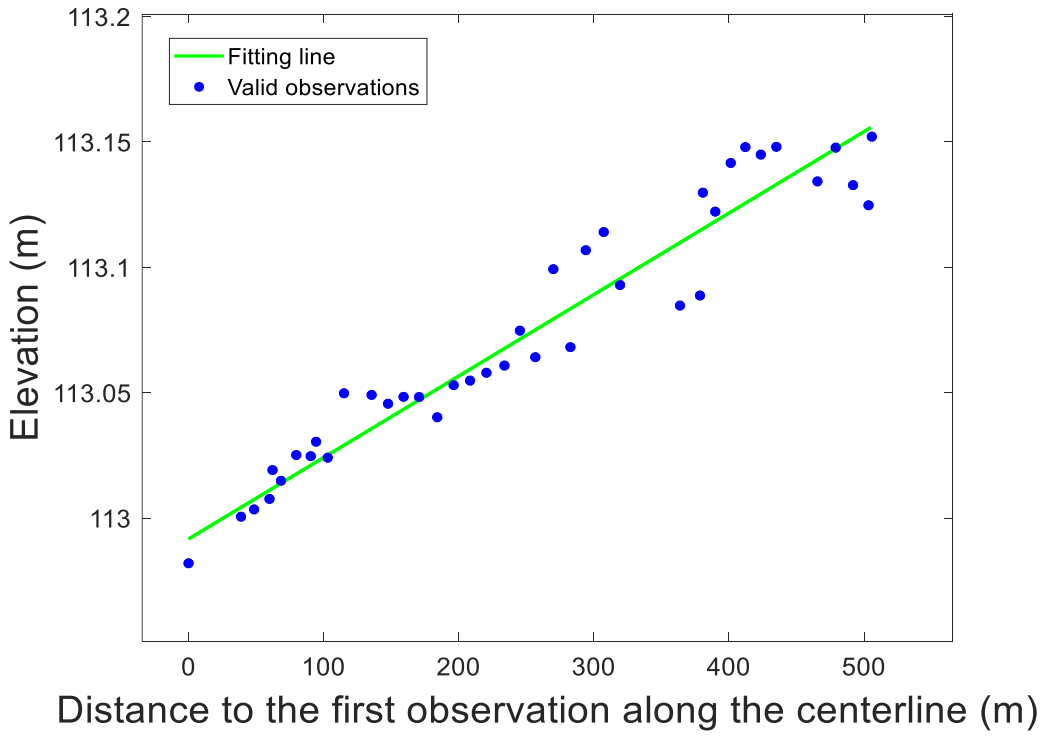

Figure 5.6: The fitting line of observations from one beam.

5.5 Results and discussion

Due to the operational off-nadir pointing of ICESat-2 over land areas for enhanced topographic measurements, the ground tracks of repeat cycles do not remain in the same positions. To ensure denser coverage of the entire river, 4 years' worth of data are used. The SWORD river reaches, defined every 10 km, allow for averaging the water levels on the centerline obtained from the along-track data over four years within one reach, representing the water level of that reach. Then the height profile of the river can be derived. This approach yields a robust estimate of the chainage slope, provided that the water level time series is long enough to capture the entire distribution. Figure 5.7 shows the averaged water levels along the river with a spatial resolution of 10 km using 4 years' ICESat-2 data. The orthometric height of the river varies within a range of approximately 390 m to 10 m. Observably, the slopes of the upstream region are steeper compared to those of the downstream region. This observation aligns with the topography, as the Rhine River flows from mountainous areas to plain areas.

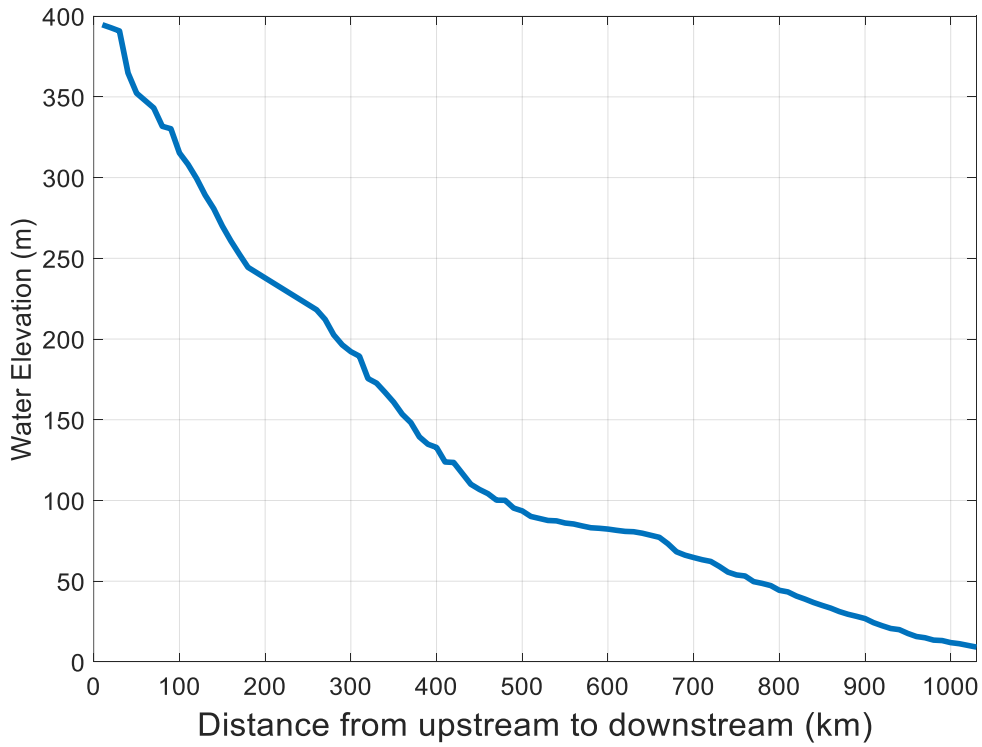

Figure 5.7: Average water elevation of each reach along the Rhine River.

5.5.1 Along-track based river slope validation against ground measurements

Validating along-track based river slopes for the entire river is challenging due to limited ground data availability. However, some local water resource management offices conduct measurements of certain river reaches using traditional methods, either for research purposes or shipping activities. In our study, we acquired water level measurements along a small-scale section near the city of Mainz. These measurements were obtained using ship-mounted GNSS equipment, provided by the Waterways and Shipping Office Upper Rhine (German: Wasserstraßen- und Schifffahrtsamt Oberrhein). Consequently, in this particular region, a comparison can be made between the along-track based river slopes estimated by ICESat-2 and the local data collected by the ship-based measurements. Figure 5.8 shows an example of the ship-based measurements along a river reach.

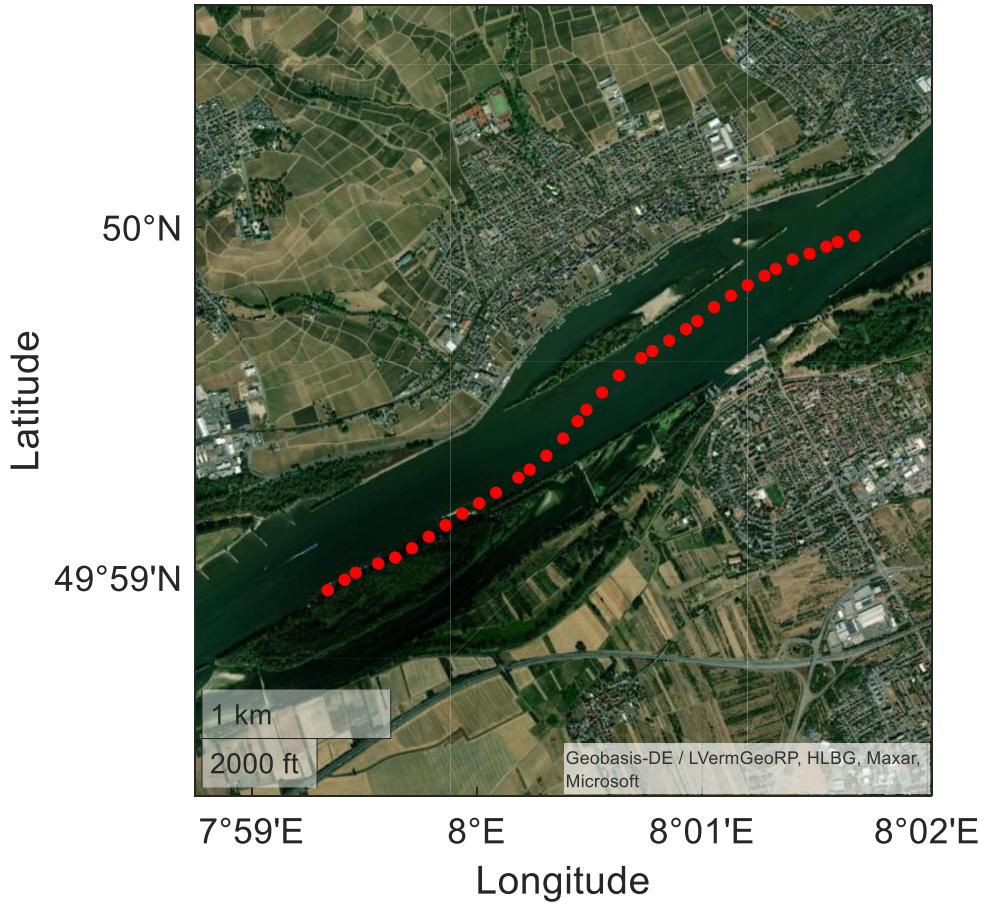

Figure 5.8: Ship-based height measurements along the river reach.

Overlapping data between ship-based measurements and ICESat-2 measurements are

available for four different months. We make the assumption that the river slope remains relatively stable within each month. Consequently, the along-track slope obtained from ICESat-2 during a specific month can be reasonably compared to the ship-based measurements taken during that same month. Figure 5.9 shows the water elevation comparison between ICESat-2 and ship-based measurements in four months. The observed height differences between the two datasets likely stem from disparities in geodetic datum systems and acquisition dates employed therein. The slopes of the two datasets can be calculated by the method of Subsection 5.2.1 respectively. Slope differences between ICESat-2 along-track data and ship-based data for the four months: 9.2 cm/km, 0.1 cm/km, 3.6 cm/km, and 2.2 cm/km respectively. The average slope difference across the four months is calculated to be 3.8 cm/km. This comparison shows that the ICESat-2 along-track data is in reasonably good agreement with the ship-based measurements, supporting the accuracy and reliability of ICESat-2's measurements for assessing river slopes.

5.5.2 Cross-validation of across-track river slopes

We do not expect the slope between two gauge stations will reflect small-scale RSS, because the distance between two neighboring gauge stations is much larger than the length of a reach. However, when calculating the across-track slope using two strong beams, e.g. the slope between P_2 and P_5 in Figure 5.1, the two weak beams will also generate one across-track slope. As a result, the across-track slope can be compared between both strong and weak beams. The across-track slopes from strong beams within each reach over four years are averaged, providing a representative value for the across-track slope of that reach. This process is similarly applied to the weak beams, obtaining the chainage slopes for both strong and weak beams. Figure 5.10 shows the chainage slope of the river derived from strong and weak beams. The color bar indicates that the slopes of upstream reaches are steeper compared to those of downstream reaches. In Figure 5.10(b), there is a data gap between 49°N and 50°N, resulting from the lack of available data on weak beams in that region. Notably, the slope difference between strong and weak beams is relatively small in the downstream section, specifically from 49°N heading northwards, with a RMS of 3.2 cm/km. In the upstream section, specifically from 49°N heading southwards, the slope difference between strong and weak beams is more significant compared to the downstream part, with a RMS of 9.7 cm/km. Several factors may contribute to this difference, including substantial slope variations, the presence of dams, and potential obstructions such as wires in the upstream region. Figure 5.11 displays the average slope precision of each reach, indicating that the precision from both strong and weak beams is below 1 cm/km.

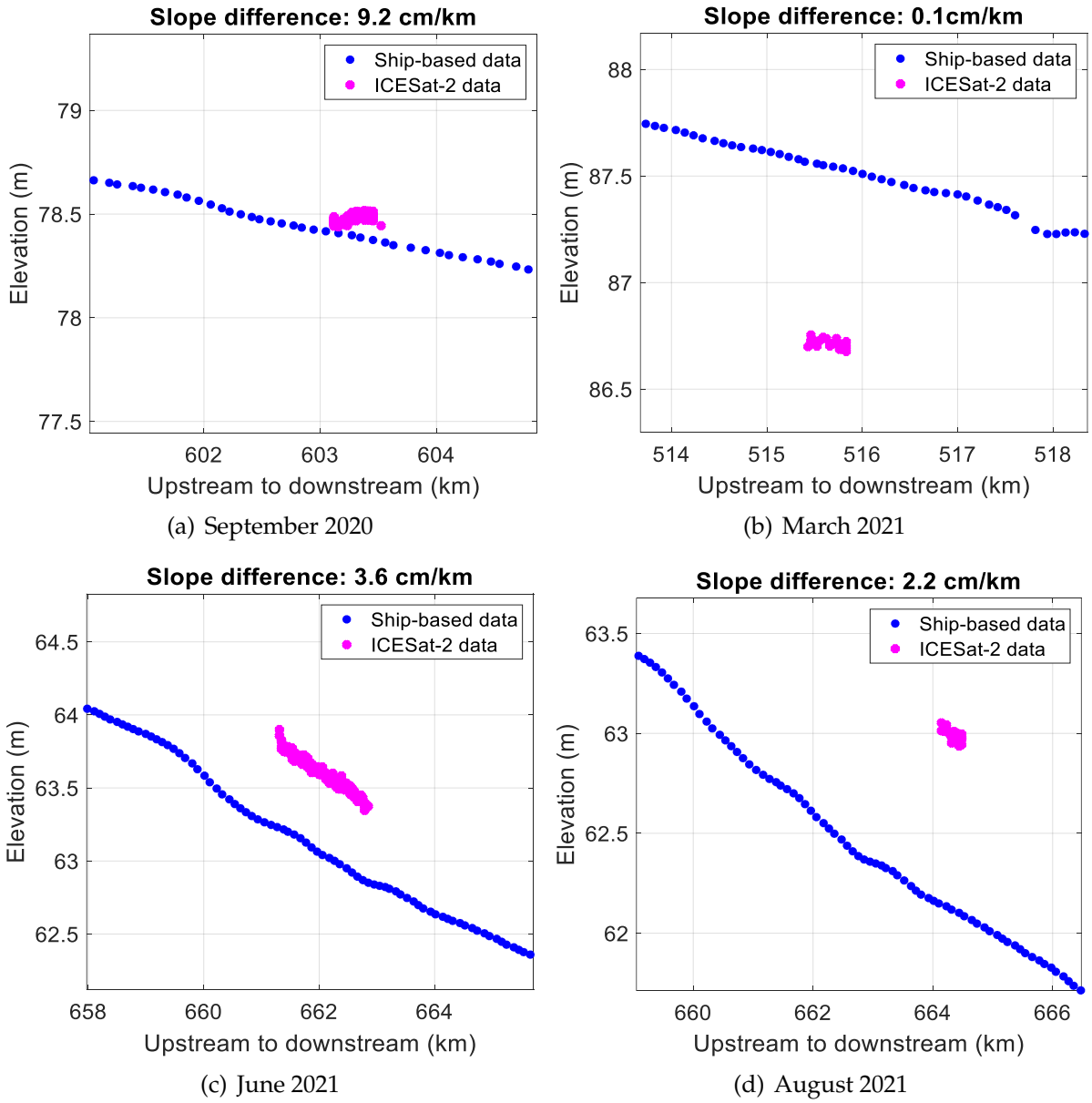

(a) September 2020 (b) March 2021

(c) June 2021 (d) August 2021

Figure 5.9: Water height comparison between ICESat-2 and ship-based measurements.

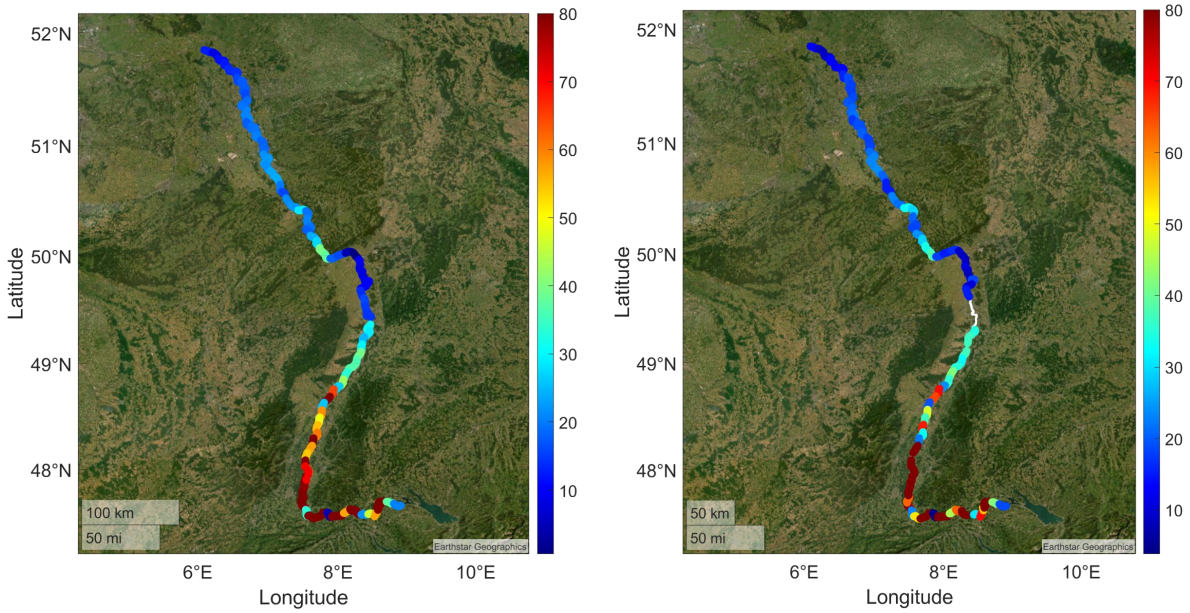

(a) Across-track slope of strong beams (cm/km) (b) Across-track slope of weak beams (cm/km)

Figure 5.10: Comparison of across-track slopes between strong and weak beams.

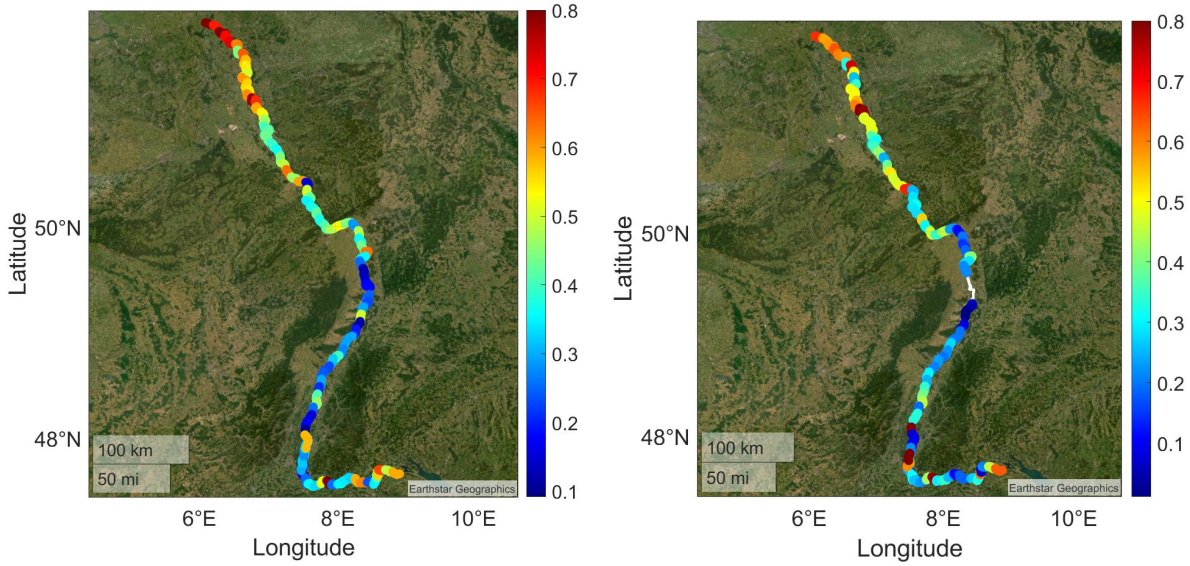

(a) Across-track slope precision of strong beams (cm/km) (b) Across-track slope precision of weak beams (cm/km)

Figure 5.11: Comparison of across-track slope precision between strong and weak beams.

5.6 Summary

In this chapter, we have successfully derived the RSS from ICESat-2 ATL13 observations at the reach scale. The difference between the along-track slope and the ship-based slope is expected to be on the order of several centimeters per kilometer. The results obtained through the across-track approach show an RMS difference between strong and weak beams of less than 10 cm/km for the Rhine River. RSS can serve as a significant correction for water level time series derived from radar satellite altimetry, especially when other errors, like the off-nadir effect, are not predominant.

To apply RSS as a correction, it is essential to unambiguously determine the crossing chainage of the satellite orbit. The SWOT mission is expected to provide RSS time series with higher temporal resolution compared to ICESat-2, as SWOT's revisit interval for a reach is about 11 days due to its 120 km swath width and 21-day repeat orbit (Biancamaria et al., 2016). Additionally, SWOT's Ka-band Radar Interferometer (KaRin) instrument can penetrate clouds, allowing for more data availability in regions with high cloud coverage. SWOT is explicitly designed to observe water surface slope, and its science requirements aim for a slope accuracy of 1.7 cm/km (Biancamaria et al., 2016), which is expected to surpass the mean along-track based river slopes of this study.

Chapter 6

Conclusions and outlook

6.1 Summary of findings

In this thesis, we explored the applications of the ICESat-2 in monitoring inland water bodies (lakes and rivers). The primary objectives are to assess the satellite's capability in measuring water level, river slope and lake volume variations, and to investigate its potential for various hydrological applications. Throughout the research, a combination of remote sensing techniques and data processing algorithms was employed to achieve these goals.

Firstly, through the application of the XO analysis method, the radial orbit error level of the ICESat-2 satellite was effectively determined. In this approach, Kepler's orbit model was used to represent the satellite's radial distance, and a linearization process involving three parameters was employed for the LS adjustment. Our findings reveal that, despite the advancements in satellite design, it remains challenging to completely eliminate orbit errors, resulting in an error magnitude of several centimeters. Consequently, there is a pressing need for further advancements in technology to minimize the radial orbit error and enhance the precision of satellite observations.

Secondly, this research demonstrated the impressive capabilities of ICESat-2 in accurately measuring water levels and volumes in lakes. By combining ICESat-2 data with Landsat images and validating the results with *in-situ* measurements, the relationship of water level, area and volume was established. This represents a significant advancement in using remote sensing technology to track changes in lakes, and it holds great potential for enhancing our understanding of water resources and ecosystems.

Furthermore, this research evaluated ICESat-2's ability to estimate river slopes using two different methods. The along-track river slope was compared with the ship-based measured slope, and the across-track river slope was cross-validated using strong and

weak beams. The results showed its potential in estimating river flow rates, which will be valuable for calculating river discharge.

These findings present a promising advancement in the field of remote sensing-based hydrology, with potential applications in regions lacking *in-situ* data. Additionally, the insights gained from this research contribute to our understanding of climate change impacts on freshwater bodies. By analyzing long-term data obtained from ICESat-2 data and Landsat imagery, we can discern patterns and trends in water level–area–volume changes, providing important information for climate scientists, water resource managers, and policymakers.

6.2 Limitations and future directions

While this study showed the applications of ICESat-2 in monitoring lakes and rivers, some limitations and challenges were encountered during the research process. One primary limitation is the satellite's temporal and spatial resolution, which may not be sufficient for capturing fine-scale hydrological processes. Future missions with improved resolution and more frequent observations could address this issue.

Additionally, ICESat-2's performance can be affected by cloud cover, particularly in regions with persistent cloud cover. Integrating data from other complementary satellite missions or employing data assimilation techniques could help overcome this limitation.

Moreover, according to Manning's equation (Manning, 1891), the river discharge can be estimated if we know the parameters in Eq. (6.1).

$$Q = \frac{1}{n} A^{\frac{5}{3}} W^{-\frac{2}{3}} \sqrt{S}, \tag{6.1}$$

where Q is the river discharge, n is Manning's roughness coefficient, A is the cross-section area of the river channel, W is the river width, and S is the RSS. The bathymetry measurement using ICESat-2 still relies on the quality of water and this is the main obstacle to the potential research on river discharge estimation. More extensive validation and calibration efforts are needed to improve the reliability of these estimates further. For future research, the following directions are recommended to enhance the applications of ICESat-2 in monitoring water bodies:

1. Investigate the integration of ICESat-2 data with other remote sensing technologies, such as SAR images and radar altimetry, to improve water level monitoring in regions with dense vegetation or complex terrain.

2. Explore the potential of ICESat-2 in studying the dynamics of glacial lakes, which are highly vulnerable to climate change-induced glacier retreat.

3. Collaborate with hydrological and climate modeling communities to assimilate ICESat-2 data into models, enhancing their accuracy and predictive capabilities.

4. Extend the study to different geographical regions and investigate the variability in ICESat-2 performance across diverse landscapes.

Bibliography

Abowarda, A. S., Bai, L., Zhang, C., Long, D., Li, X., Huang, Q., and Sun, Z. (2021). Generating surface soil moisture at 30 m spatial resolution using both data fusion and machine learning toward better water resources management at the field scale. *Remote Sensing of Environment*, 255:112301. DOI: 10.1016/j.rse.2021.112301.

Abshire, J. B., Sun, X., Riris, H., Sirota, J. M., McGarry, J. F., Palm, S., Yi, D., and Liiva, P. (2005). Geoscience Laser Altimeter System (GLAS) on the ICESat mission: on-orbit measurement performance. *Geophysical Research Letters*, 32(21). DOI: 10.1029/2005GL024028.

Allen, G. H. and Pavelsky, T. M. (2018). Global extent of rivers and streams. *Science*, 361(6402):585–588. DOI: 10.1126/science.aat0636.

Alsdorf, D. E., Rodríguez, E., and Lettenmaier, D. P. (2007). Measuring surface water from space. *Reviews of Geophysics*, 45(2). DOI: 10.1029/2006RG000197.

Altenau, E. H., Pavelsky, T. M., Durand, M. T., Yang, X., Frasson, R. P. d. M., and Bendezu, L. (2021). The Surface Water and Ocean Topography (SWOT) Mission River Database (SWORD): A global river network for satellite data products. *Water Resources Research*, 57(7):e2021WR030054. DOI: 10.1029/2021WR030054.

Altenau, E. H., Pavelsky, T. M., Moller, D., Lion, C., Pitcher, L. H., Allen, G. H., Bates, P. D., Calmant, S., Durand, M., and Smith, L. C. (2017). AirSWOT measurements of river water surface elevation and slope: Tanana River, AK. *Geophysical Research Letters*, 44(1):181–189. DOI: 10.1002/2016GL071577.

Altenau, E. H., Pavelsky, T. M., Moller, D., Pitcher, L. H., Bates, P. D., Durand, M. T., and Smith, L. C. (2019). Temporal variations in river water surface elevation and slope captured by AirSWOT. *Remote Sensing of Environment*, 224:304–316. DOI: 10.1016/j.rse.2019.02.002.

Baarda, W. (1967). *Statistical concepts in geodesy*. Netherlands Geodetic Commission, Publications on Geodesy, New Series 2, No. 4. Available online at: https://www.ncgeo.nl/downloads/08Baarda.pdf.

Baarda, W. (1968). *A testing procedure for use in geodetic networks*. Netherlands Geodetic Commission, Publications on Geodesy, New Series 2, No. 5.

Bao, L., Lu, Y., and Wang, Y. (2009). Improved retracking algorithm for oceanic altimeter waveforms. *Progress in Natural Science*, 19(2):195–203. DOI: 10.1016/j.pnsc.2008.06.017.

Barsugli, J. J., Nowak, K., Rajagopalan, B., Prairie, J. R., and Harding, B. (2009). Comment on "When will Lake Mead go dry?" by TP Barnett and DW Pierce. *Water Resources Research*, 45(9). DOI: 10.1029/2008WR007627.

Bates, P. D. and De Roo, A. (2000). A simple raster-based model for flood inundation simulation. *Journal of Hydrology*, 236(1-2):54–77. DOI: 10.1016/S0022-1694(00)00278-X.

Bertiger, W., Bar-Sever, Y. E., Christensen, E. J., Davis, E. S., Guinn, J. R., Haines, B. J., Ibanez-Meier, R. W., Jee, J. R., Lichten, S. M., Melbourne, W. G., Muellerschoen, R. J., Munson, T. N., Vigue, Y., Wu, S. C., Yunck, T. P., Schutz, B. E., Abusali, P. A. M., Rim, H. J., Watkins, M. M., and Willis, P. (1994). GPS precise tracking of TOPEX/POSEIDON: Results and implications. *Journal of Geophysical Research: Oceans*, 99(C12):24449–24464. DOI: 10.1029/94JC01171.

Biancamaria, S., Lettenmaier, D. P., and Pavelsky, T. M. (2016). The SWOT mission and its capabilities for land hydrology. *Surveys in Geophysics*, 37(2):307–337. DOI: 10.1007/s10712-015-9346-y.

Blair, J. B., Coyle, D., Bufton, J., and Harding, D. (1994). Optimization of an airborne laser altimeter for remote sensing of vegetation and tree canopies. In *Proceedings of IGARSS'94-1994 IEEE International Geoscience and Remote Sensing Symposium*, volume 2, pages 939–941. IEEE. DOI: 10.1109/IGARSS.1994.399307.

Bonnefond, P., Verron, J., Aublanc, J., Babu, K., Bergé-Nguyen, M., Cancet, M., Chaudhary, A., Crétaux, J.-F., Frappart, F., Haines, B. J., Laurain, O., Ollivier, A., Poisson, J.-C., Prandi, P., Sharma, R., Thibaut, P., and Watson, C. (2018). The benefits of the Ka-band as evidenced from the SARAL/AltiKa altimetric mission: Quality assessment and unique characteristics of AltiKa data. *Remote Sensing*, 10(1):83. DOI: 10.3390/rs10010083.

Bosch, W. (2004). Geodetic application of satellite altimetry. In *Satellite Altimetry for Geodesy, Geophysics and Oceanography: Proceedings of the International Workshop on Satellite Altimetry, a joint workshop of IAG Section III Special Study Group SSG3. 186*

and IAG Section II, September 8–13, 2002, Wuhan, China, pages 3–21. Springer. DOI: 10.1007/978-3-642-18861-9_1.

Bosch, W. (2007). Discrete crossover analysis. In *Dynamic Planet: Monitoring and Understanding a Dynamic Planet with Geodetic and Oceanographic Tools IAG Symposium Cairns, Australia 22–26 August, 2005*, pages 131–136. Springer. DOI: 10.1007/978-3-540-49350-1_21.

Bosch, W., Dettmering, D., and Schwatke, C. (2014). Multi-mission cross-calibration of satellite altimeters: Constructing a long-term data record for global and regional sea level change studies. *Remote Sensing*, 6(3):2255–2281. DOI: 10.3390/rs6032255.

Brown, A. E., Zhang, L., McMahon, T. A., Western, A. W., and Vertessy, R. A. (2005). A review of paired catchment studies for determining changes in water yield resulting from alterations in vegetation. *Journal of Hydrology*, 310(1-4):28–61. DOI: 10.1016/j.jhydrol.2004.12.010.

Brown, C. D. (2002). *Elements of spacecraft design*. American Institute of Aeronautics and Astronautics, Reston, Virginia. DOI: 10.2514/4.861796.

Busker, T., de Roo, A., Gelati, E., Schwatke, C., Adamovic, M., Bisselink, B., Pekel, J.-F., and Cottam, A. (2019). A global lake and reservoir volume analysis using a surface water dataset and satellite altimetry. *Hydrology and Earth System Sciences*, 23(2):669–690. DOI: 10.5194/hess-23-669-2019.

Cahalane, C., Magee, A., Monteys, X., Casal, G., Hanafin, J., and Harris, P. (2019). A comparison of Landsat 8, RapidEye and Pleiades products for improving empirical predictions of satellite-derived bathymetry. *Remote Sensing of Environment*, 233:111414. DOI: 10.1016/j.rse.2019.111414.

Cai, X., Feng, L., Hou, X., and Chen, X. (2016). Remote sensing of the water storage dynamics of large lakes and reservoirs in the Yangtze River Basin from 2000 to 2014. *Scientific Reports*, 6(1):36405. DOI: 10.1038/srep36405.

Calmant, S. and Seyler, F. (2006). Continental surface waters from satellite altimetry. *Comptes Rendus Geoscience*, 338(14-15):1113–1122. DOI: 10.1016/j.crte.2006.05.012.

Camps, A., Park, H., Pablos, M., Foti, G., Gommenginger, C. P., Liu, P.-W., and Judge, J. (2016). Sensitivity of GNSS-R spaceborne observations to soil moisture and vegetation. *IEEE Journal of Selected Topics in Applied Earth Observations and Remote Sensing*, 9(10):4730–4742. DOI: 10.1109/JSTARS.2016.2588467.

Chelton, D. B., Ries, J. C., Haines, B. J., Fu, L.-L., and Callahan, P. S. (2001). Satellite altimetry. In *International Geophysics*, volume 69, pages 1–131. Elsevier. DOI: 10.1016/S0074-6142(01)80146-7.

Cheney, R. E. and Marsh, J. G. (1981). Oceanic eddy variability measured by GEOS 3 altimeter crossover differences. *Eos, Transactions American Geophysical Union*, 62(45):737–752. DOI: 10.1029/EO062i045p00737.

Cheng, C.-T., Wang, W.-C., Xu, D.-M., and Chau, K. W. (2008). Optimizing hydropower reservoir operation using hybrid genetic algorithm and chaos. *Water Resources Management*, 22:895–909. DOI: 10.1007/s11269-007-9200-1.

Cohen, S., Wan, T., Islam, M. T., and Syvitski, J. (2018). Global river slope: A new geospatial dataset and global-scale analysis. *Journal of Hydrology*, 563:1057–1067. DOI: 10.1016/j.jhydrol.2018.06.066.

Cohen, S. C., Degnan, J. J., Bufton, J. L., Garvin, J. B., and Abshire, J. B. (1987). The geoscience laser altimetry/ranging system. *IEEE Transactions on Geoscience and Remote Sensing*, GE-25(5):581–592. DOI: 10.1109/TGRS.1987.289837.

Cook, C. and Bakker, K. (2012). Water security: Debating an emerging paradigm. *Global Environmental Change*, 22(1):94–102. DOI: 10.1016/j.gloenvcha.2011.10.011.

Crétaux, J.-F., Abarca-del Río, R., Berge-Nguyen, M., Arsen, A., Drolon, V., Clos, G., and Maisongrande, P. (2016). Lake volume monitoring from space. *Surveys in Geophysics*, 37(2):269–305. DOI: 10.1007/s10712-016-9362-6.

Crétaux, J.-F., Arsen, A., Calmant, S., Kouraev, A., Vuglinski, V., Bergé-Nguyen, M., Gennero, M.-C., Nino, F., Del Rio, R. A., Cazenave, A., and Maisongrande, P. (2011). SOLS: A lake database to monitor in the near real time water level and storage variations from remote sensing data. *Advances in Space Research*, 47(9):1497–1507. DOI: 10.1016/j.asr.2011.01.004.

Cui, C. and Lelgemann, D. (1993). On cross-over differences of the radial orbital perturbations as functions of force model parameters. In *Geodesy and Physics of the Earth*, pages 95–99. Springer. DOI: 10.1007/978-3-642-78149-0_25.

De Lannoy, G. J., Reichle, R. H., Arsenault, K. R., Houser, P. R., Kumar, S., Verhoest, N. E., and Pauwels, V. R. (2012). Multiscale assimilation of Advanced Microwave Scanning Radiometer–EOS snow water equivalent and Moderate Resolution Imaging Spectroradiometer snow cover fraction observations in northern Colorado. *Water Resources Research*, 48(1). DOI: 10.1029/2011WR010588.

Déry, S. J., Hernández-Henríquez, M. A., Burford, J. E., and Wood, E. F. (2009). Observational evidence of an intensifying hydrological cycle in northern Canada. *Geophysical Research Letters*, 36(13). DOI: 10.1029/2009GL038852.

Donlon, C., Berruti, B., Buongiorno, A., Ferreira, M.-H., Féménias, P., Frerick, J., Goryl, P., Klein, U., Laur, H., Mavrocordatos, C., Nieke, J., Rebhan, H., Seitz, B., Stroede, J., and Sciarra, R. (2012). The global monitoring for environment and security (GMES) Sentinel-3 mission. *Remote Sensing of Environment*, 120:37–57. DOI: 10.1016/j.rse.2011.07.024.

Douglas, B., Agreen, R., and Sandwell, D. (1984). Observing global ocean circulation with Seasat altimeter data. *Marine Geodesy*, 8(1-4):67–83. DOI: 10.1080/15210608409379498.

Dozier, J., Green, R. O., Nolin, A. W., and Painter, T. H. (2009). Interpretation of snow properties from imaging spectrometry. *Remote Sensing of Environment*, 113:S25–S37. DOI: 10.1016/j.rse.2007.07.029.

Duan, Z. and Bastiaanssen, W. (2013). Estimating water volume variations in lakes and reservoirs from four operational satellite altimetry databases and satellite imagery data. *Remote Sensing of Environment*, 134:403–416. DOI: 10.1016/j.rse.2013.03.010.

Dubayah, R., Blair, J. B., Goetz, S., Fatoyinbo, L., Hansen, M., Healey, S., Hofton, M., Hurtt, G., Kellner, J., Luthcke, S., Armston, J., Tang, H., Duncanson, L., Hancock, S., Jantz, P., Marselis, S., Patterson, P. L., Qi, W., and Silva, C. (2020). The Global Ecosystem Dynamics Investigation: High-resolution laser ranging of the Earth's forests and topography. *Science of Remote Sensing*, 1:100002. DOI: 10.1016/j.srs.2020.100002.

Dunne, T., Mertes, L. A., Meade, R. H., Richey, J. E., and Forsberg, B. R. (1998). Exchanges of sediment between the flood plain and channel of the Amazon River in Brazil. *Geological Society of America Bulletin*, 110(4):450–467. DOI: 10.1130/0016-7606(1998)110<0450:EOSBTF>2.3.CO;2.

Edalat, M. M. and Stephen, H. (2019). Socio-economic drought assessment in Lake Mead, USA, based on a multivariate standardized water-scarcity index. *Hydrological Sciences Journal*, 64(5):555–569. DOI: 10.1080/02626667.2019.1593988.

Elmi, O. (2019). *Dynamic water masks from optical satellite imagery*. PhD thesis, University of Stuttgart, Stuttgart, Germany. DOI: 10.18419/opus-10597.

Elmi, O. and Tourian, M. J. (2023). Retrieving time series of river water extent from global inland water data sets. *Journal of Hydrology*, 617:128880. DOI: 10.1016/j.jhydrol.2022.128880.

Ester, M., Kriegel, H.-P., Sander, J., and Xu, X. (1996). A density-based algorithm for discovering clusters in large spatial databases with noise. In *Proceedings of 2nd International Conference on Knowledge Discovery and Data Mining*, number 34, pages 226–231. Available online at https://dl.acm.org/doi/10.5555/3001460.3001507.

Fischler, M. A. and Bolles, R. C. (1981). Random sample consensus: a paradigm for model fitting with applications to image analysis and automated cartography. *Communications of the ACM*, 24(6):381–395. DOI: 10.1145/358669.358692.

Fisher, J. B., Tu, K. P., and Baldocchi, D. D. (2008). Global estimates of the land–atmosphere water flux based on monthly AVHRR and ISLSCP-II data, validated at 16 FLUXNET sites. *Remote Sensing of Environment*, 112(3):901–919. DOI: 10.1016/j.rse.2007.06.025.

Frappart, F., Papa, F., Güntner, A., Tomasella, J., Pfeffer, J., Ramillien, G., Emilio, T., Schietti, J., Seoane, L., da Silva Carvalho, J., Medeiros Moreira, D., Bonnet, M.-P., and Seyler, F. (2019). The spatio-temporal variability of groundwater storage in the Amazon River Basin. *Advances in Water Resources*, 124:41–52. DOI: 10.1016/j.advwatres.2018.12.005.

Frings, R., Hillebrand, G., Gehres, N., Banhold, K., Schriever, S., and Hoffmann, T. (2019). From source to mouth: Basin-scale morphodynamics of the Rhine River. *Earth-science Reviews*, 196:102830. DOI: 10.1016/j.earscirev.2019.04.002.

Fu, G. (2008). A fuzzy optimization method for multicriteria decision making: An application to reservoir flood control operation. *Expert Systems with Applications*, 34(1):145–149. DOI: 10.1016/j.eswa.2006.08.021.

Fu, L.-L. and Cazenave, A. (2000). *Satellite altimetry and earth sciences: a handbook of techniques and applications*. International Geophysics Series, Volume 69, Academic Press. ISBN: 0-12-269545-3.

Fu, L.-L. and Chelton, D. B. (1985). Observing large-scale temporal variability of ocean currents by satellite altimetry: With application to the Antarctic Circumpolar Current. *Journal of Geophysical Research: Oceans*, 90(C3):4721–4740. DOI: 10.1029/JC090iC03p04721.

Fu, L.-L. and Vazquez, J. (1988). On correcting radial orbit errors for altimetric satellites using crossover analysis. *Journal of Atmospheric and Oceanic Technology*, 5(3):466–471. DOI: 10.1175/1520-0426(1988)005<0466:OCROEF>2.0.CO;2.

Gao, B.-C. (1996). NDWI—A normalized difference water index for remote sensing of vegetation liquid water from space. *Remote Sensing of Environment*, 58(3):257–266. DOI: 10.1016/S0034-4257(96)00067-3.

Gao, J. (2009). Bathymetric mapping by means of remote sensing: methods, accuracy and limitations. *Progress in Physical Geography*, 33(1):103–116. DOI: 10.1177/0309133309105657.

Golub, G. H. and Van Loan, C. F. (2013). *Matrix computations*. The Johns Hopkins University Press. ISBN: 9781421407944.

Halicki, M. and Niedzielski, T. (2022). The accuracy of the Sentinel-3A altimetry over Polish rivers. *Journal of Hydrology*, 606:127355. DOI: 10.1016/j.jhydrol.2021.127355.

Hall, D. K. and Martinec, J. (1985). *Remote sensing of ice and snow*. Springer Dordrecht. ISBN: 978-94-009-4842-6. DOI: 10.1007/978-94-009-4842-6.

He, J.-J., Sun, L.-Y., Gong, H.-L., and Cai, Q.-G. (2018). Comparison of rill flow velocity regimes between developing and stationary rills. *Catena*, 167:13–17. DOI: 10.1016/j.catena.2018.04.020.

Hilldale, R. C. and Raff, D. (2008). Assessing the ability of airborne lidar to map river bathymetry. *Earth Surface Processes and Landforms*, 33(5):773–783. DOI: 10.1002/esp.1575.

Hohensinner, S., Hauer, C., and Muhar, S. (2018). River morphology, channelization, and habitat restoration. *Riverine Ecosystem Management: Science for Governing towards a Sustainable Future*, pages 41–65. DOI: 10.1007/978-3-319-73250-3_3.

Holdren, G. C. and Turner, K. (2010). Characteristics of Lake Mead, Arizona–Nevada. *Lake and Reservoir Management*, 26(4):230–239. DOI: 10.1080/07438141.2010.540699.

Houry, S., Minster, J., Brossier, C., Dominh, K., Gennero, M., Cazenave, A., and Vincent, P. (1994). Radial orbit error reduction and mean sea surface computation from the Geosat altimeter data. *Journal of Geophysical Research: Solid Earth*, 99(B3):4519–4531. DOI: 10.1029/93JB02004.

Immerzeel, W. W., Droogers, P., De Jong, S., and Bierkens, M. (2009). Large–scale monitoring of snow cover and runoff simulation in Himalayan river basins using remote sensing. *Remote Sensing of Environment*, 113(1):40–49. DOI: 10.1016/j.rse.2008.08.010.

IPCC (2013). Climate Change 2013: The Physical Science Basis. Contribution of Working Group I to the Fifth Assessment Report of the Intergovernmental Panel on Climate Change [Stocker, T.F., D. Qin, G.-K. Plattner, M. Tignor, S.K. Allen, J. Boschung, A. Nauels, Y. Xia, V. Bex and P.M. Midgley (eds.)]. *Cambridge University Press*, 1535. ISBN: 9781107057991.

IPCC (2021). Climate Change 2021: The Physical Science Basis. Contribution of Working Group I to the Sixth Assessment Report of the Intergovernmental Panel on Climate Change [Masson-Delmotte, V., P. Zhai, A. Pirani, S.L. Connors, C. Péan, S. Berger, N. Caud, Y. Chen, L. Goldfarb, M.I. Gomis, M. Huang, K. Leitzell, E. Lonnoy, J.B.R. Matthews, T.K. Maycock, T. Waterfield, O. Yelekçi, R. Yu, and B. Zhou (eds.)]. *Cambridge University Press*, 2391. DOI: 10.1017/9781009157896.

IPCC (2022). Climate change 2022: Impacts, adaptation and vulnerability. Contribution of Working Group II to the Sixth Assessment Report of the Intergovernmental Panel on Climate Change. [H.-O. Pörtner, D.C. Roberts, M. Tignor, E.S. Poloczanska, K. Mintenbeck, A. Alegría, M. Craig, S. Langsdorf, S. Löschke, V. Möller, A. Okem, B. Rama (eds.)]. *Cambridge University Press*, 3056. DOI: 10.1017/9781009325844.

Jackson, T. J., Schmugge, J., and Engman, E. (1996). Remote sensing applications to hydrology: soil moisture. *Hydrological Sciences Journal*, 41(4):517–530. DOI: 10.1080/02626669609491523.

Jasinski, M., Stoll, J., Hancock, D., Robbins, J., Nattala, J., Morison, J., Jones, B., Ondrusek, M., Pavelsky, T., and Parrish, C. (2021). Algorithm Theoretical Basis Document (ATBD) for Along Track Inland Surface Water Data, Release 005. *Goddard Space Flight Center Greenbelt, NASA, Maryland, USA*. DOI: 10.5067/RI5QTGTSVHRZ.

Jasinski, M. F., Stoll, J. D., Cook, W. B., Ondrusek, M., Stengel, E., and Brunt, K. (2016). Inland and near-shore water profiles derived from the high-altitude Multiple Altimeter Beam Experimental Lidar (MABEL). *Journal of Coastal Research*, 76(1):44–55. DOI: 10.2112/SI76-005.

Jeniffer, K., Su, Z., Woldai, T., and Maathuis, B. (2010). Estimation of spatial–temporal rainfall distribution using remote sensing techniques: A case study of Makanya catchment, Tanzania. *International Journal of Applied Earth Observation and Geoinformation*, 12:S90–S99. DOI: 10.1016/j.jag.2009.10.003.

Jiang, L., Bandini, F., Smith, O., Klint Jensen, I., and Bauer-Gottwein, P. (2020). The value of distributed high-resolution UAV-borne observations of water surface elevation for river management and hydrodynamic modeling. *Remote Sensing*, 12(7):1171. DOI: 10.3390/rs12071171.

Jiang, S., Ren, L., Yong, B., Fu, C., and Yang, X. (2012a). Analyzing the effects of climate variability and human activities on runoff from the Laohahe basin in northern China. *Hydrology Research*, 43(1-2):3–13. DOI: 10.2166/nh.2011.133.

Jiang, X., Lin, M., Liu, J., Zhang, Y., Xie, X., Peng, H., and Zhou, W. (2012b). The HY-2 satellite and its preliminary assessment. *International Journal of Digital Earth*, 5(3):266–281. DOI: 10.1080/17538947.2012.658685.

Jung, G., Wagner, S., and Kunstmann, H. (2012). Joint climate–hydrology modeling: an impact study for the data-sparse environment of the Volta Basin in West Africa. *Hydrology Research*, 43(3):231–248. DOI: 10.2166/nh.2012.044.

Kerr, Y. H., Waldteufel, P., Richaume, P., Wigneron, J. P., Ferrazzoli, P., Mahmoodi, A., Al Bitar, A., Cabot, F., Gruhier, C., Juglea, S. E., Leroux, D., Mialon, A., and Delwart, S. (2012). The SMOS soil moisture retrieval algorithm. *IEEE Transactions on Geoscience and Remote Sensing*, 50(5):1384–1403. DOI: 110.1109/TGRS.2012.2184548.

Kidd, C. and Huffman, G. (2011). Global precipitation measurement. *Meteorological Applications*, 18(3):334–353. DOI: 10.1002/met.284.

Knighton, D. (2014). *Fluvial forms and processes: a new perspective*. Routledge. ISBN: 978-0-340-66313-4.

LeFavour, G. and Alsdorf, D. (2005). Water slope and discharge in the Amazon River estimated using the shuttle radar topography mission digital elevation model. *Geophysical Research Letters*, 32(17). DOI: 10.1029/2005GL023836.

Lehner, B. and Döll, P. (2004). Development and validation of a global database of lakes, reservoirs and wetlands. *Journal of Hydrology*, 296(1-4):1–22. DOI: 10.1016/j.jhydrol.2004.03.028.

Leigh, H. W., Magruder, L. A., Carabajal, C. C., Saba, J. L., and McGarry, J. F. (2014). Development of onboard digital elevation and relief databases for ICESat-2. *IEEE Transactions on Geoscience and Remote Sensing*, 53(4):2011–2020. DOI: 10.1109/TGRS.2014.2352277.

Lethbridge, M. (1967). Precipitation probability and satellite radiation data. *Monthly Weather Review*, 95(7):487–490. DOI: 10.1175/1520-0493(1967)095<0487:PPASRD>2.3.CO;2.

Lettenmaier, D. P., Alsdorf, D., Dozier, J., Huffman, G. J., Pan, M., and Wood, E. F. (2015). Inroads of remote sensing into hydrologic science during the WRR era. *Water Resources Research*, 51(9):7309–7342. DOI: 10.1002/2015WR017616.

Lighthill, M. J. and Whitham, G. B. (1955). On kinematic waves I. Flood movement in long rivers. *Proceedings of the Royal Society of London. Series A. Mathematical and Physical Sciences*, 229(1178):281–316. DOI: 10.1098/rspa.1955.0088.

Liu, Y. Y., Dorigo, W. A., Parinussa, R., de Jeu, R. A., Wagner, W., McCabe, M. F., Evans, J., and Van Dijk, A. (2012). Trend-preserving blending of passive and active microwave soil moisture retrievals. *Remote Sensing of Environment*, 123:280–297. DOI: 10.1016/j.rse.2012.03.014.

Luo, Y., Guan, K., and Peng, J. (2018). STAIR: A generic and fully–automated method to fuse multiple sources of optical satellite data to generate a high–resolution, daily and cloud-/gap-free surface reflectance product. *Remote Sensing of Environment*, 214:87–99. DOI: 10.1016/j.rse.2018.04.042.

Ma, Y., Xu, N., Sun, J., Wang, X. H., Yang, F., and Li, S. (2019). Estimating water levels and volumes of lakes dated back to the 1980s using Landsat imagery and photon-counting lidar datasets. *Remote Sensing of Environment*, 232:111287. DOI: 10.1016/j.rse.2019.111287.

Mandlburger, G., Weiß, R., and Artz, T. (2020). Mapping of water surface levels and slopes with single photon lidar–a case study at the river Rhine. *International Archives of the Photogrammetry, Remote Sensing & Spatial Information Sciences*. DOI: 10.5194/isprs-archives-XLIII-B1-2020-57-2020.

Manning, R. (1891). On the flow of water in open channels and pipes. *Transactions of the Institution of Civil Engineers of Ireland*, 20:161–207.

Markus, T., Neumann, T., Martino, A., Abdalati, W., Brunt, K., Csatho, B., Farrell, S., Fricker, H., Gardner, A., Harding, D., Jasinski, M., Kwok, R., Magruder, L., Lubin, D., Luthcke, S., Morison, J., Nelson, R., Neuenschwander, A., Palm, S., Popescu, S., Shum, C., Schutz, B. E., Smith, B., Yang, Y., and Zwally, J. (2017). The Ice, Cloud, and land Elevation Satellite-2 (ICESat-2): science requirements, concept, and implementation. *Remote Sensing of Environment*, 190:260–273. DOI: 10.1016/j.rse.2016.12.029.

Marques, A. C., Veras, C. E., and Rodriguez, D. A. (2022). Assessment of water policies contributions for sustainable water resources management under climate change scenarios. *Journal of Hydrology*, 608:127690. DOI: 10.1016/j.jhydrol.2022.127690.

McCabe, M. F., Ershadi, A., Jimenez, C., Miralles, D. G., Michel, D., and Wood, E. F. (2016). The GEWEX LandFlux project: Evaluation of model evaporation using tower-based and globally gridded forcing data. *Geoscientific Model Development*, 9(1):283–305. DOI: 10.5194/gmd-9-283-2016.

McGill, M., Markus, T., Scott, V. S., and Neumann, T. (2013). The multiple altimeter beam experimental Lidar (MABEL): An airborne simulator for the ICESat-2 mission. *Journal of Atmospheric and Oceanic Technology*, 30(2):345–352. DOI: 10.1175/JTECH-D-12-00076.1.

Mertes, L. A., Dunne, T., and Martinelli, L. A. (1996). Channel-floodplain geomorphology along the solimões-Amazon river, Brazil. *Geological Society of America Bulletin*, 108(9):1089–1107. DOI: 10.1130/0016-7606(1996)108<1089:CFGATS>2.3.CO;2.

Morison, J., Hancock, D., Dickinson, S., Robbins, J., Roberts, L., Kwok, R., Palm, S., Smith, B., Jasinski, M., Plant, B., and Urban, T. (2019). Algorithm Theoretical Basis Document (ATBD) for Ocean Surface Height. *National Aeronautics and Space Administration*. Available online at icesat-2.gsfc.nasa.gov/sites/default/files/page_files/ICESat2_ATL12_ATBD_r002.pdf.

Mu, Q., Heinsch, F. A., Zhao, M., and Running, S. W. (2007). Development of a global evapotranspiration algorithm based on MODIS and global meteorology data. *Remote Sensing of Environment*, 111(4):519–536. DOI: 10.1016/j.rse.2007.04.015.

Muller-Karger, F. E., Hestir, E., Ade, C., Turpie, K., Roberts, D. A., Siegel, D., Miller, R. J., Humm, D., Izenberg, N., Keller, M., Morgan, F., Frouin, R., Dekker, A. G., Gardner, R., Goodman, J., Schaeffer, B., Franz, B. A., Pahlevan, N., Mannino, A. G., Concha, J. A., Ackleson, S. G., Cavanaugh, K. C., Romanou, A., Tzortziou, M., Boss, E. S., Pavlick, R., Freeman, A., Rousseaux, C. S., Dunne, J., Long, M. C., Klein, E., McKinley, G. A., Goes, J., Letelier, R., Kavanaugh, M., Roffer, M., Bracher, A., Arrigo, K. R., Dierssen, H., Zhang, X., Davis, F. W., Best, B., Guralnick, R., Moisan, J., Sosik, H. M., Kudela, R., Mouw, C. B., Barnard, A. H., Palacios, S., Roesler, C., Drakou, E. G., Appeltans, W., and Jetz, W. (2018). Satellite sensor requirements for monitoring essential biodiversity variables of coastal ecosystems. *Ecological Applications*, 28(3):749–760. DOI: 10.1002/eap.1682.

Neumann, G. A., Rowlands, D. D., Lemoine, F. G., Smith, D. E., and Zuber, M. T. (2001). Crossover analysis of Mars orbiter laser altimeter data. *Journal of Geophysical Research: Planets*, 106(E10):23753–23768. DOI: 10.1029/2000JE001381.

Neumann, T., Brenner, A., Hancock, D., Robbins, J., Saba, J., Harbeck, K., Gibbons, A., Lee, J., Luthcke, S., and Rebold, T. (2021). Ice, cloud, and land elevation satellite–2 (ICESat-2) project: Algorithm theoretical basis document (ATBD) for global geolocated photons (ATL03), Version 5. *National Aeronautics and Space Administration, Goddard Space Flight Center*. Available online at nsidc.org/sites/default/files/icesat2_atl03_atbd_r005_0.pdf.

Neumann, T. A., Martino, A. J., Markus, T., Bae, S., Bock, M. R., Brenner, A. C., Brunt, K. M., Cavanaugh, J., Fernandes, S. T., Hancock, D. W., Harbeck, K., Lee, J., Kurtz, N. T., Luers, P. J., Luthcke, S. B., Magruder, L., Pennington, T. A., Ramos-Izquierdo, L., Rebold, T., Skoog, J., and Thomas, T. C. (2019). The Ice, Cloud, and Land Elevation Satellite–2 Mission: A global geolocated photon product derived from the advanced topographic laser altimeter system. *Remote Sensing of Environment*, 233:111325. DOI: 10.1016/j.rse.2019.111325.

Odhiambo, B. K. and Boss, S. K. (2004). Integrated Echo Sounder, GPS, and GIS for Reservoir Sedimentation Studies: Examples from Two Arkansas Lakes 1. *JAWRA Journal of the American Water Resources Association*, 40(4):981–997. DOI: 10.1111/j.1752-1688.2004.tb01061.x.

Otsu, N. (1979). A threshold selection method from gray-level histograms. *IEEE Transactions on Systems, Man, and Cybernetics*, 9(1):62–66. DOI: 10.1109/TSMC.1979.4310076.

Paiva, R. d., Collischonn, W., Bonnet, M.-P., De Goncalves, L., Calmant, S., Getirana, A., and Santos da Silva, J. (2013). Assimilating in situ and radar altimetry data into a large-scale hydrologic-hydrodynamic model for streamflow forecast in the Amazon. *Hydrology and Earth System Sciences*, 17(7):2929–2946. DOI: 10.5194/hess-17-2929-2013.

Paloscia, S., Pettinato, S., Santi, E., Notarnicola, C., Pasolli, L., and Reppucci, A. (2013). Soil moisture mapping using Sentinel-1 images: Algorithm and preliminary validation. *Remote Sensing of Environment*, 134:234–248. DOI: 10.1016/j.rse.2013.02.027.

Paris, A., Dias de Paiva, R., Santos da Silva, J., Medeiros Moreira, D., Calmant, S., Garambois, P.-A., Collischonn, W., Bonnet, M.-P., and Seyler, F. (2016).

Stage-discharge rating curves based on satellite altimetry and modeled discharge in the Amazon basin. *Water Resources Research*, 52(5):3787–3814. DOI: 10.1002/2014WR016618.

Parsaie, A. (2016). Analyzing the distribution of momentum and energy coefficients in compound open channel. *Modeling Earth Systems and Environment*, 2:1–5. DOI: 10.1007/s40808-015-0054-x.

Paz, A. R. and Collischonn, W. (2007). River reach length and slope estimates for large-scale hydrological models based on a relatively high-resolution digital elevation model. *Journal of Hydrology*, 343(3-4):127–139. DOI: 10.1016/j.jhydrol.2007.06.006.

Pekel, J.-F., Cottam, A., Gorelick, N., and Belward, A. S. (2016). High-resolution mapping of global surface water and its long-term changes. *Nature*, 540(7633):418–422. DOI: 10.1038/nature20584.

Peng, D., Guo, S., Liu, P., and Liu, T. (2006). Reservoir storage curve estimation based on remote sensing data. *Journal of Hydrologic Engineering*, 11(2):165–172. DOI: 10.1061/(ASCE)1084-0699(2006)11:2(165).

Ranndal, H., Sigaard Christiansen, P., Kliving, P., Baltazar Andersen, O., and Nielsen, K. (2021). Evaluation of a statistical approach for extracting shallow water bathymetry signals from ICESat-2 ATL03 photon data. *Remote Sensing*, 13(17):3548. DOI: 10.3390/rs13173548.

Rapp, R. H. (1979). Geos 3 data processing for the recovery of geoid undulations and gravity anomalies. *Journal of Geophysical Research: Solid Earth*, 84(B8):3784–3792. DOI: 10.1029/JB084iB08p03784.

Rose, S. K., Andersen, O. B., Passaro, M., Ludwigsen, C. A., and Schwatke, C. (2019). Arctic ocean sea level record from the complete radar altimetry era: 1991–2018. *Remote Sensing*, 11(14):1672. DOI: 10.3390/rs11141672.

Ryan, J. C., Smith, L. C., Cooley, S. W., Pitcher, L. H., and Pavelsky, T. M. (2020). Global characterization of inland water reservoirs using icesat-2 altimetry and climate reanalysis. *Geophysical Research Letters*, 47(17):e2020GL088543. DOI: 10.1029/2020GL088543.

Scherer, D., Schwatke, C., Dettmering, D., and Seitz, F. (2022). ICESat-2 based river surface slope and its impact on water level time series from satellite altimetry. *Water Resources Research*, 58(11):e2022WR032842. DOI: 10.1029/2022WR032842.

Schlembach, F., Passaro, M., Quartly, G. D., Kurekin, A., Nencioli, F., Dodet, G., Piollé, J.-F., Ardhuin, F., Bidlot, J., Schwatke, C., Seitz, F., Cipollini, P., and Donlon, C. (2020). Round robin assessment of radar altimeter Low Resolution Mode and delay-Doppler retracking algorithms for significant wave height. *Remote Sensing*, 12(8):1254. DOI: 10.3390/rs12081254.

Schrama, E. J. (1989). *The role of errors orbit in processing of satellite altimeter data*. PhD thesis. Delft University of Technology, the Netherlands. Publications on Geodesy, 33. Available online at resolver.tudelft.nl/uuid:a959901f-1808-443a-8b03-9fdcfdb1eb5a.

Schutz, B. E., Zwally, H. J., Shuman, C. A., Hancock, D., and DiMarzio, J. P. (2005). Overview of the ICESat mission. *Geophysical Research Letters*, 32(21). DOI: 10.1029/2005GL024009.

Schwatke, C., Dettmering, D., Bosch, W., and Seitz, F. (2015). DAHITI–an innovative approach for estimating water level time series over inland waters using multi-mission satellite altimetry. *Hydrology and Earth System Sciences*, 19(10):4345–4364. DOI: 10.5194/hess-19-4345-2015.

Schwatke, C., Scherer, D., and Dettmering, D. (2019). Automated extraction of consistent time-variable water surfaces of lakes and reservoirs based on Landsat and Sentinel-2. *Remote Sensing*, 11(9):1010. DOI: 10.3390/rs11091010.

Seckler, D., Barker, R., and Amarasinghe, U. (1999). Water scarcity in the twenty-first century. *International Journal of Water Resources Development*, 15(1-2):29–42. DOI: 10.1080/07900629948916.

Shen, X., Wang, D., Mao, K., Anagnostou, E., and Hong, Y. (2019). Inundation extent mapping by synthetic aperture radar: A review. *Remote Sensing*, 11(7):879. DOI: 10.3390/rs11070879.

Shum, C., Schutz, B., Tapley, B., and Zhang, B. (1990). Altimeter crossover methods for precision orbit determination and the mapping of geophysical parameters. *Journal of the Astronautical Sciences*, 38:355–368.

Sichangi, A. W., Wang, L., Yang, K., Chen, D., Wang, Z., Li, X., Zhou, J., Liu, W., and Kuria, D. (2016). Estimating continental river basin discharges using multiple remote sensing data sets. *Remote Sensing of Environment*, 179:36–53. DOI: 10.1016/j.rse.2016.03.019.

Siriwardena, L., Finlayson, B., and McMahon, T. (2006). The impact of land use change on catchment hydrology in large catchments: The Comet River, Central Queensland, Australia. *Journal of Hydrology*, 326(1-4):199–214. DOI: 10.1016/j.jhydrol.2005.10.030.

Smith, D. E., Zuber, M. T., Frey, H. V., Garvin, J. B., Head, J. W., Muhleman, D. O., Pettengill, G. H., Phillips, R. J., Solomon, S. C., Zwally, H. J., Banerdt, W. B., Duxbury, T. C., Golombek, M. P., Lemoine, F. G., Neumann, G. A., Rowlands, D. D., Aharonson, O., Ford, P. G., Ivanov, A. B., Johnson, C. L., McGovern, P. J., Abshire, J. B., Afzal, R. S., and Sun, X. (2001). Mars Orbiter Laser Altimeter: Experiment summary after the first year of global mapping of Mars. *Journal of Geophysical Research: Planets*, 106(E10):23689–23722. DOI: 10.1029/2000JE001364.

Smith, D. E., Zuber, M. T., Neumann, G. A., Lemoine, F. G., Mazarico, E., Torrence, M. H., McGarry, J. F., Rowlands, D. D., Head III, J. W., Duxbury, T. H., Aharonson, O., Lucey, P. G., Robinson, M. S., Barnouin, O. S., Cavanaugh, J. F., Sun, X., Liiva, P., Mao, D., Smith, J. C., and Bartels, A. E. (2010). Initial observations from the lunar orbiter laser altimeter (LOLA). *Geophysical Research Letters*, 37(18). DOI: 10.1029/2010GL043751.

Sneeuw, N., Lorenz, C., Devaraju, B., Tourian, M. J., Riegger, J., Kunstmann, H., and Bárdossy, A. (2014). Estimating runoff using hydro-geodetic approaches. *Surveys in Geophysics*, 35(6):1333–1359. DOI: 10.1007/s10712-014-9300-4.

Spinhirne, J. D., Palm, S. P., Hart, W. D., Hlavka, D. L., and Welton, E. J. (2005). Cloud and aerosol measurements from GLAS: Overview and initial results. *Geophysical Research Letters*, 32(22). DOI: 10.1029/2005GL023507.

Sulistioadi, Y., Tseng, K.-H., Shum, C., Hidayat, H., Sumaryono, M., Suhardiman, A., Setiawan, F., and Sunarso, S. (2015). Satellite radar altimetry for monitoring small rivers and lakes in Indonesia. *Hydrology and Earth System Sciences*, 19(1):341–359. DOI: 10.5194/hess-19-341-2015.

Tai, C.-K. (1988). Geosat crossover analysis in the tropical Pacific: 1. Constrained sinusoidal crossover adjustment. *Journal of Geophysical Research: Oceans*, 93(C9):10621–10629. DOI: 10.1029/JC093iC09p10621.

Tang, H., Dubayah, R., Swatantran, A., Hofton, M., Sheldon, S., Clark, D. B., and Blair, B. (2012). Retrieval of vertical LAI profiles over tropical rain forests using waveform lidar at La Selva, Costa Rica. *Remote Sensing of Environment*, 124:242–250. DOI: 10.1016/j.rse.2012.05.005.

Tang, P., Huber, D., Akinci, B., Lipman, R., and Lytle, A. (2010). Automatic reconstruction of as-built building information models from laser-scanned point clouds: A review of related techniques. *Automation in Construction*, 19(7):829–843. DOI: 10.1016/j.autcon.2010.06.007.

Tedesco, M., Derksen, C., Deems, J. S., and Foster, J. L. (2015). Remote sensing of snow depth and snow water equivalent. *Remote Sensing of the Cryosphere*, pages 73–98. DOI: 10.1002/9781118368909.ch5.

Thompson, J. (2012). Modelling the impacts of climate change on upland catchments in southwest Scotland using MIKE SHE and the UKCP09 probabilistic projections. *Hydrology Research*, 43(4):507–530. DOI: 10.2166/nh.2012.105.

Tourian, M. (2013). *Application of spaceborne geodetic sensors for hydrology*. PhD thesis, University of Stuttgart, Stuttgart, Germany. DOI: 10.18419/opus-3929.

Tourian, M., Schwatke, C., and Sneeuw, N. (2017). River discharge estimation at daily resolution from satellite altimetry over an entire river basin. *Journal of Hydrology*, 546:230–247. DOI: 10.1016/j.jhydrol.2017.01.009.

Tourian, M., Sneeuw, N., and Bárdossy, A. (2013). A quantile function approach to discharge estimation from satellite altimetry (ENVISAT). *Water Resources Research*, 49(7):4174–4186. DOI: 10.1002/wrcr.20348.

Tourian, M., Tarpanelli, A., Elmi, O., Qin, T., Brocca, L., Moramarco, T., and Sneeuw, N. (2016). Spatiotemporal densification of river water level time series by multimission satellite altimetry. *Water Resources Research*, 52(2):1140–1159. DOI: 10.1002/2015WR017654.

Uhlenbrook, S. and Connor, R. (2019). The United Nations world water development report 2019: leaving no one behind. Available online at http://hdl.handle.net/1834/42357.

Van Gysen, H. and Coleman, R. (1997). On the satellite altimeter crossover problem. *Journal of Geodesy*, 71(2):83–96. DOI: 10.1007/s001900050077.

Wagner, W., Dorigo, W., De Jeu, R., Fernandez, D., Benveniste, J., Haas, E., and Ertl, M. (2012). Fusion of active and passive microwave observations to create an essential climate variable data record on soil moisture. *ISPRS Annals of the Photogrammetry, Remote Sensing and Spatial Information Sciences (ISPRS Annals)*, 7:315–321. DOI: 10.5194/isprsannals-I-7-315-2012.

Wang, B. and Sneeuw, N. (2024). Crossover adjustment of ICESat-2 satellite altimetry for the Arctic region. *Advances in Space Research*, 73(1):376–385. DOI: 10.1016/j.asr.2023.07.041.

Weatherall, P., Marks, K. M., Jakobsson, M., Schmitt, T., Tani, S., Arndt, J. E., Rovere, M., Chayes, D., Ferrini, V., and Wigley, R. (2015). A new digital bathymetric model of the world's oceans. *Earth and Space Science*, 2(8):331–345. DOI: 10.1002/2015EA000107.

Webb, C. E., Jay, Z. H., and Abdalati, W. (2012). The ice, cloud, and land elevation satellite (ICESat) summary mission timeline and performance relative to pre-launch mission success criteria. Available online at https://ntrs.nasa.gov/citations/20130014062.

Wingham, D., Francis, C., Baker, S., Bouzinac, C., Brockley, D., Cullen, R., de Chateau-Thierry, P., Laxon, S., Mallow, U., Mavrocordatos, C., Phalippou, L., Ratier, G., Rey, L., Rostan, F., Viau, P., and Wallis, D. (2006). CryoSat: A mission to determine the fluctuations in Earth's land and marine ice fields. *Advances in Space Research*, 37(4):841–871. DOI: 10.1016/j.asr.2005.07.027.

Wunsch, C. and Zlotnicki, V. (1984). The accuracy of altimetric surfaces. *Geophysical Journal International*, 78(3):795–808. DOI: 10.1111/j.1365-246X.1984.tb05071.x.

Xing, Y., de Gier, A., Zhang, J., and Wang, L. (2010). An improved method for estimating forest canopy height using ICESat-GLAS full waveform data over sloping terrain: A case study in Changbai mountains, China. *International Journal of Applied Earth Observation and Geoinformation*, 12(5):385–392. DOI: 10.1016/j.jag.2010.04.010.

Xu, H. (2006). Modification of normalised difference water index (NDWI) to enhance open water features in remotely sensed imagery. *International Journal of Remote Sensing*, 27(14):3025–3033. DOI: 10.1080/01431160600589179.

Yamanouchi, T. and Takata, K. (2020). Rapid change of the Arctic climate system and its global influences-Overview of GRENE Arctic climate change research project (2011–2016). *Polar Science*, 25:100548. DOI: 10.1016/j.polar.2020.100548.

Yamazaki, D., Ikeshima, D., Sosa, J., Bates, P. D., Allen, G. H., and Pavelsky, T. M. (2019). MERIT Hydro: a high-resolution global hydrography map based on latest topography dataset. *Water Resources Research*, 55(6):5053–5073. DOI: 10.1029/2019WR024873.

Yamazaki, D., Ikeshima, D., Tawatari, R., Yamaguchi, T., O'Loughlin, F., Neal, J. C., Sampson, C. C., Kanae, S., and Bates, P. D. (2017). A high-accuracy map of

global terrain elevations. *Geophysical Research Letters*, 44(11):5844–5853. DOI: 10.1002/2017GL072874.

Yang, X., Qin, Q., Grussenmeyer, P., and Koehl, M. (2018). Urban surface water body detection with suppressed built-up noise based on water indices from Sentinel-2 MSI imagery. *Remote Sensing of Environment*, 219:259–270. DOI: 10.1016/j.rse.2018.09.016.

Yaseen, Z. M., Sulaiman, S. O., Deo, R. C., and Chau, K.-W. (2019). An enhanced extreme learning machine model for river flow forecasting: State-of-the-art, practical applications in water resource engineering area and future research direction. *Journal of Hydrology*, 569:387–408. DOI: 10.1016/j.jhydrol.2018.11.069.

Yeh, P. J.-F., Swenson, S. C., Famiglietti, J. S., and Rodell, M. (2006). Remote sensing of groundwater storage changes in Illinois using the Gravity Recovery and Climate Experiment (GRACE). *Water Resources Research*, 42(12). DOI: 10.1029/2006WR005374.

Zakharova, E., Nielsen, K., Kamenev, G., and Kouraev, A. (2020). River discharge estimation from radar altimetry: Assessment of satellite performance, river scales and methods. *Journal of Hydrology*, 583:124561. DOI: 10.1016/j.jhydrol.2020.124561.

Zhang, G., Yao, T., Shum, C., Yi, S., Yang, K., Xie, H., Feng, W., Bolch, T., Wang, L., Behrangi, A., Zhang, H., Wang, W., Xiang, Y., and Yu, J. (2017). Lake volume and groundwater storage variations in Tibetan Plateau's endorheic basin. *Geophysical Research Letters*, 44(11):5550–5560. DOI: 10.1002/2017GL073773.

Zhang, J., Hu, Q., Li, Y., Li, H., and Li, J. (2021). Area, lake-level and volume variations of typical lakes on the Tibetan Plateau and their response to climate change, 1972–2019. *Geo-Spatial Information Science*, 24(3):458–473. DOI: 10.1080/10095020.2021.1940318.

Zhang, J. and Kerekes, J. (2014). An adaptive density-based model for extracting surface returns from photon-counting laser altimeter data. *IEEE Geoscience and Remote Sensing Letters*, 12(4):726–730. DOI: 10.1109/LGRS.2014.2360367.

Zhang, Z., Chen, G., Bo, Y., Guo, X., and Bao, J. (2022). Performance evaluation of combining ICESat-2 and GEDI laser altimetry missions for inland lake level retrievals. *Geoscience Letters*, 9(1):1–13. DOI: 10.1186/s40562-022-00243-w.

Zlinszky, A., Timár, G., Weber, R., Székely, B., Briese, C., Ressl, C., and Pfeifer, N. (2014). Observation of a local gravity potential isosurface by airborne lidar of Lake Balaton, Hungary. *Solid Earth*, 5(1):355–369. DOI: 10.5194/se-5-355-2014.

Zwally, H. J., Schutz, B., Abdalati, W., Abshire, J., Bentley, C., Brenner, A., Bufton, J., Dezio, J., Hancock, D., Harding, D., Herring, T., Minster, B., Quinn, K., Palm, S., Spinhirne, J., and Thomas, R. (2002). ICESat's laser measurements of polar ice, atmosphere, ocean, and land. *Journal of Geodynamics*, 34(3-4):405–445. DOI: 10.1016/S0264-3707(02)00042-X.

Appendix A

Baarda's data snooping

The probabilistic characteristics of measurement errors are closely linked to the assumed probability distribution of these errors. In geodesy and various other scientific fields, the widely recognized normal distribution serves as a frequently employed model for measurement errors. This choice is substantiated by both the central limit theorem and the maximum entropy principle, further justifying the use of the normal distribution as a suitable representation for measurement errors. Consequently, the null hypothesis (H_0) is formulated based on the assumption that the random errors follow a normal distribution with a mean of zero. When the null hypothesis H_0 is assumed to be true, the associated model is used to estimate unknown parameters, typically using a least-squares methodology. Therefore, in the linear or linearized form of the standard Gauss-Markov model, the null hypothesis H_0 can be expressed as follows:

$$\begin{aligned} H_0 : \mathrm{E}\left\{\underline{y}\right\} = Ax + \mathrm{E}\left\{e\right\};\ \mathrm{D}\left\{\underline{y}\right\} = Q_y, \\ \rightarrow \underline{\hat{y}}_0 = A\underline{\hat{x}}_0, \\ \rightarrow \underline{\hat{e}}_0 = \underline{y} - \underline{\hat{y}}_0, \end{aligned} \tag{A.1}$$

where $\mathrm{E}\{\}$ represents the expectation operator and $\mathrm{D}\{\}$ represents the dispersion operator. In this equation, $\underline{y}$ denotes the vector of measurements, A is the design matrix of full rank n, x represents the unknown parameter vector, e is the vector of unknown measurement errors, and Q_y is the covariance matrix associated with the measurements $\underline{y}$. This null hypothesis assumes that the expected value of the measurements can be accurately represented by the linear relationship between the design matrix A and the unknown parameter vector x.

In contrast, an alternative model is put forth when there are concerns regarding the reliability of the model under the null hypothesis H_0. In this case, it is assumed that the validity of the null hypothesis H_0 in Eq. A.1 can be compromised if the dataset contains outliers. The alternative hypothesis, denoted by H_a, opposes Eq. A.1 by introducing an extended model that incorporates an additional unknown vector ∇ of deterministic

bias parameters, formulated as follows:

$$\begin{aligned} H_a : \mathrm{E}\left\{\underline{y}\right\} &= Ax + C\nabla + \mathrm{E}\left\{e\right\}; \qquad \mathrm{D}\left\{\underline{y}\right\} = Q_y, \\ &= \begin{pmatrix} A & C \end{pmatrix} \begin{pmatrix} x \\ \nabla \end{pmatrix} + \mathrm{E}\left\{e\right\}, \\ &\rightarrow \underline{\hat{y}}_a = A\underline{\hat{x}}_a + C\underline{\hat{\nabla}}, \\ &\rightarrow \underline{\hat{e}}_a = \underline{y} - \underline{\hat{y}}_a, \end{aligned} \tag{A.2}$$

where C is an $m \times 1$-vector and ∇ is one-parameter scalar in Baarda's data snooping, i.e.,

$$C = \left[0, 0, ..., \underbrace{1}_{\text{position } i}, 0, ..., 0 \right]^{\mathrm{T}}. \tag{A.3}$$

Then the test statistic $\underline{T}$ is

$$\begin{aligned} \underline{T} &= \underline{\hat{e}}_0{}^{\mathrm{T}} {Q_y}^{-1} \underline{\hat{e}}_0 - \underline{\hat{e}}_a{}^{\mathrm{T}} {Q_y}^{-1} \underline{\hat{e}}_a \\ &= (\underline{\hat{y}}_0 - \underline{\hat{y}}_a)^{\mathrm{T}} {Q_y}^{-1} (\underline{\hat{y}}_0 - \underline{\hat{y}}_a) \\ &= \underline{\hat{\nabla}}^{\mathrm{T}} C^{\mathrm{T}} {Q_y}^{-1} Q_{\underline{\hat{e}}_0} {Q_y}^{-1} C \underline{\hat{\nabla}}. \end{aligned} \tag{A.4}$$

Since the normal equations under H_0 and H_a from Eq. A.1 and Eq. A.2 can be written as:

$$\begin{aligned} H_0 \quad &: \quad A^{\mathrm{T}} {Q_y}^{-1} A \underline{\hat{x}}_0 = A^{\mathrm{T}} {Q_y}^{-1} \underline{y} \\ H_a \quad &: \quad \begin{pmatrix} A^{\mathrm{T}} \\ C^{\mathrm{T}} \end{pmatrix} {Q_y}^{-1} \begin{pmatrix} A & C \end{pmatrix} \begin{pmatrix} \underline{\hat{x}} \\ \underline{\hat{\nabla}} \end{pmatrix} = \begin{pmatrix} A^{\mathrm{T}} \\ C^{\mathrm{T}} \end{pmatrix} {Q_y}^{-1} \underline{y} \\ &\iff \begin{pmatrix} A^{\mathrm{T}} {Q_y}^{-1} A & A^{\mathrm{T}} {Q_y}^{-1} C \\ C^{\mathrm{T}} {Q_y}^{-1} A & C^{\mathrm{T}} {Q_y}^{-1} C \end{pmatrix} \begin{pmatrix} \underline{\hat{x}}_a \\ \underline{\hat{\nabla}} \end{pmatrix} = \begin{pmatrix} A^{\mathrm{T}} {Q_y}^{-1} \underline{y} \\ C^{\mathrm{T}} {Q_y}^{-1} \underline{y} \end{pmatrix}, \end{aligned} \tag{A.5}$$

$\underline{\hat{x}}_a$ can be solved by the first row, which is written as:

$$\begin{aligned} & A^{\mathrm{T}} {Q_y}^{-1} A \underline{\hat{x}}_a + A^{\mathrm{T}} {Q_y}^{-1} C \underline{\hat{\nabla}} = A^{\mathrm{T}} {Q_y}^{-1} A \underline{\hat{x}}_0 \\ & \Longrightarrow \underline{\hat{x}}_a = \underline{\hat{x}}_0 - (A^{\mathrm{T}} {Q_y}^{-1} A)^{-1} A^{\mathrm{T}} {Q_y}^{-1} C \underline{\hat{\nabla}}. \end{aligned} \tag{A.6}$$

If we substitute $\underline{\hat{x}}_a$ to solve $\underline{\hat{\nabla}}$ in the second row, then we can get

$$\underline{\hat{\nabla}} = (C^{\mathrm{T}} {Q_y}^{-1} Q_{\hat{e}_0} {Q_y}^{-1} C)^{-1} C^{\mathrm{T}} {Q_y}^{-1} \underline{\hat{e}}_0. \tag{A.7}$$

Substitute $\underline{\hat{\nabla}}$ in Eq. A.4, then we get

$$\begin{aligned}
\underline{T} &= \underline{\hat{e}_0}^{\mathrm{T}} {Q_y}^{-1} C (C^{\mathrm{T}} {Q_y}^{-1} Q_{\hat{e}_0} {Q_y}^{-1} C)^{-1} C^{\mathrm{T}} {Q_y}^{-1} \underline{\hat{e}_0} \\
&= \frac{(\underline{\hat{e}_0}^{\mathrm{T}} {Q_y}^{-1} C)^2}{C^{\mathrm{T}} {Q_y}^{-1} Q_{\hat{e}_0} {Q_y}^{-1} C} \\
&= \frac{\underline{\hat{\nabla}}^2}{(C^{\mathrm{T}} {Q_y}^{-1} Q_{\hat{e}_0} {Q_y}^{-1} C)^{-1}} \\
&= \frac{\underline{\hat{\nabla}}^2}{\sigma^2_{\underline{\hat{\nabla}}}}. \\
\underline{\hat{\nabla}}^2 &= \frac{C^{\mathrm{T}} {Q_y}^{-1} \underline{\hat{e}}}{C^{\mathrm{T}} {Q_y}^{-1} Q_{\hat{e}_0} {Q_y}^{-1} C}.
\end{aligned} \tag{A.8}$$

A test decision is performed as the rule: reject H_0 if $\underline{T} = \frac{\underline{\hat{\nabla}}^2}{\sigma^2_{\underline{\hat{\nabla}}}} > k_\alpha$. The decision rule states that if Baarda's test statistic exceeds a certain critical value k_α, which corresponds to a percentage of its probability distribution, then the null hypothesis is rejected in favor of the alternative hypothesis. This decision rule represents a specific case where the null hypothesis H_0 is being tested against a single alternative hypothesis H_a. Consequently, the rejection of the null hypothesis automatically leads to the acceptance of the alternative hypothesis, and vice versa. In essence, the process of outlier detection inherently includes outlier identification, and vice versa. This is because the formulation of the alternative hypothesis H_a is based on the assumption that an outlier exists at a predetermined location within the dataset. When an observation is rejected, the dataset y_i will be iteratively tested until no more observations are rejected.